Near-net-shape Fabrication of Ni(x)Al(y) – TiC Cermets by Binder Jet Additive Manufacturing and Pressure-less Melt Infiltration

A Thesis Presented for the
Master of Science
Degree
The University of Tennessee, Knoxville

Joshua Michael Arnold

August 2018

Acknowledgements

First and foremost, I would like to extend my thankfulness and gratitude to Dr. Suresh Babu and Dr. Amy Elliott. Dr. Babu, for his constant patience and guidance pushing me to think and grow as a scientist. Dr. Elliott, for her valuable mentorship and kindness and financial support of this work. I would like to also acknowledge the rest of my committee members Dr. Claudia Rawn, Dr. Haixuan Xu, and Dr. Brett Compton. Dr. Rawn and Dr. Xu for being valuable teachers during my time at UTK and Dr. Compton for being an encouraging force in attending graduate school. Within the same vein I would also like to thank Dr. Peeyush Nandwana and Dr. Corson Cramer for their mentorship and friendship. Much of my growth and learning is a result of discussing questions and ideas with you two, which I am sure found your patience thinning on more than a few occasions.

For technical assistance and general mentorship I would like to thank Rick Lowden, Jim Kiggans, Derek Siddel, Desarae Goldsby, Chih-Hsiang Kuo, Dr. Hsin Wang, Dr. Tom Watkins, Dr. Ercan Cakmak, Dr. Niyanth Sridharan, and Dr. Boopathy Kombaiah. I would like to thank specifically Dr. John Salasin on his help with my many infiltration experiments – you spent much of your time with me when you did not have to so thank you and congratulations on graduation!

To everyone who has been apart of Suresh's research group over the last two and a half years I cannot overstate how important your friendship and support has been to me. Chih-Hsiang (Sean), Travis, Danny, Curtis, Jake, Michael, Sarah, Avinash, Naren, Sean Y., Sarah, Mohan, Haines, Hassan, and everyone else…thank you!

Finally, I would like to acknowledge the support of the Center for Materials Processing, A Tennessee Higher Education Commission (THEC) supported Accomplished Center of Excellence, for the use of various processing equipment to conduct parts of this research.

Abstract

Binder jet additive manufacturing effectively replaces preform preparation by traditional powder metallurgy methods and allows more complex geometries to be potentially fabricated. The use of a pressure-less melt infiltration technique provides a method of achieving a fully dense composite in a near-net-shape fashion, cost effective and scalable. TiC preforms (15 x 15 x 10/7.5 mm) were fabricated via Binder Jet Additive Manufacturing and then infiltrated by $NiAl_3$ and Ni_3Al using a pressure-less melt infiltration technique. Two compositions, Ni_3Al and $NiAl_3$, were used as infiltrant materials in order to compare wetting behavior and infiltration kinetics.

A stark difference in shape retention between Ni_3Al and $NiAl_3$ infiltrated preforms was observed after infiltration. It was found that the TiC particles in the as printed preform were arranged in an interconnected network structure as a result of the binder jet process and/or sintering step and is responsible for maintaining structural integrity of the printed preform. TiC dissolution by liquid Ni_3Al was significant enough to disband this network structure and force particle re-arrangement and lead to poor shape retention. Conversely, TiC particle re-arrangement did not occur during infiltration of the Al-rich $NiAl_3$ alloy and thus the network structure remained intact leading to excellent shape retention of the infiltrated preform.

It was found $NiAl_3$ exhibits a complex melting and solidification behavior where an Al-rich phase segregates heavily from the melted material. The presence of an Al-rich inter-particle matrix phase indicates the possibility of a “metered” infiltration process where multiple liquid phases of variant compositions infiltrate the “macro” and “micro” capillaries of the TiC preform in a staggered fashion. The composition and time of infiltration remains unknown and a topic of future work. Additionally, Thermodynamic simulation predicts a reaction at the TiC interface by liquid $NiAl_3$ to form Al_4C_3, with an interfacial reaction product potentially explaining the lack of TiC dissolution and volumetric shrinkage during and after infiltration by $NiAl_3$.

Table of Contents

1 Introduction 1

2 Literature Review & Background 4

2.1 Metal Matrix Composites – Cermets 4
2.2 Nickel Aluminide Based Cermets 5
2.2.1 Ni-Al Binary System 5
2.2.2 Ni_3Al and $NiAl_3$ Phases 7
2.2.3 Ni_3Al-TiC Cermet Fabrication in Literature 8
2.3 Binder Jetting 13
2.3.1 Powder Characteristics 14
2.3.2 Binder Saturation 15
2.3.3 Preform Consolidation 16
2.4 Densification by Sintering 16
2.5 Densification by Melt Infiltration 17
2.5.1 Pressure-less Infiltration 18
2.5.2 Pressure (forced) Infiltration 20
2.6 Fundamentals of Wetting 21
2.6.1 Wetting of Ceramic Solids by Liquid Metals 22
2.7 Objectives of Current Research 23

3 Experimental Procedure & Materials 25

3.1 Materials 25
3.2 Binder Jet Process 25
3.2.1 Printing Process 26
3.2.2 De-binding 27
3.2.3 Sintering Procedure 28
3.2.4 Preform geometry 28
3.3 Infiltration Experiments 29
3.3.1 Infiltration Procedure 29
3.3.2 Round 1 Infiltration Experiments 30
3.3.3 Round 2 Infiltration Experiments 31
3.4 Characterization Techniques 31
3.4.1 Archimedes Immersion Density Measurements 31
3.4.2 Microscopy 32
3.4.3 Electron Backscatter Diffraction (EBSD) 33
3.4.4 Transmission Electron Microscopy (TEM) 33
3.4.5 X-ray Diffraction (XRD) 33
3.5 X-ray Computed Tomography (XCT) 34
3.6 High Temperature Differential Scanning Calorimetry (DSC) 34

4 Results & Discussion 36

4.1 XCT of Printed TiC Preform 36
4.2 Ni_3Al – TiC infiltration 38
4.2.1 30 min Infiltration 38

4.2.2 15 min Infiltration 40
4.2.3 Ni_3Al Infiltrated Microstructure & Phase Analysis 42
4.2.4 Infiltration Kinetics – Time of Infiltration 46
4.3 $NiAl_3$ – TiC infiltration 49
4.4 Ni_3Al Infiltrated Microstructural & Phase Analysis 52
4.4.1 SEM 52
4.4.2 Initial XRD Phase Analysis 53
4.5 $NiAl_3$ Melting/Solidification Behavior 53
4.5.1 $NiAl_3$ Infiltration of TiC preform – No Excess Infiltrant 55
4.5.2 Melting & Solidification of base $NiAl_3$ Alloy 57
4.5.3 $NiAl_3$ Infiltration at Intermediate temperature 65
4.6 $NiAl_3$ Microstructure Analysis & Solidification Behavior 66
4.6.1 Al-rich phase within TiC inter-particle area 66
4.6.2 $NiAl_3$ Infiltrated Matrix Microstructure 69
4.6.3 Local TiC Interface Simulation by CALPHAD 72
4.6.4 High Temperature DSC Dissolution at Local Interface Simulation 72
4.7 Characterization of TiC Interface by TEM 74
4.8 Infiltration of TiC by $NiAl_3$ + Al Mixture 76

5 Summary, Conclusions, & Future Work 81
5.1 Conclusions 81
5.2 Suggestions for Future Work 81

References 83

Appendices 90
Appendix A: Infiltration of TiC Preform Prepared with Bi-modal Powder Distribution by $NiAl_3$ 91
Appendix B: EBSD Data for Sample 6 93

Vita 95

List of Tables

Table 1 Reported mechanical property data for Ni3Al-TiC cermets fabricated in literature. Originally compiled in this work **9**
Table 2 Chemical composition of $NiAl_3$ and Ni_3Al alloys **26**
Table 3 Process parameters for Round 1 Infiltration Experiments. Sample 2 experienced discoloration during sintering. No melting of metal infiltrant occurred during infiltration of samples 3 and 4. No infiltration occurred for Sample 11; preform used for XCT characterization. **31**
Table 4 Process parameters for Round 2 Infiltration Experiments. No infiltration of Samples S2 and S6 occurred despite melting of $NiAl_3$. Sample 11 used for infiltration after XCT characterization. Samples that have yet to be infiltrated, particularly Samples B2-B6, will be used for future experiments. **32**

List of Figures

Figure 2-1 Ni-Al binary phase diagram [18] **6**
Figure 2-2 Cermet Process Flow for Binder Jet Additive Manufacturing & Melt Infiltration Processing..... **13**
Figure 2-3 Schematic of Binder Jet Process. Courtesy of Nandwana et. al [46]..... **14**
Figure 2-4 Liquid droplet on a solid substrate depicting the solid surface energy γ_{sv} , liquid surface energy γ_{lv} , solid-liquid interface energy γ_{sl} , and contact angle θ_c **21**
Figure 3-1 X1 Lab Binder Jet Printer from ExOne used for all TiC prints **26**
Figure 3-2 De-bind cycle for all TiC prints **27**
Figure 3-3 Naytech bench top muffle furnace used for de-bind cycle of printed preform **27**
Figure 3-4 a) TiC preform ~30% dense RD 1. **b)** TiC preform ~50% dense RD 2. ..... **28**
Figure 3-5 Printed TiC preform set on bed of Ni_3Al powder inside quartz crucible **29**
Figure 3-6 CM Furnaces 1730-12 HF alumina tube furnace at UTK courtesy of Center for Materials Processing **30**
Figure 3-7 CM Furnaces 265C alumina tube furnace at ORNL **30**
Figure 4-1 XCT of Preform 9 (~30% dense), sintered at 1400°C for 2 hours. Resolution is ~10um. Average particle size of TiC powder is ~2.5um. **37**
Figure 4-2 XCT of Preform S3 (~50% dense). Resolution is ~10um. Average particle size of TiC powder is ~30um. Bright spots are contamination of a singular or multiple higher Z elements..... **37**
Figure 4-3 Sample 10 infiltrated with Ni_3Al at 1430°C for 30 mins. Visibly poor shape retention by wall collapse and excess metal fused to bottom of preform. “Upward flowing traces” of solidified metal clear along outside of preform indicating strong capillary driving force. **39**
Figure 4-4 Optical stitching of Sample 10. Significant porosity visible in excess metal fused to bottom/side of preform..... **40**
Figure 4-5 Sample 7 infiltrated with Ni_3Al at 1430C for 15 mins (left). Preform set on bed of Ni_3Al powder. Cross-section shows un-infiltrated center area of preform (right). Excess metal fused to outside of preform retains shape of circular crucible **41**
Figure 4-6 SEM image of Sample 10 infiltrated by Ni_3Al at 1430°C for 30 mins. 500x. . **42**
Figure 4-7 Optical micrograph of Sample 10 infiltrated by Ni_3Al at 1430°C for 30 mins. 5x. TiC clusters visible at lower magnifications noted by red arrows. **43**
Figure 4-8 Optical micrograph of Sample 10, infiltrated by Ni_3Al at 1430°C for 30 mins. Porosity visible within TiC clusters near center of preform. 10x. **43**
Figure 4-9 Sample 10 SEM image showing TiC particles dispersed in matrix with sporadic dark spots highlighted by yellow circles. **44**
Figure 4-10 Sample 10 SEM image showing EDS map of dark spot indicating Al-rich compared to rest of matrix **45**

Figure 4-11 Sample 10, infiltrated at 1450C for 30 mins. a) Dark phase in base Ni_3Al metal fused to outside of infiltrated preform b) EDS point analysis of infiltrated preform shows composition of dark phase to be Al-rich compared to surrounding Ni_3Al matrix (light grey); black features are TiC particles. **45**
Figure 4-12 XRD pattern for Sample 10, infiltrated at 1430°C for 30 mins confirming presence of TiC and Ni_3Al phases and possibly NiAl. Pattern is miss labeled as Sample 8 but is in fact Sample 10. Mo radiation source was used to prevent fluorescence by nickel. **47**
Figure 4-13 DSC Cooling curves of three separate Ni_3Al cycles. Two exothermic solidification peaks are observed. The first solidification peak is enlarged and moves towards lower temperatures with each progressive cycle. **47**
Figure 4-15 Time of infiltration as a function of pore radius using Lucas-Washburn equation. Assumed values include contact angle of 30°, melt viscosity (η) of 4 MPa-s, surface tension (γ_{LV}) of 1.6 J/m^2. ..... **48**
Figure 4-16 Effect of time on infiltration depth for porous TiC preforms CIPed at 285 MPa (~63% of theoretical density)" [34] **49**
Figure 4-17 Sample 6 infiltrated with $NiAl_3$ at 1415°C for 30mins. Preform shows excellent shape retention. **51**
Figure 4-18 Optical stitching of Sample 6. Significant porosity visible throughout specimen. Visible cracking indicates brittle nature of alloy. Cross-section taken from center of preform where small warpage at corners is not discernable. **51**
Figure 4-19 SEM (BSE) image of Sample 6 infiltrated by $NiAl_3$ at 1415°C for 30 mins. 500x. Light grey matrix phase is a higher atomic # phase, which is Ni_2Al_3, and will appear brighter. Cracking visible. **53**
Figure 4-20 XRD pattern for Sample 6, infiltrated with $NiAl_3$ at 1415°C for 30 mins. Presence of TiC, $NiAl_3$, Ni_2Al_3 confirmed. Pattern also checked against NiAl but no peak match **54**
Figure 4-21 Remnant material left in crucible after $NiAl_3$ infiltration into TiC preform. Precipitate of some metal phase on crucible wall. **55**
Figure 4-22 Sample 9 infiltrated with NiAl3 at 1415°C for 30 mins. The infiltrated preform is shown on the left. The top surface of the remnant material is shown in the middle while the bottom surface of the remnant material is shown on the right. **56**
Figure 4-23 Sample 9 infiltrated with $NiAl_3$ at 1415°C for 30 mins. Considerable porosity visible throughout infiltrated preform. **56**
Figure 4-24 Diffraction pattern for flat, bottom surface of Sample 9 remnant, shown left in Fig. 4-19. $NiAl_3$ and Ni_2Al_3 phases identified. Dotted lines at ~17.5° and ~25° 2Θ indicate an unidentified phase. ..... Error! Bookmark not defined.
Figure 4-25 Same diffraction pattern of flat, bottom surface ofSample 9 remnant, shown left in Fig. 18. Al-rich phase matches one of the unidentified peaks at ~25°C 2Θ, but the presence of Al-rich phase and TiC are both highly speculative. Unidentified peaks shown here are $NiAl_3$ and Ni_2Al_3 peaks shown in Fig 4-21 ..... **58**

Figure 4-26 Remnant material left in crucible after melting pure NiAl3 powder (left). Cross-section of segregated remnant material (right)..... **58**
Figure 4-27 Microstructure of metallic, silver liquid phase showing three distinct phases: Ni_2Al_3 (light grey), $NiAl_3$ (grey), and Al (dark grey). Left and right images taken at 100x and 450x respectively **59**
Figure 4-28 EDS Quantitative Point Scan Image a) Ni_2Al_3 b) $NiAl_3$ c) FCC Al. Image taken at 450x**.** ..... Error! Bookmark not defined.
Figure 4-29 XRD scan of gray, porous phase of segregated remnant material. NiAl3, Ni2Al3, and possible Al-rich phase detected. It's thought that a small part of the diffraction signal originated from the silver, metallic phase. **62**
Figure 4-30 XRD scan of silver, metallic phase of segregated remnant material. NiAl3, Ni2Al3, and Al-rich alloy confirmed **62**
Figure 4-31 Ni-Al phase diagram created using ThermoCalc showing bulk composition of $NiAl_3$ **63**
Figure 4-32 DSC Melting curves of $NiAl_3$. Black curve is first run from powder, blue and red curves are subsequent re-melting. Primary melting peak observed at ~850°C with smaller melting peaks observed at ~620°C and ~1130°C. Pattern made in Netzch analysis software. **64**
Figure 4-33 DSC Cooling curves of three separate $NiAl_3$ cycles. Primary solidification peak observed at ~820°C with smaller solidification peaks observed at ~1110°C and ~630°C. **64**
Figure 4-34 Sample S2 (left) shows complete lack of infiltration. Material remnant (right) left in crucible shows clear melting behavior and segregation of Al-rich phase. **66**
Figure 4-35 SEM image of Sample 5, infiltrated at 1415°C for 30 mins by $NiAl_3$. Cluster of TiC particles shown where high contrast reveals the porosity against dark inter-particle matrix phase. **67**
Figure 4-36 EDS map of TiC cluster in Sample 5. Inter-particle area has Al-rich matrix phase with no detected Ni alongside porosity. 1,500x magnification. **67**
Figure 4-37 EDS map of Sample 5 shows black phase adjoined and near to TiC particles that appear to be Al-rich with little to no Ni and Ti. 2,000x magnification **68**
Figure 4-38 EDS Point Scan of Sample 6 confirms dark matrix phase to be NiAl3 and light matrix phase to be Ni2Al3. TiC particles reside only within NiAl3 matrix. ... **70**
Figure 4-39 Solidification Theory 1..... **70**
Figure 4-40 Solidification Theory 2..... **71**
Figure 4-41 Scheil simulation depicting solidification behavior of 1:1 molar ratio of TiC and $NiAl_3$. Simulation conducted in ThermoCalc software with TCAL3 database. Dotted line represents the equilibrium calculation. **73**
Figure 4-42 DSC Analysis of 1:1 molar ratio TiC:NiAl3. The sample was ramped up to 1400**°**C and held for 30 mins to simulate TiC dissolution during infiltration processing. **74**

Figure 4-43 Bright field TEM image of TiC interface. Ledges are seen along the TiC/matrix interface. **75**
Figure 4-44 EDS Map of TiC interface for Bright Field TEM Image shown in Fig. 4-40. **76**
Figure 4-45 Optical cross-section of TiC preform infiltrated with NiAl3 + Al at 1415°C for 30 mins. Significant crystal growth is visible inside cavity of preform and also fused to bottom of preform. **78**
Figure 4-46 Top of infiltrated preform showing region of crystal growth in cup cavity. Crystal growth regions show light colored dendrites (NiAl3) within a dark (Al) matrix **78**
Figure 4-47 EDS Mapping of sample at bottom of crystal growth showing TiC particles dispersed in a matrix of NiAl3 + Al **79**
Figure A-1 Sample B1 infiltrated with $NiAl_3$ at 1415°C for 30 mins. Significant amount of excess material left in crucible. Silver, metallic chunk fused to bottom of infiltrated preform. **92**
Figure A-2 Optical stitching cross-section of sample B1, infiltrated with $NiAl_3$ at 1415°C for 30 mins. Large cracking seen at base of right wall and mid-height of left wall occurred as a result of the hot mount process **92**
Figure B-1 Image Quality (IQ) Map of Sample 6, Infiltrated at 1415°C for 30 mins. Light grey region is Ni_2Al_3. Dark grey is $NiAl_3$. **94**
Figure B-2 Auto Phase Map of Sample 6. ..... **94**
Figure B-3 IQ + CI map of Sample 6. ..... **94**

1 Introduction

Additive Manufacturing (AM), commonly known as “3D Printing”, is the process by which objects are fabricated layer-by-layer from a computer-aided design file. This is in contrast to traditional manufacturing processes, which are typically based on subtraction through cutting, grinding, machining, and are assembled by welding or fasteners. There exists a wide-range of AM techniques, which fall under the umbrella of AM process categories. ASTM lists seven distinct categories: [1]

1) **Direct Energy Deposition (DMD)** – thermal energy (electron beam or laser) is used to fuse materials by melting as they are being deposited
2) **Powder Bed Fusion (PBF)** – thermal energy (electron beam or laser) selectively fuses regions of a powder bed
3) **Material Extrusion** – material is selectively dispensed through a nozzle or orifice
4) **Material Jetting** – droplets of build material are selectively deposited; similar to inkjet printer but with photopolymers
5) **Sheet Lamination** – sheets of material are bonded to form an object
6) **Vat photopolymerization** – liquid photopolymer in a vat is selectively cured by light-activated polymerization
7) **Binder Jetting** – a liquid bonding agent is selectively deposited to join powder materials

Each individual AM process may have many advantages and disadvantages. Binder Jet, for example, can print a wide variety of materials including metals, ceramics, and sands and can typically do this much faster than other AM techniques which might also be able to fabricate a similar depth of material range, such as selective laser melting (SLM) [2]. Binder jetting utilizes inkjet-printing technology to fabricate a 3D component by selectively depositing a binder into a powder bed in a layer-by-layer wise fashion. During the printing process, powder material is spread across the build platform using a roller. Once the powder layer has been uniformly spread, a print head will selectively deposit the adhesive binder where required. The layer is then partially cured to “bind” the powder and then the build platform is lowered by the desired layer thickness so that the entire process may be repeated until a full 3D part has been fabricated. Once finished, the powder bed is removed and the printed part undergoes a final curing process to fully set the binder. The fully cured build can then be de-powdered from the print bed.

The ability to net-shape hard ceramics without a significant heat source makes binder jet a unique and attractive process for the fabrication of cermets [3]. A cermet consists of a metallic matrix reinforced with a secondary phase (typically a ceramic such as carbides, nitrides, or oxides) so that a single material is created which

combines metallic properties (ductility and toughness) with ceramic properties (high strength/modulus). The use of particulate reinforcement additionally yields isotropic properties while simultaneously keeping cost low, but particulate agglomerate can also be a potential challenge. This combination results in a unique material that has mechanical properties that may operate at higher temperatures than the base metal. This makes ideal materials for applications in aerospace, automotive, tooling, and other structural applications [4] .

Using binder jet, the ceramic reinforcement particulate is printed in the final shape of the desired component; a porous “preform”. The metallic matrix is then incorporated into the preform using liquid state processing, such as melt infiltration, where the liquid metal wicks up into the ceramic preform. The end result is ideally a fully dense cermet that has retained its printed shape with little to no volumetric shrinkage. Much of the research focus with binder jet currently is with single alloy metals where densification occurs by shrinkage during sintering, but a large hurdle with these materials is distortion during shrinkage. However, with cermets, densification occurs by the filling of void porosity in the preform and is therefore able to largely mitigate shrinkage. There may still be some shrinkage that occurs during processing of cermets in this manner but the final shape remains intact.

Pressure-less melt infiltration, a liquid state process, is an attractive method for fabricating composites without the use of an external force. This process is comprised of a liquid melt that wicks into the porous ceramic preform. In the case of a wetting system (i.e. the metal wets the ceramic phase and has a contact angle < 90°), Infiltration will happen spontaneously due to capillary forces and requires no external pressure (pressure-less melt infiltration). However, if the metal does not wet the ceramic phase (contact angle >90°) then an external force is required to wick the melt into the preform (forced infiltration). This can be achieved by pressurized gas, a die (squeeze casting), or vacuum. Pressure-less melt infiltration lends itself nicely to be paired with binder jet for several reasons. The first, as stated previously, is that densification occurs by the filling of void porosity and avoids the risk of shape distortion during traditional shrinkage. Secondly, pressure-less melt infiltration does not require the use of any specialized equipment and is therefore a cost-effective process that has the potential for scalability. A typical set-up would consist of setting the printed ceramic preform on a bed of powder within a crucible and running a furnace cycle at the required temperature to melt the metal powder, at which point the metal wicks into the preform to achieve the final composite. Pairing binder jet with pressure-less melt infiltration ensures that the entire process from print to final component remains cost-effective compared to traditional manufacturing.

The aim of this research is to utilize binder additive manufacturing and melt infiltration to fabricate near-net-shape cermets consisting of a nickel aluminide (Ni_xAl_y) matrix reinforced with titanium carbide (TiC) particles. In addition, an attempt will be made at gaining a better understanding of the underlying phenomenon and kinetics that are present during the infiltration process so that this knowledge may be

applied to other material systems. It will be shown that by utilizing these techniques, a cermet consisting of the materials above can be fabricated in a near-net-shape fashion with little to no volumetric shrinkage. The data will form a pathway to develop design tools for binder jetting.

2 Literature Review & Background

This chapter will describe the in-depth information necessary to understand the studies presented in this thesis as well as review literature. Section 2.1 will provide an overview of metal matrix composite materials in order to provide an overview of the chosen material system. Section 2.2 will examine the materials studied in this work, $NiAl_3$ and Ni_3Al, and the motivation for this choice. In section 2.3 the Binder Jet additive manufacturing process will be discussed and the reasons for choosing a Binder Jet and melt infiltration combination process. The chosen densification method of melt infiltration will be described in section 2.4. And finally, a review of the concept of wetting and the importance in relation to cermets will be presented in section 2.5. Overall, this chapter will present the motivation for the chosen material system and the selected fabrication methods.

2.1 Metal Matrix Composites – Cermets

A metal matrix composite (MMC) is defined as a metal matrix combined with a secondary heterogeneous phase (metal or ceramic) to create a single material with properties that exceed either of the single phases. Typically, a metal will be reinforced with a ceramic material thus combining metallic properties (ductility and toughness) with ceramic properties (high strength/modulus); known as a "cermet" [4]. Cermets can be generally classified by their reinforcement type, including fibers (high aspect ratio), platelets/whiskers, and particulates (aspect ratio of ~1). Composites based on particle reinforcement are desirable for their relatively low cost compared to high aspect ratio reinforcements and ease of fabrication where fiber breakup is not an issue, and also their isotropic properties [4], [5]. A major benefit of particulate reinforced cermets is that not only can they undergo traditional metalworking techniques such as extrusion and forging but can also be produced by powder metallurgy (P/M) processes, which allows for the possibility of near-net-shape fabrication [5], [6].

While composites composed of a two metal system certainly exist and have their applications, overwhelmingly cermets are fabricated with ceramic reinforcements. The reason for this, as stated above, is that ceramics can impart their unique properties that a metallic matrix generally cannot offer alone including higher strength, higher operating temperatures and high temperature capabilities, and higher fatigue & hardness characteristics[4], [5]. Aluminum is perhaps the most widely used alloy as a matrix for cermets due its low density (2.7g/cc), good ductility, corrosion resistance (passivation by aluminum oxide), and low cost (commodity metal). By reinforcing aluminum with a low density ceramic such as SiC, the specific strength of aluminum may be greatly enhanced as well as its wear and fatigue resistance [7]. Nickel is another attractive matrix material for its high melting point

and higher strength compared to aluminum, but is more than 3x denser and is not corrosion resistant. The advantageous properties of both materials are combined within the various intermetallic phases of the Ni-Al binary system and are especially attractive materials for cermet matrices. Ni-Al intermetallics and their use in cermets will be discussed in the following chapters.

2.2 Nickel Aluminide Based Cermets

Intermetallic compounds, specifically those based on aluminum, have had significant interest for several decades due to their attractive properties including high strength, excellent corrosion resistance, and low density. This combination of properties makes them ideal structural materials for high temperature and/or corrosive environments where the potential application space is wide spread and may find promising use in aerospace, automotive, tooling, and other areas [8]–[13]. Compared to nickel based superalloys, these aluminides have lower density (~8.2 for Inconel 718 vs. ~7.2 for Ni_3Al, higher strength at elevated temperatures (UTS = ~950 MPa at 900°C and higher operating temperatures [11]. Although already attractive materials, combining these alloys with a ceramic reinforcement may yield a lower density, higher tensile strength, and improved creep and wear resistance [10]. In particular, the low density (4.93g/cc) and high hardness (27-35 GPa) of TiC make it an excellent reinforcement for nickel aluminides [14]–[16]. For the Ni-rich intermetallics, a lower density can be achieved and thus an improved specific strength and stiffness. For the low density Al-rich intermetallic, the high hardness of TiC offers the potential for an excellent lightweight wear-resistant cermet. In doing so, the currently occupied material-property space, as described by Ashby, may be expanded through the use of hybrid materials such as the nickel-aluminide cermets that are discussed in this work [17]

The following section will discuss on the metallurgy of nickel aluminides and their role in composite materials. Previous fabrication methodologies of these materials in literature, specifically TiC reinforced, will be discussed and serve as the bridge into the unique processes used to fabricate the composites described within this work.

2.2.1 Ni-Al Binary System

The three primary intermetallic phases within the Ni-Al binary system are the Ni-rich phases (Ni_3Al and NiAl) and the Al-rich $NiAl_3$, shown in Fig. 2-1. The majority of research into nickel aluminides has focused on the two Ni-rich phases, Ni_3Al and NiAl, due to a combination of attractive properties including high melting points and the

ability to retain strength at elevated temperatures as a result of their simple, ordered crystal structures. This combination of properties has earmarked nickel aluminide based materials for high temperature structural applications such as gas turbine engine components.

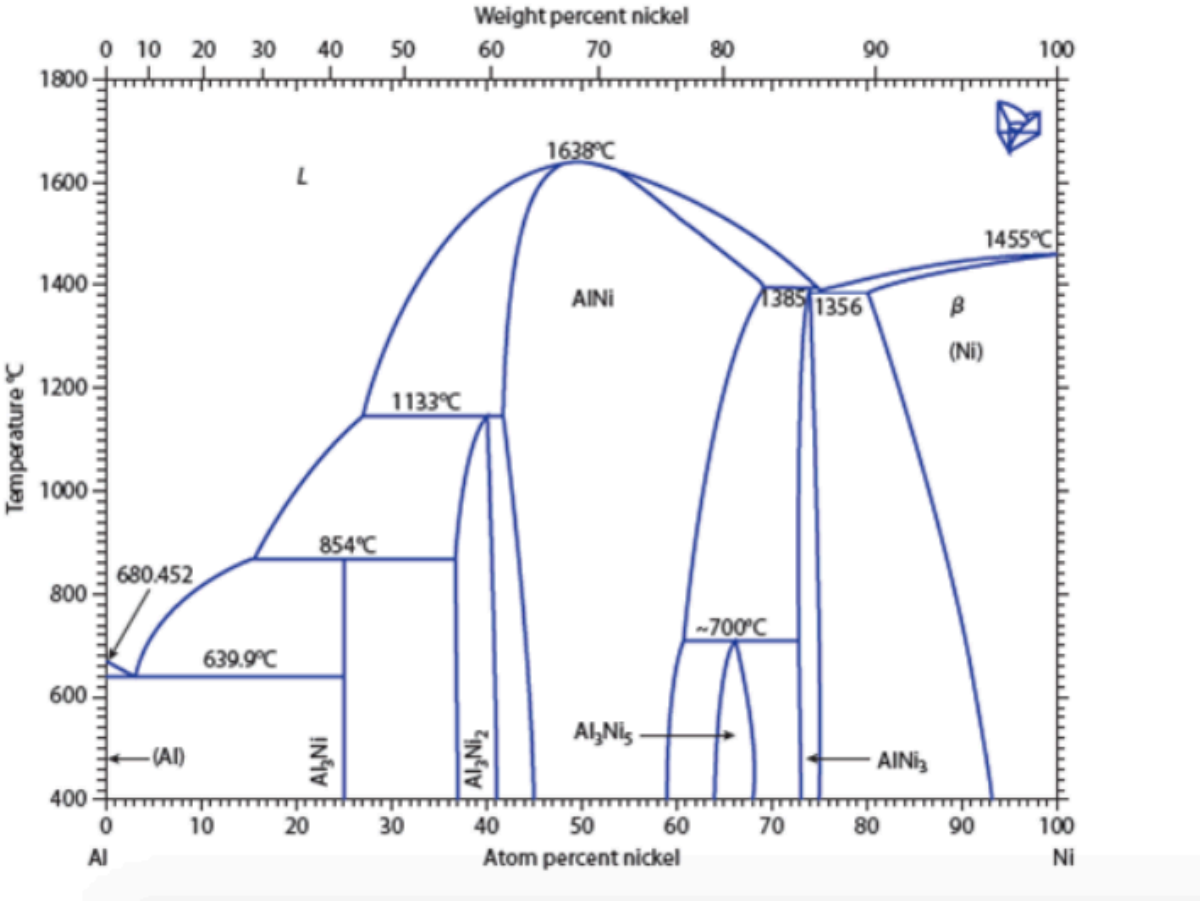


Figure 2-1 Ni-Al binary phase diagram [18]

As previously mentioned, due to a high Al content, all three intermetallic phases are able to passivate by the formation of a stable layer of aluminum oxide, which lends to their use in corrosive (ex. aqueous) environments[11]. Unlike conventional alloys and nickel-based superalloys, nickel aluminides do not depend on chromium oxide for corrosion resistance, which is unstable at elevated temperatures [19]. This is similar to alumina forming austenitic (AFA) stainless steels, which also use alumina in addition to chromium oxide to allow for higher operating temperatures. Additionally, the chemistry of the Ni-Al intermetallics is very simple compared to nickel superalloys or even steels. The two phases investigated in this work, Ni_3Al and $NiAl_3$, and also their use as a matrix for TiC-reinforced composites will be discussed further.

2.2.2 Ni_3Al and $NiAl_3$ Phases

Within this class of Ni-Al intermetallic phases, Ni_3Al has received by far the most attention and research focus. This phase may be better well known as γ', the primary strengthening phase in nickel-based superalloys and is responsible for the high temperature strength and creep resistance of these superalloys [20]. The alloy consists of 75 at. % Ni and 25 at. % Al, but may exist over a narrow range (~73-76 at. %) and has a melting point of ~1395°C. Ni_3Al has a simple, long-range ordered $L1_2$ crystal structure based on an FCC unit cell where the Ni atoms preferentially reside on the cubic face positions while the Al atoms reside on the corner positions [21]. Perhaps the most attractive property of the alloy is that the yield strength increases significantly up to ~850°C and that the wear resistance shows a similar trend with temperature. The unique strength retention is derived from the low atomic mobility of the crystal structure [10], [11]. Ni_3Al has a density of 7.25 – 7.5 g/cc depending on the stoichiometry; lighter than other nickel superalloys.

However, this alloy displays low ductility and a brittle fracture mechanism of intergranular failure at ambient temperatures and tackling this problem was a driving force in the research on this alloy. It was discovered in the 1970's that alloying with small amounts of boron could significantly increase the room temperature ductility of this material. Later on, it was found that chromium additions could further enhance the ductility of Ni_3Al at moderate to high temperatures [11]. These advancements made feasible the use of Ni_3Al as a matrix material for cermets and will be discussed further.

Compared to Ni_3Al, the Al-rich $NiAl_3$ has received very little attention in literature. In the context of the application space for Ni_3Al as a high temperature structural material, this makes sense. $NiAl_3$, consisting of 25 at. % Ni and 75 at. % Al, has a low melting point of 854°C and similar ductility compared to Ni_3Al, which make processing difficult. Unlike Ni_3Al and NiAl, which have simple cubic crystal structures, $NiAl_3$ forms in the complex orthorhombic primitive unit cell $D0_{11}$ cementite (Fe_3C) crystal structure. The unit cell consists of 16 atoms with 4 Ni and 12 Al atoms. The brittle nature of this alloy at low temperatures can likely be attributed to its complex crystal structure, where plastic deformation via dislocation glide may be more difficult compared to other alloys with more simple structures due to the absence of planar slip planes [22]. However, more complex crystal structures generally exhibit higher hardness values and $NiAl_3$ does indeed have a higher reported hardness (~7000-8000 MPa) than Ni_3Al (< 4000 MPa) [23], [24].

Combined with its low density (3.96g/cc), $NiAl_3$ might be applied as a lightweight tooling material. Despite the lack of research on the Al-rich intermetallics of the Ni-Al system, there has been experimental study on the use of $NiAl_3$ as a reinforcement phase in Al-based composites. This owes to the low density and high hardness of the alloy but also due the metallic bonding achieved between the Al matrix and $NiAl_3$ reinforcement. Peng et. al demonstrated that by the addition of up to

10 wt.% nickel to the 7050 series aluminum alloy, $NiAl_3$ could be precipitated in the Al matrix resulting in a significant increase in hardness, up to ~2300 MPa. The hardness of the base 7050 alloy is ~180 MPa [25]. Similar work has also been conducted on 2000 series aluminum alloys Beyond this, there is no known mention in the literature of the use of $NiAl_3$ as a matrix metal for cermets.

2.2.3 Ni_3Al-TiC Cermet Fabrication in Literature

TiC reinforced Ni_3Al cermets have been produced by a myriad of processing methods including powder metallurgy (P/M)[26]–[29][30], liquid state processing such as melt infiltration [31]–[37], and in-situ sintering methods [36], [38]–[41]. Much of the research on this material was conducted at ORNL as far back as the early 1990's and is the basis for the methodology used in the present work. The fabrication methods present in literature will be discussed in this section. There exist considerably more research efforts on the fabrication of Ni_3Al based cermets including the use of Al_2O_3, SiC, WC, and TiC reinforcements. For the sake of this review, only the fabrication of Ni_3Al-TiC composites will be discussed. The decision to use TiC reinforcement will be discussed more in depth in later sections, but the primary reason is due to its superior mechanical properties and high melting point and also its partial metallic bonding character.

2.2.3.1 Ni_3Al-TiC Fabrication by P/M & In-Situ Synthesis

Initially in 1996 Tiegs, Plucknett, and Becher fabricated Ni_3Al-TiC composites containing 17 vol.% binder (Ni_3Al) by ball-milling TiC and Ni_3Al powders and then consolidated by hot pressing at 1150-1450°C to an unreported density. Ni_3Al was found to wet TiC well with a reported wetting angle < 15°, where densification occurred by liquid phase sintering and particle re-arrangement. Micro-hardness, flexural strength, and fracture toughness were characterized; summarized in Table 1 [26]. Liu et al. achieved Ni_3Al (~55 vol.%)-TiC composites exceeding 98% theoretical density by vacuum sintering under high-pressure with mixtures of Ni, Al, Ti, and C powders [38]. Recently, Stewart, Plucknett, and Memarrashidi have utilized an in-situ press and sinter approach where TiC powder was blended with Ni + NiAl powder and then pressed at 45 and 207 MPa respectively and then subsequently sintered at 1550°C for 1 hour to achieve a composite with binder content ranging from 20–40 vol.%. A sintered density exceeding ~98% theoretical was achieved and Vickers hardness, sliding wear behavior, and aqueous corrosion response were studied [39], [41].

Chen et. al utilized a unique mechanically-induced self-sustaining synthesis reaction (MSR) process to fabricate TiC-Ni_3Al composites with Ni_3Al content ranging

from 20-50 vol.%. The MSR process uses the high amount of heat released during reactions between the elemental powders during ball milling to stimulate self-propagating reactions that result in a homogenous composition of high purity. Ni, Al, Ti, C, and B powders were ball-milled until a synthesis reaction occurred, upon which the synthesized powders were consolidated by press and sinter. The noticeably higher flexural strength observed by Chen is attributed to the special "cleaning" of the TiC powder surface during MSR, by which it is described that the high surface porosity of commercially available TiC powders used in other studies may absorb contaminants and reduce wetting by the Ni_3Al binder thereby increasing porosity at the binder/TiC interface, which flexural strength is very sensitive to [40].

While it has been shown that Ni_3Al-TiC composites may be prepared by P/M techniques where densification occurs by shrinkage during sintering, this methodology is not directly applicable to the near-net-shape fabrication methods presented in this thesis. Hence, literature that describes the fabrication of Ni_3Al-TiC composites by melt infiltration techniques where densification is achieved by filling of void porosity will be discussed more in depth.

Table 1 Reported mechanical property data for Ni3Al-TiC cermets fabricated in literature. Originally compiled in this work

	Material (Vol. % Ni_3Al)	**Density (%)**	**Hardness (GPa)**	**Flexural Strength (MPa)**	**Fracture Toughness ($MPa/m^{1/2}$)**	**Elastic Modulus (GPa)**
Tiegs, Plucknett, Becher [16]	17		16 - 20	750 - 900	8 - 14	
Plucknett, Becher [21]	20	> 96		1360		
Becher, Plucknett [22]	8 - 40	> 96	17.2 - 14.6			430 - 370
Stewart, Plucknett [29]	30	> 98	10.3 - 12.5			
Collier, Plucknett [25]	20 - 50	> 99	12.3 - 19.2			
Collier, Plucknett [34]	10 - 50	> 99				428 - 319
Liu et. al [28]	55	> 98	5.6 - 7			
Chen [30]	20 - 50	> 98	14.5 - 9.8	1220 - 2165	8.7 - 17.5	
Pan [23]	10 - 40			925 - 1476	7.6 - 20.4	
He et al. [26]	> 45		0.57 - 0.6	1113 - 1017	10.5 - 9.7	380 - 420
Zhang et. al [32]	20 - 80	> 98		587 - 1468		318 - 266

2.2.3.2 Ni_3Al-TiC Fabrication Liquid State Processing: Melt Infiltration

The fabrication of Ni_3Al-TiC composites by liquid state processing was first described by Plucknett and Becher in 1997, where composites with 8-40 vol.% Ni_3Al content were fabricated by either a melt infiltration or melt infiltration-sintering technique. A melt infiltration-sintering technique simply involves using less metal infiltrate than is required to fill the entire porosity of the preform where densification then occurs both by filling of void porosity and shrinkage. TiC preforms of ~60% green density were prepared by cold isostatic pressing (CIP) TiC powder. Ni_3Al pellets were then placed on top of the preform and melted where the metal then "wicked" downward into the TiC preform driven by both capillary and gravitational forces to achieve near full density. If enough Ni_3Al to fill the entire void space of the preform was used then consolidation was achieved by filling of void porosity (infiltration). If lesser amounts of Ni_3Al were used then both filling of void porosity and also liquid phase sintering of the TiC preform achieved consolidation (infiltration-sintering). Notably, Plucknett and Becher showed that when filling of porosity dominated densification the linear shrinkage of the composite was < 7%, low enough to be considered near net shape. Low and high temperature flexural strength testing was conducted by use of a four point bend test in addition to fracture toughness, elastic modulus, and oxidation behavior on the fabricated Ni_3Al-TiC composites; summarized in Table 1 [31], [32]. The same methodology was used by Holmes et. al to fabricate Ni_3Al-TiC composites of >99% theoretical density with binder content of 10-40 vol.%, where the electrochemical corrosion behavior was studied [37].

In later publications, Plucknett and Becher reported contact angles of 25°-35° for samples held at 1400°C, confirming excellent wetting of TiC by liquid Ni_3Al. Interestingly, it is also reported Ni_3Al infiltration into the TiC preform occurs considerably slower than predicted by the classic Lucas Washburn equation. Plucknett and Becher attribute this phenomenon to chemical dissolution of TiC in liquid Ni_3Al thus altering the liquid surface energy and viscosity of the metal binder by enrichment of titanium (< 7 at.%) and carbon, with a carbide composition of $TiC_{0.93}$ [34].

He and Zhu utilized a similar methodology to infiltrate Ni_3Al into a Ni_3Al/TiC preform fabricated by self-propagating high-temperature combustion synthesis (SHS), similar to the MSR technique published by Chen et. al. Preforms with 20/30 vol.% Ni_3Al were created and it was demonstrated that the wetting of the liquid Ni_3Al binder was improved for the Ni_3Al/TiC preform compared to the normal TiC preform. Composites of ~45 vol.% Ni_3Al binder infiltrated into a 20/30 vol.% Ni_3Al/TiC preform were reported as fully dense with no defects. Microstructures were characterized based upon changing infiltration temperature and times and found that a sound, defect-free microstructure could be obtained at high temperatures with shorter infiltration time and vice versa. He and Zhu note that instead of a uniform dispersion, TiC particles within the preform make up a dimensionally connected network that was retained

after infiltration by Ni_3Al [36] A similar TiC network structure was reported for hot pressed Ni_3Al-TiC composites by Zhang et. al and correlated to a higher Young's modulus and Poisson's ratio at particular binder vol. %. Additionally, it has been shown that interconnected network formed by the ceramic reinforcement could result in higher fracture toughness [42], [43]. Based upon the findings from He and Zhu and Zhang, it is likely this network structure is present in other studies but simply not reported on.

2.2.3.2.1 Ni_3Al-TiC by Upward Infiltration

Pan et. al reported a similar process to Plucknett and Becher where a TiC preform prepared by pressing was infiltrated Ni_3Al, however, the Ni_3Al powder was placed below the TiC preform to facilitate "upward" infiltration rather than the downward infiltration process used by Plucknett and Becher. TiC discs were vertically placed in a crucible and surrounded by Ni_3Al pellets, which once liquid "wicked" up into the preform due to capillary action. The infiltration method used by Plucknett and Becher is not driven completely by capillary action since the liquid will flow downward due to gravitational forces as well. TiC preforms were pressed to ~60% green density and infiltrated with 10, 20, 30, and 40 vol.% of Ni_3Al binder equaling 25, 50, 75, and 100% of the open porosity within the preform. Similar to Plucknett and Becher, the contribution to densification by both infiltration and liquid phase sintering was studied, described by Pan as the real and nominal infiltration degrees. The real infiltration degree is defined as the total percentage of the pore volume filled by the metal binder represented by eq. 1, where k equals linear shrinkage of the composite (%). p_f is the calculated density of the infiltrated sample (g/cc), p_g is the green density of the preform (%), p_{NA} is the density of Ni_3Al, and p_{TiC} is the density of TiC (g/cc) [33].

$$f = \frac{(1-k)^3 p_f - p_{TiC} p_g}{p_{NA}[(1-k)^3 - p_g} \quad (1)$$

The nominal infiltration degree ignores k, where a difference in the real and nominal infiltration degree indicates a contribution by shrinkage (and hence liquid phase sintering) to densification. Maximum linear shrinkage of ~9% occurred at 20 vol.% binder indicating consolidation achieved partially by liquid phase sintering. When the densification was done completely by filling of void porosity (40 vol.% binder), the linear shrinkage was < 1%. TiC dissolution in liquid Ni_3Al was also documented and confirmed by the use of fast cooling rates (~50°C/min vs. 7.5°C/min in this work), where dissolved TiC in the binder was unable to re-precipitate as TiC and instead formed $Ni_3(Al,Ti)C$. In order for liquid phase sintering to occur the solid phase must have partial solubility in the liquid metal, therefore TiC dissolution in liquid Ni_3Al is to be expected to some degree. For equal volume fractions of Ni_3Al, Pan reported

faster infiltration times (20 mins for 40mm thick sample) and higher flexural strength and fracture toughness compared to Plucknett and Becher (reported in Table 1). This is attributed to the uni-directional infiltration front during “upward” infiltration, as opposed to a possible multi-directional front in downward infiltration where defects, such as solute pinning or gas porosity, will be trapped at the points of which infiltration fronts intersect. The conclusion is that Pan et al. demonstrated the advantages of using an upward infiltration process in terms of lowered processing times and increased mechanical properties [33]. Additionally, this process lends itself to the use of preforms with more complex geometries where the preform can easily be placed on a bed of metal powder regardless of shape.

2.2.3.2.2 Ni3Al-TiC by Slip Casting and Infiltration

Composites prepared by melt infiltration allows for potential near-net-shape fabrication that cannot normally be achieved by traditional P/M techniques. However, in the described literature above the TiC preforms are still fabricated by P/M or in-situ methods, which has geometrical limitations. Recently, Collier and Plucknett have described a process in which the TiC preforms to be infiltrated are made by an aqueous slip casting procedure where an aqueous TiC suspension is directionally cast into cylindrical molds to form the preform shape. The TiC preforms are then pressure-less infiltrated following the procedure described by Plucknett and Becher [31]. A hardness comparison between infiltrated composites with preforms prepared by both dry pressing and aqueous processing showed a ~4% increase in hardness for the slip cast preforms of equal binder content. [35], [44]. While preforms with only simple disc shapes were reported, this process could be used to fabricate more complex geometries similar to traditional casting. However, like conventional casting, this method may have difficulty with internal features or more organic shape designs.

Near-net-shape fabrication of Ni_3Al-TiC cermets by liquid state processing methods has been shown to produce fully dense materials with minimal linear shrinkage [27], [33], [34]. However, it is clear from the literature the ability to make these composites with complex geometries is critically lacking, with the studies utilizing simple, uniform thickness disc shapes. The methods proposed in this work utilize the infiltration methodology described by Pan et. al, but instead the TiC preforms are fabricated by binder jet additive manufacturing to achieve highly complex shapes. By combining Binderjet AM and pressure-less melt infiltration; Ni_3Al-TiC cermets with complex shapes can be fabricated in a near-net-shape fashion at low cost. An in-depth discussion of the Binderjet AM process will be described in the next section.

2.3 Binder Jetting

Binder jetting is an ink-jet AM process where a part is built in a layer-by-layer wise fashion where powder material is “fused” together by selectively depositing an adhesive binder material via inkjet. After each layer a partial curing cycle is run to partially “set” the binder in place. This process is repeated until a final part has been printed. After the print process has been completed, a curing cycle is used to fully set the binder in place, which imparts enough green strength to de-powder the part, where excess powder is removed from the build. At this point, the part may then be consolidated either by a sintering process or infiltrated with a second, lower melting point material. Generally, the part will be held at a lower temperature (< ~700°C) to burn off the binder phase before the temperature is increased to the sintering or infiltration temperature (ex. ~1000 - 1300°C for Inconel 718). The de-bind and infiltration cycles are conducted in two separate furnaces within this work due to the high temperatures requirements at which infiltration is conducted (> 1400°), which necessitates two different furnaces. A general process-flow is shown in Fig. 2-2.

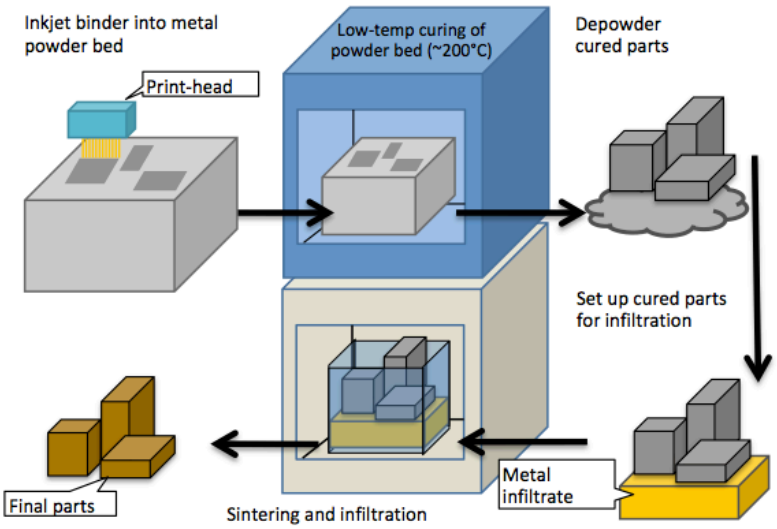


Figure 2-2 Cermet Process Flow for Binder Jet Additive Manufacturing & Melt Infiltration Processing

The basis for what is now called Binder Jet additive manufacturing was first developed and patented at the Massachusetts Institute of Technology (MIT) in 1993. In 1995, Z corporation obtained exclusive licensing rights to the inkjet technology, patented as “3DP” (3D Printing), and created their first inkjet technology printer called the Z402, which fabricated models using starch and plaster-based powders and a water-based liquid binder [45]. Currently, ExOne is able to fabricate a wide-range of materials with Binder Jet including nickel-based superalloys, stainless steels, tungsten carbide and other ceramic powders, and metal alloy blends such as stainless steel/bronze.

Binder jet additive manufacturing is classified as a powder bed AM process, where components are selectively fabricated from a bed of powder. Unlike powder bed fusion processes such as Selective Laser Melting (SLM) and Electron Beam Melting (EBM), which use a thermal energy source to melt and fuse powder together, inkjet AM like binder jet will instead selectively deposit a binder onto the powder bed where the part geometry requires. Binder jet's use of a roller provides a unique advantage where theoretically any powder size and distribution may be used for printing, including very fine and coarse particle sizes. Additionally, powder bed fusion processes require a build plate for stability since thermal stresses are introduced into the part that might result in warping or even cracking. Binder jet, which does not use a thermal energy source for shaping, requires no such build plate. Finally, the overall advantage is that print time is greatly reduced compared to other powder bed processes and this is magnified for a greater number of parts within a build [3]. A schematic of the binder jet machine process is shown in Fig. 2-3.

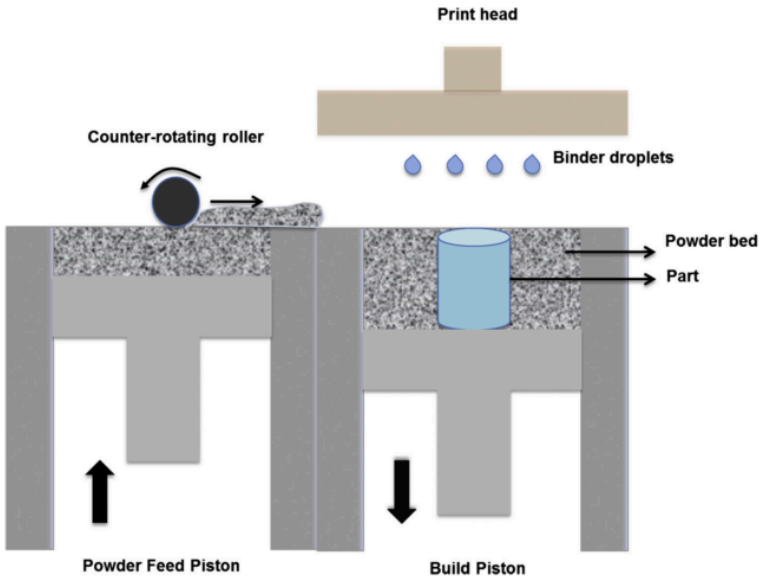


Figure 2-3 Schematic of Binder Jet Process. Courtesy of Nandwana et. al [46]

2.3.1 Powder Characteristics

In powder bed systems, the print density is determined by the packing factor (bulk density of powder divided by true density of powder) of the powder material feedstock. However, a disadvantage of the binder jet process, or any powder bed system, is the packing factor of the powder feedstock cannot be controlled by the machine itself, rather, the packing factor is determined mainly by the powder characteristics. Powder size, powder sphericity, surface roughness, and powder size

distribution can all affect the packing factor and by considering these parameters the print density may be optimized. For instance, it has been shown that using a bimodal powder size distribution can increase the final print density by up to 16% [47], [48]. In the case of binder jet, this means the printed preform has a limited range of densities for a specific powder feedstock. Ideally, the print density would be as high as possible in order to better facilitate densification during post-processing.

A challenge with binder jetting followed by sintering is the competing demands between the printing and sintering processes. The use of a fine particulate size may be advantageous during sintering of the printed part – a higher surface area promotes faster sintering kinetics [49]. A fine particle size, however, also provides difficulty during the printing process where a finer particle size is more likely to not pack as tightly, resulting in a lower density preform. In fact, within this original work, a higher preform density was achieved by simply using powder with a larger particle size. Powder size distribution as mentioned not only affects your packing factor but may also have an effect on your surface finish and also plays a role in setting your layer thickness. Finally, the powder characteristics of the material feedstock play not only a huge role in the print density but also in the print process itself, affect your binder saturation, layer thickness, roller speed, and safety concerns.

2.3.2 Binder Saturation

The volume of adhesive binder deposited into the powder bed during the printing process is set by the parameter called “binder saturation” and is determined based on the powder packing density. This parameter is expressed by the volume of the binder divided by the volume of open space within the powder (i.e. open porosity). The binder saturation is set by the operator and also depends largely on powder characteristics. Higher binder saturation will be required for powder material with a higher surface area. This means that powder with a fine particle size, rough surface, irregular shape, or very porous will need to have more binder. The operator may also adjust the binder saturation based on visual cues. Too high of a binder saturation and the powder particles will begin to stick to the roller and result in a non-uniform powder bed. Too low of a binder saturation and the risk of layer delamination is increased[46]. Once the binder saturation is set for a print and the operator is satisfied with the strength of the print, the saturation will be used for that specific powder feedstock for all future prints.

Currently, an organic binder is used for the printing process due to the need of a low burn-off temperature. However, due to the organic nature of the binder, it has been shown that residual carbon may be left behind after binder-burnout [46]. This also must play a role in determination of the binder saturation, as a higher saturation will result in more residual carbon left behind and therefore must also be considered with respect to the material system and secondary processing methods. Aluminum

may react with free carbon to form aluminum carbide (Al_4C_3), which is a deleterious phase that may not only negatively affect mechanical properties but is also a safety concern since aluminum carbide may react with water to form methane (a flammable hazard)[50].

It has been shown that carbon coating TiB_2 particles within a Ti matrix results in the formation of a TiC layer at the TiB_2/Ti interface, thereby preventing TiB_2 degradation and increasing mechanical properties. The residual carbon left from the binder could potentially be used in a similar fashion to form metallic carbides, discussed by Nandwana et. al in the fabrication of Inconel 718 by binder jet [46], [51]. The possible effects of residual carbon must be considered within this work since the cermets consist of an Al-rich matrix reinforced by a carbide reinforcement.

2.3.3 Preform Consolidation

The final product of the binder jet process is a porous preform with the desired shape of the final component. In this case, there are two methods for achieving full densification of the preform. For single alloy systems, such as steels, densification may occur by shrinkage during sintering. A secondary, moderately low melting point material may also be infiltrated into the porous preform where densification primarily occurs by filling of void porosity. For composite systems such as steel reinforced with bronze, densification may be a combination of both where void porosity is filled by the secondary bronze phase and the steel reinforcement experiences liquid phase sintering. It has also been shown in literature that by infiltrating with binder content less than the total pore volume, densification may occur by both liquid phase sintering and infiltration[33], [34] . However, composites based on refractory carbides will have great difficulty experiencing densification by shrinkage due to their high melting points, which necessitates either high sintering temperatures or densification by filling of void porosity. This makes binder jet additive manufacturing an ideal fabrication route for cermets where the secondary ceramic reinforcement is printed via binder jet in the desired shape of the part and the metallic matrix is infiltrated into the porous preform to achieve a fully dense near-net-shape component.

2.4 Densification by Sintering

Once the powder is shaped into a preform with binder jetting, it must be densified to reach desirable mechanical properties. Sintering is a crucial post-processing operation to achieve full solidification and porosity reduction in porous preforms printed by binder jet. As the final result of the binder jet process is a porous preform, there is a constant balance between achieving full densification while

controlling shrinkage in order to produce a dimensionally accurate near-net-shape part. Printing near-net-shape single metal alloys is a current challenge for binder jet due to the low print density of the process, which therefore requires significant shrinkage for consolidation. Refractory carbides are unable to be consolidated by solid state sintering without the use of very high sintering temperatures due to their high melting points. Zhang et. al reported that even under pressures of 30MPa, the sintering of TiC required temperatures up to 1700°C [42]. Consolidation of high temperature ceramics may be partially achieved with a liquid sintering aid, called *liquid phase sintering.* In order for liquid phase sintering to occur there must be some partial solubility of the solid phase within the liquid phase. Unlike solid state sintering where consolidation occurs by necking and bulk mass transport, liquid phase sintering may be classified by three distinct stages [52].

1. **Particle re-arrangement** - the liquid phase wicks into the "capillaries" between the grains and because of solid solubility, grains are re-arranged. Generally, this occurs very fast. Densification may slightly increase by more favorable packing factor
2. **Dissolution-reprecipitation** - as a result of the solid solubility of the solid phase within the liquid phase, smaller grains dissolve and precipitate on larger grains, thus grain coarsening occurs and as an extension – densification.
3. **Final densification:** densification occurs by continued grain coarsening and the elimination of porosity within the microstructure.

2.5 Densification by Melt Infiltration

Densification by filling of pore volume, i.e. infiltration, is a consolidation method where a second, heterogeneous liquid phase fills the pore volume of the primary solid phase. Infiltration can be either a spontaneous or forced process depending on the wetting characteristics of the system. If insufficient liquid phase is used for the infiltration process, partial densification may also occur by liquid phase sintering of the solid phase. Cermets are commonly fabricated by melt infiltration techniques because of the relatively lower melting point of the metallic matrix compared to the ceramic reinforcement (TiC ~3150°C, WC ~2900°C). The low melting point of lightweight metals such as Al (~660°C) and Mg (~650°C) especially make infiltration an attractive fabrication method for cermets based on these metals. Advantages of using a melt infiltration process is that it lends itself to the near-net-shape fabrication of more complex geometries and can be a more economical process in terms of processing times and cost compared to solid-state techniques [5], [53], [54].

The methodology used in this work utilizes the melt infiltration process to incorporate a liquid nickel aluminide binder into a porous TiC preform prepared by binder jet. Specifically, a pressure-less melt infiltration process detailed by Pan et. al

[33] is used to reduce processing time and cost. In the following section, the melt infiltration process will be reviewed including pressure-less in section 2.5.1 forced infiltration in section 2.5.2.

2.5.1 Pressure-less Infiltration

Pressure-less infiltration, commonly referred to as “spontaneous” infiltration, is a liquid processing method by which a liquid infiltrate wicks into a solid, porous medium (preform) driven purely by capillary forces without the use of an external force. This method is only possible if the liquid phase displays a wetting behavior on the solid phase, typically described by a solid-liquid contact angle < 90°. In reality, factors such as surface roughness and pore shape can alter contact angle such that a wetting to non-wetting transition may occur at angles below or above 90° [55]. For a solid-liquid interface, the angle of the edge of a liquid phase against the solid surface is the “contact angle”. The contact angle can be described using the Young equation (eq.1) as a function of the surface energy of the solid, surface tension of the liquid, and the solid-liquid interface energy.

$$cos\theta = \frac{\gamma_{sv}-\gamma_{sl}}{\gamma_{lv}} \tag{2}$$

The driving force of a liquid to infiltrate the porous media is known as the “capillary pressure” and represents the pressure difference across the interface of two immiscible phases within a capillary: the “wetting phase” and the “non-wetting” phase. Mathematically, the capillary pressure can be represented by equation 2, where p_{nw} is the pressure of the “non-wetting” phase, which is typically the vapor phase being displaced within the capillary tube and p_w is the pressure of the wetting phase. In order to drive the infiltrate material into the preform, the pressure outside of the liquid phase in the capillary must be higher, thus a positive pressure drives the fluid into the capillary.

$$p_c = p_{nw} - p_w = \frac{2\gamma_{lv}}{r} \tag{3}$$

The capillary pressure can be further described as a function of contact angle, θ, by the Young-Laplace equation (eq. 4) [56]. The interfacial tension of the liquid and the pore radius of the capillary are represented by γ and *r*, respectively.

$$p_c = p_{nw} - p_w = \frac{2\gamma cos\theta}{r} \tag{4}$$

It can be seen from Eq. 3, that if a contact angle is < 90°, i.e. “wetting”, then the capillary pressure will be positive and there will be a driving force for the liquid to infiltrate the preform. Conversely, if the contact angle is > 90°, then the system is said to be “non-wetting” and the capillary pressure will be negative and there will be no driving force for the liquid to infiltrate the porous media.

The capillary flow of the liquid infiltrate can be classically described by the Lucas-Washburn equation (eq. 4), which describes the time required, *t*, of a liquid to infiltrate a distance, *h,* and is related to the pore radius of the capillary, *r*, contact angle, θ, and viscosity of the liquid, η. Essentially, this equation expresses the capillary flow of the fluid versus viscous drag [56].

$$h^2 = \frac{\gamma r t cos\theta}{2\eta} \tag{5}$$

h – height of infiltration (m), t – time of infiltration (s), r – capillary pore radius (m), γ – liquid surface tensions (J/m^2), η – melt viscosity (N-s/m^2), *cos* θ – contact angle of liquid on solid. By virtue of this relationship it can be seen that an increased infiltration rate can be achieved by changing the viscosity and/or surface energy of the liquid. Increasing the infiltration temperature can be advantageous for capillary flow by lowering the viscosity, especially for particularly viscous liquids [56]. Surface energy of the liquid can change if there is chemical interaction at the interface of the liquid infiltrate and solid capillary, such as chemical dissolution or the formation of a reaction product. Plucknett and Becher reported longer infiltration times than predicted by the Lucas-Washburn equation as a likely result of changing surface energy due to chemical interaction at the interface [34]. Additionally, Muscat et. al reported a dynamic wetting behavior with changing surface energies and contact angle for TiC infiltrated by aluminum [57], [58]. However, there are limitations with the Lucas-Washburn equation in describing capillary flow. Firstly, for small infiltration times approaching zero the fluid velocity is high and not feasible, which results from neglect of an inertial term. Secondly, because there is no consideration for gravitational forces, the Lucas-Washburn equation will allow a fluid to infiltrate theoretically any height [59]. Martins et al. have proposed a new model that expands upon the Lucas-Washburn equation to include both an inertial and gravity term, shown by equation 6 below [60]

$$h^2 = t\frac{\rho r^2}{4\eta}\left(\frac{2\gamma_{LV}cos\theta}{\rho r} - gh\right) \tag{6}$$

p – density of liquid (g/m^3), *g* – gravitational constant (m/s^2). By considering equations 4 and 5, it can be seen that the infiltration process is a function of both chemical and geometric factors. As described above, the capillary pressure and infiltration rate are both affected by material chemistry in the form of surface energies

and viscosity. From a geometry standpoint, reducing the pore radius of the “capillary” will increase the capillary pressure and driving force for infiltration.

2.5.2 Pressure (forced) Infiltration

When there is no driving force for infiltration due to poor wetting behavior, the use of an external applied force may be used to overcome the negative capillary pressure, called the “intrusion” pressure in order to force the infiltrate into the preform. The more negative the capillary pressure, the greater the applied pressure must be to meet the intrusion pressure. This external force may be applied by several methods including gas pressure infiltration, squeeze casting, and pressure die infiltration [61], [62] .

During gas infiltration, a high-pressure gas is used to force the infiltrate material into the preform. This process has the benefit of using quasi-hydrostatic pressure so the green strength of the preform does not need to be very high. Additionally, there is no need for complex tooling or ram; only a vacuum pump. [63]. Squeeze casting is a traditional liquid phase processing method that combines casting and forging to produce a high strength part that solidifies under pressure within the die.

Squeeze cast infiltration is an extension of this process where the porous preform is set inside the chamber and a high-pressure ram forces the liquid metal into the preform, which then solidifies under pressure. The high pressure of this process avoids the formation of gas and shrinkage porosities and produces a fully dense part. Additionally, squeeze casting produces a fine microstructure due to the rapid solidification under high pressure resulting in strengths similar to wrought or forged parts [63]. Unlike squeeze casting, which applies pressure to the entire surface of the liquid metal, pressure die infiltration utilizes a die casting procedure where the liquid metal is mechanically injected through a small channel into a die chamber containing the preform [64]. This procedure may also be known as indirect squeeze casting.

While pressure infiltration methods may be used to overcome poor wetting behavior, these processes require complex tooling and equipment compared to the economical pressure-less infiltration method. Additionally, the preforms printed by Binderjet have particularly low green strength due to their low density and may make processing under higher pressures difficult. However, as liquid metals do not typically readily wet ceramic solids, a pressure infiltration method is often required based on the selected material system. This raises the point that when considering a liquid metal fabrication process, the wetting nature of the system plays a crucial role in determining the appropriate processing method.

2.6 Fundamentals of Wetting

The importance of wetting in context of capillary flow and the melt infiltration process has been discussed. However, the importance of wetting extends beyond just the infiltration process itself. In this chapter, the fundamental theory behind the concept of wetting will be briefly discussed in order to provide a basic understanding of the importance that wetting plays not only in processing but also in material selection and properties of the composite.

As mentioned previously, a capillary pressure arises from the pressure difference caused by the interfacial tension between two immiscible fluids. Fundamentally, the interfacial tension can be understood as the competing forces of attraction on the surface molecules of the fluid. In order for the interface to minimize the surface free energy and maintain equilibrium, the pressure inside the fluid at the interface must be greater than the external pressure at the interface (equal to the pressure of the vapor phase) [65], [66]. This is why applying an external pressure on the interface can overcome poor wetting behavior; the external pressure is elevated greater than that within the fluid interface and thus the interface expands. If we consider a liquid droplet on a solid surface, shown in Fig. 2-4, the fluid interface can be thought of as being "pulled" along the solid surface so that the liquid droplet "spreads" along the substrate.

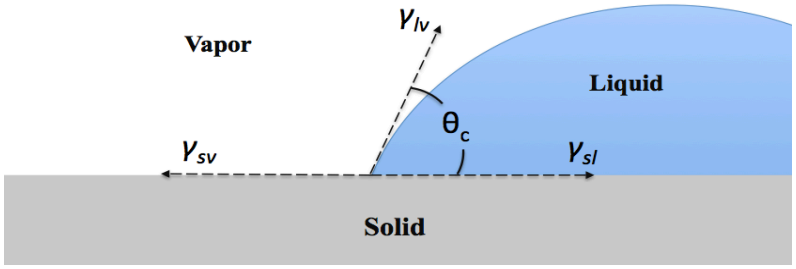


Figure 2-4 Liquid droplet on a solid substrate depicting the solid surface energy γ_{sv} , liquid surface energy γ_{lv} , solid-liquid interface energy γ_{sl} , and contact angle θ_c

Molecules at the surface of the fluid experience a greater attraction to other molecules within the fluid compared to dissimilar molecules of the solid or vapor phase and this is known as the cohesion forces of the liquid. In other words, the "cohesion energy" is the required energy to remove a molecule from the liquid phase into the vapor phase. Conversely, the attraction between the molecules of the liquid and solid phases at the interface is known as the adhesion forces. The "adhesion energy" is the work that must be done in order to separate the liquid and solid phases, represented by W_a. The work of adhesion can be related to the surface energies of the solid and liquid phases as well as the interfacial energy by equation 5. Thus, the work

of adhesion can be further related to the contact angle by equation 6 - known as the Young-Dupree equation [67], [68].

$$W_a = \gamma_{sv} + \gamma_{lv} - \gamma_{sl} \tag{6}$$

$$cos\theta = \frac{W_a}{\gamma_{lv}} - 1 \tag{7}$$

Fundamentally, the contact angle can be thought of as a representation of the balance between the competing adhesion (W_a) and cohesion ($2\gamma_{lv}$) forces at the solid-liquid interface. From the Young-Dupree equation it can be seen that a contact angle of 90° is obtained when the adhesion energy is roughly equal to the surface energy of the liquid - or roughly half of the cohesion energy of the liquid. If the work of adhesion is greater than the surface energy of the liquid, then a contact angle of < 90° is obtained and “wetting” is said to occur [55].

The adhesion forces may generally only overcome the cohesion forces if the interfacial bond is very strong, such as a chemical bond. Liquid metals do not typically wet ceramic solids for this reason; there is no established chemical bonding at the interface and the adhesion is based on weak van-der-Waals forces. Atoms of the liquid metal share a strong chemical bond by metallic bonding, while the atoms of the ceramic solid share a strong chemical bond by either covalent or ionic bonding. Liquid metals wet solid metals very well for the very reason that they share metallic bonding at the interface. Metals that do not share any miscibility are still able to achieve good wetting as a result of strong interfacial metallic bonding. In summary, liquid metals do not wet ceramic solids due to the difference in chemical bonding of the two phases.

2.6.1 Wetting of Ceramic Solids by Liquid Metals

In addition to the wetting of solid metals, liquid metal also wets the carbides, nitrides, and oxides of transition metals due to their mixed bonding characteristics [69], [70]. These carbides, such as TiC and WC, exhibit a mixed metallic-covalent-ionic bonding character dominated by metallic bonding, which allows wetting by liquid metals due to shared metallic bonding at the interface. The nature of the mixed bonding of transition metal carbides is very complex but the metallic binding is a result of the electron transfer from carbon to the un-filled d-shell orbital of the base transition metal [66], [70]. Additionally, the properties exhibited by these carbides such as high hardness and high melting points originate from the ionic and covalent bonding character of the carbide. In particular, the carbides formed by the transition metals of groups IV – VI exhibit a partial metallic bonding character and are known as

interstitial carbides. The difference between the electronegativity of the metal and carbon is very large and also the atomic radii of these metals is large enough such that the carbon atoms are interstitially located in the unit cell of the carbide. Generally, interstitial carbides exhibit a stronger metallic character than intermediate carbides, such as cementite (Fe_3C), where the carbon atom is too large to fit interstitially in the unit cell [71]. In contrast, SiC and B_4C are purely covalent carbides and thus are not wet by liquid metals. However, metals that react with carbon to form an interfacial reaction product will also generally react with SiC and B_4C in the same manner. An excellent example is the wetting of carbon by liquid aluminum, which reacts with carbon to form aluminum carbide (Al_4C_3) with strong metal-carbon covalent bonding. In the same manner, liquid aluminum will "wet" SiC and B_4C by the formation of Al_4C_3 at the interface, thus establishing a strong chemical bond by the formation of a reaction product [66].

For metal/ceramic systems, great wetting is achieved when a strong chemical bond is established at the interface of the liquid and solid phases by some reaction mechanism – either the formation of a new reaction product at the interface or dissolution of the solid phase by the liquid metal [55]. As mentioned above, aluminum will "wet" carbides by formation of Al_4C_3. However, the formation of a reaction product is generally avoided due to the deleterious effects on the properties of the composite [50]. Reaction in the form of carbide dissolution is then the preferred method to achieve good wetting at the interface. When considering metals that wet TiC (and other transition metal carbides) very favorably, transition metals with un-filled d-orbitals will react heavily to dissolve the carbide and form a solid solution. Such metals include Fe, Ni, Co, Cr, Nb, Zr, and Ti [72]. The heavy dissolution of TiC by nickel-based alloys is reported in literature, summarized in section 2.2.3, and also originally within this work. The motivation for TiC as a reinforcement phase is not only resulting from its excellent properties such as high hardness (27-35 GPa), high elastic modulus (~430 GPa), high melting point (~3100°C), and low density (4.93g/cc) but also due to the strong metallic bonding character that allows wetting by liquid metals [14]–[16], [73]. For liquid state processing methods where wetting is essential, TiC is an ideal reinforcement phase compared to the covalent carbides SiC and B_4C

2.7 Objectives of Current Research

It is clear from studying the literature that there is no methodology for the near-net-shape fabrication of Ni_xAl_y-TiC cermets with complex geometries. The goal of this work aims to present a new combination process based upon the methodology originally presented by Plucknett and Becher in order to facilitate the fabrication of more complex geometries. TiC preforms will be fabricated by binder jet additive manufacturing and then upward melt infiltration will be used to incorporate the nickel

aluminide binder. The use of binder jet additive manufacturing allows for the near-net-shape creation of preforms with complex geometries. Upward melt infiltration will allow full density to be achieved without significant shrinkage. Additionally, there is no known literature concerning the use of $NiAl_3$ as a matrix material for TiC cermets. The wetting behavior of Ni_3Al and $NiAl_3$ will be studied in context of their use as a matrix material for TiC cermets. By gaining a greater understanding of the dissolution and infiltration kinetics present during processing of Ni_xAl_y-TiC cermets, this knowledge may be applied to the similar fabrication of different material systems. One of the primary questions this work aims to answer is how will the difference in wetting behavior between $NiAl_3$ and Ni_3al affect the infiltration process?

3 Experimental Procedure & Materials

The following chapter will discuss the experimental procedures used to obtain the results presented in Chapter 4. The materials utilized in the preparation of samples will be discussed.

3.1 Materials

The TiC powder used as the primary material feedstock for the binder jet printing process was Ti-301 -325 mesh purchased from Atlantic Equipment Engineers (AEE). Ti-303 -100+325mesh was also purchased and used in preparation for TiC powder with a bimodal powder size distribution. The average particle size of the Ti-301 powder feedstock ranged from ~2um to ~30um between batches and was characterized using powder morphology analysis with a Malvern Panalytical Morphologi G3 microscope.

TiC powder feedstock with a bimodal size distribution was created by first sorting -325 mesh powder with a 100, 200, and 275mesh sieve, which resulted in powder sizes of > 75µm, 53 - 75µm, and < 53µm. The bimodal powder was then created by blending -325 mesh powder (~42g) with the 53 - 75µm size powder (~114g) in a ratio of 27/73 and ball milling.

For the first round of infiltration experiments, unmarked Ni_3Al and $NiAl_3$ powder at ORNL were used where XRD was used for phase confirmation. For later experiments, $NiAl_3$ powder was purchased from AEE – designation Ni-305 -325 mesh. Luvak Laboratories using direct current plasma emission spectroscopy – ASTM E 1097-12, measured the chemical composition of the two primary nickel aluminide powders – unmarked Ni_3Al and AEE $NiAl_3$ (Ni-305). The measured composition of each alloy is shown in Table 2.

3.2 Binder Jet Process

As mentioned previously, one of the goals of this work was to prepare a porous TiC preform to be used in infiltration experiments by binder jet additive manufacturing in order to show the ability to prepare potential complex geometries. The individual steps in this process will be discussed next.

Table 2 Chemical compositions of $NiAl_3$ and Ni_3Al alloys

Sample	Ni_3Al	$NiAl_3$
	Wt. %	Wt. %
Nickel	84.8	41.2
Aluminum	14.1	58.1
Boron	.0017	.0006
Zirconium	.20	.0057
Chromium	.075	.30
Molybdenum	.11	.0020
Semi-Quantitative		
Calcium	<.01	.023
Iron	.17	.054
Silicon	.24	<.01
Titanium	.028	.30
Tungsten	.17	.054

3.2.1 Printing Process

Each TiC print, including cups and bend/tensile bars were printed using a X1-Lab printer from ExOne, shown in Fig. 3-1. The printing process parameters for all builds were as follows: layer thickness set to a standard value of 100µm, binder saturation set to 85%, powder packing ratio varied between 35 – 40%, dryer intensity set to 90%, dryer time of 16 seconds where the width of the build plate is 40mm. De-powdering of the prints was done by hand with a small brush. Derek Siddel and Desarae Goldsby run the ExOne binder jet printers and were deferred to for all TiC prints within this work.

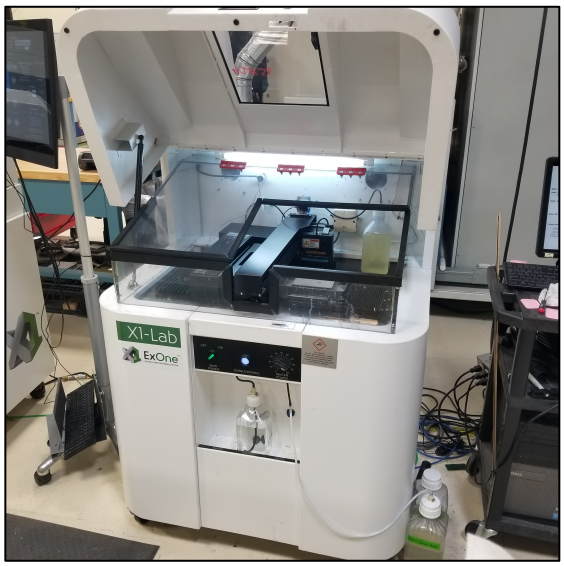


Figure 3-1 X1 Lab Binder Jet Printer from ExOne used for all TiC print

3.2.2 De-binding

De-binding of the printed TiC preforms was conducted after de-powdering in order to burn off the adhesive binder to prepare the preforms for further processing and consolidation. The de-bind cycle is shown in Fig. 3-2 and was conducted using a Neytech bench top furnace shown in Fig. 3-3. The sample is heated at 10°C/min to 630°C, held at temp for 1.5 hours, heated at 10°C/min to 900°C and held for an hour, then cooled to room temperature at 10°C/min. In some instances, de-binding of the preforms was simply done during the sintering procedure.

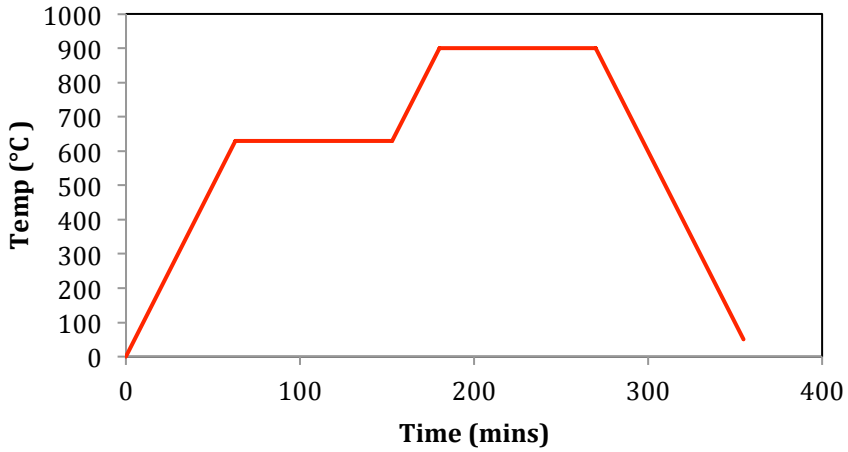


Figure 3-2 De-bind cycle for all TiC prints



Figure 3-3 Naytech bench top muffle furnace used for de-bind cycle of printed preform

3.2.3 Sintering Procedure

For experiments in round 1, in order to potentially increase the green density, the printed TiC cups underwent sintering at 1200-1500°C for 1-4 hours in a 265C CM Furnaces alumina tube furnace under Ar/4% H_2 (Fig. 3-7). It was found that minimal densification occurred even at the maximum temperature and hold time, no more than a ~2-3% theoretical density increase. As a result, TiC prints used for round 2 experiments and onward, including bend and tensile bars, were not sintered prior to infiltration.

3.2.4 Preform geometry

Ultimately, the purpose of using binder jetting is to fabricate the porous ceramic preform with complex geometries. To this end, a cubic cup geometry was designed that was simple enough for infiltration studies but contained features (i.e. walls) that varied in thickness. A picture of the print geometry is shown in Fig. 3-4. The dimensions of the preform varied slightly between builds. The original dimensions were 15 x 15 x 10mm with inner cavity dimensions of 10 x 10 x 5 for a total material volume of 1.75mm^3. Round 2 preforms had outer dimensions of 15 x 15 x 10mm with the inner cavity measuring 10 x 10 x 7.5mm for a total material volume of 1500mm^3; shown in Fig. 3-5. Both prints were done using -325 mesh powder with an average particle size of ~2um and ~30um respectively. The print quality of the part improved considerably from RD 1 to RD 2, which is thought to be a result of the better flowability of the larger particle size. Finer particles will tend to clump and fall out of the preform sporadically, which can be seen in the image below as indicated by larger holes alongside the outside. The dimensions of the original part geometry were kept constant for all builds, but it was observed that changing the layer thickness of the build based upon the average particle size resulted in the print software scaling the part by a small amount.

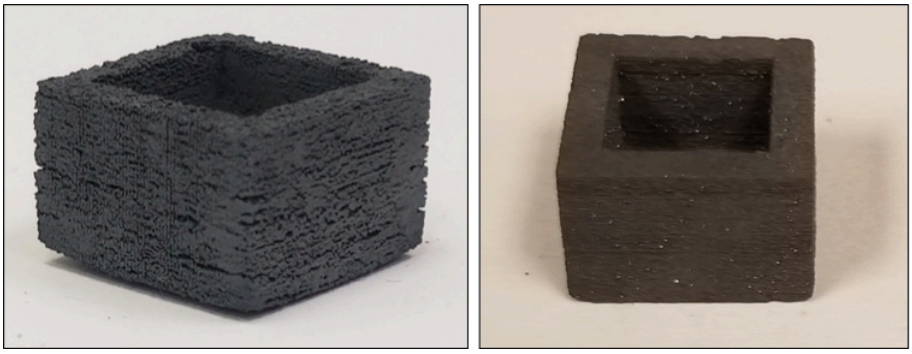


Figure 3-4 a) TiC preform ~30% dense RD 1. **b)** TiC preform ~50% dense RD 2

3.3 Infiltration Experiments

3.3.1 Infiltration Procedure

The infiltration procedure used in this work was adapted from the upward infiltration methodology described by Pan [33]. Nickel aluminide powder was first placed in a cylindrical alumina crucible and then the TiC preform was placed on top of the powder, shown in Fig. 3-5 with a quartz crucible for visibility. The methodology described by Pan used metal powder underneath the TiC preform only so that purely capillary forces drove infiltration. However, in this work, a few additional specimens were fabricated by adding metal powder to the cavity of the preform such that both capillary and gravitational forces drove infiltration. This was done for a comparison between the two infiltration techniques.

The alumina crucible containing the metal powder and TiC preform was loaded into a tube furnace and run under a specified cycle. An inert reducing atmosphere of Ar/4% H_2 was used to remove the aluminum oxide present on the metal surface. Attempted melting of the nickel aluminide powder under a 100% Ar atmosphere resulted in no melting and confirmed the requirement for a reducing atmosphere. Infiltration experiments were done using two furnaces, one at ORNL (dubbed Furnace 1) and one at UTK (Dubbed Furnace 2). Furnace 1 (Fig. 3-7) was a 265C alumina tube furnace from CM Furnaces with a max operating temperature of ~1600°C, heating rate of 600°C/hr (10°C/min), and a cooling rate of 7.5°C/min. Furnace 2 (Fig. 3-6) is an older CM Furnaces model similar to their 1730-12 HF alumina tube furnace with a smaller diameter tube with a max operating temperature of ~1600°C, heating rate of 400°C/hr (~6.67°C/min), and a cooling rate of 7.5°C/min.

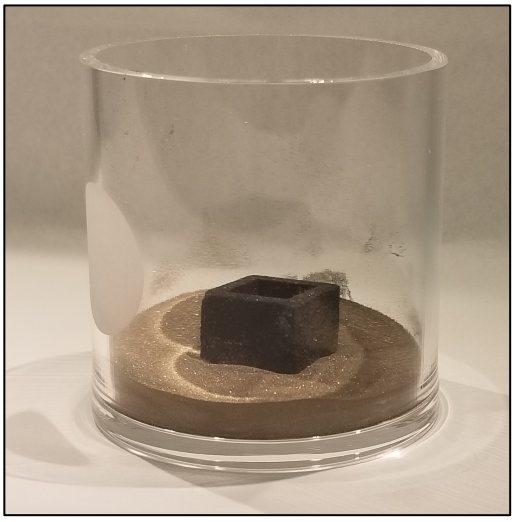


Figure 3-5 Printed TiC preform set on bed of Ni_3Al powder inside quartz crucible



Figure 3-6 CM Furnaces 1730-12 HF alumina tube furnace at UTK courtesy of Center for Materials Processing

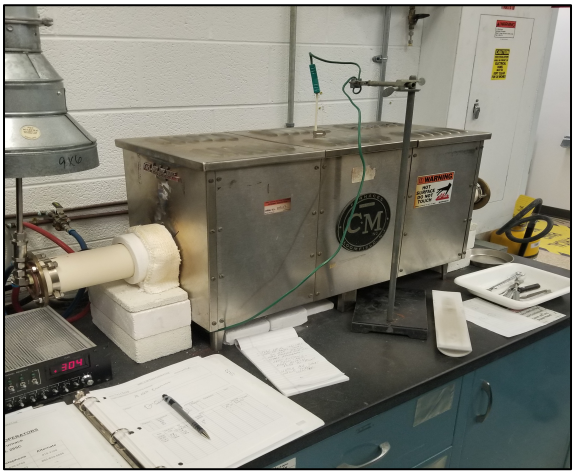


Figure 3-7 CM Furnaces 265C alumina tube furnace at ORNL

3.3.2 Round 1 Infiltration Experiments

Infiltration studies for round one of experiments consisted of 12 TiC cups printed with -325 mesh TiC powder; average particle size of ~2µm. The print density was determined by weighing each sample and was measured to be ~30% for each cup. The individual infiltration parameters used for each preform are detailed below in Table 3.

Table 3 Process parameters for Round 1 Infiltration Experiments. Sample 2 experienced discoloration during sintering. No melting of metal infiltrant occurred during infiltration of samples 3 and 4. No infiltration occurred for Sample 11; preform used for XCT characterization.

					Infiltration				
		Print Density (%)	Debind	Sinter	Temp (°C)	Time (min)	Alloy	Mechanism	Heating Rate (°C/min)
Build 1	Sample 1	~ 30	1500°C 1 hr		1500	30	Ni_3Al	capillary (c)	10
	Sample 2		1400°C 2 hr						
	Sample 3		1400°C 1 hr		1415	30	$NiAl_3$	c + gravity	10
	Sample 4		1400°C 1 hr		1415	30	$NiAl_3$	capillary	10
	Sample 5		900°C 1 hr	1450°C 2 hr	1415	30	$NiAl_3$	c + gravity	6.67
	Sample 6		900°C 1 hr	1450°C 2 hr	1415	30	$NiAl_3$	capillary	6.67
Build 2	Sample 7		1400°C 2 hr		1430	15	Ni_3Al	capillary	10
	Sample 8		1400°C 2 hr		1430	30	Ni_3Al	capillary	10
	Sample 9		1400°C 2 hr		1415	30	$NiAl_3$	capillary	6.67
	Sample 10		1400°C 2 hr		1430	30	Ni_3Al	capillary	10
	Sample 11		900°C 1 hr	1450°C 2 hr	900	30	$NiAl_3$	capillary	6.67
	Sample 12		900°C 1 hr	1450°C 2 hr	1415	30	$NiAl_3$	capillary	10

3.3.3 Round 2 Infiltration Experiments

Infiltration studies for round two of experiments consisted of twelve TiC cups - 6 cups printed using -325 mesh TiC powder (~30 µm average particle size) and 6 cups printed using TiC powder with a bimodal powder distribution. The initial goal of using a bimodal powder distribution was to further increase the print density of the preform, however, these samples printed to a similar density as those printed with the higher particle size -325 mesh powder. The print density was determined by weighing each sample and was measured to be ~50% for each preform. The individual infiltration parameters for each preform are detailed in Table 4. Each preform, excluding Sample 11 from RD 2, was de-binded according to the process described previously and was not sintered. Additional care was taken with RD 2 experiments in recording excess metal powder supplied for infiltration.

3.4 Characterization Techniques

3.4.1 Archimedes Immersion Density Measurements

Archimedes immersion method was used to measure the density of both as-printed TiC preforms and also the infiltrated cermets. Important to remember that Archimedes method only measures the open porosity of the sample. However, closed

porosity may be calculated by subtracting the measured open porosity and % theoretical density from 100.

Table 4 Process parameters for Round 2 Infiltration Experiments. No infiltration of Samples S2 and S6 occurred despite melting of $NiAl_3$. Sample 11 used for infiltration after XCT characterization. Samples that have yet to be infiltrated, particularly Samples B2-B6, will be used for future experiments.

				Infiltration					
		Print Density (%)	Debind	Temp (°C)	Time (min)	Alloy	Mechanism	Excess	Heating Rate (°C/min)
Build 1	Sample B1	~ 50	Y	1415	30	$NiAl_3$	Capillary	Y	6.67
	Sample B2		Y						
	Sample B3		Y						
	Sample B4		Y						
	Sample B5		Y						
	Sample B6		Y						
Build 2	Sample S1		Y	1430	26	Ni_3Al	Capillary	N	10
	Sample S2		Y	1000	30	$NiAl_3$	Capillary	Y	6.67
	Sample S3		Y						
	Sample S4		Y	1200	30	$NiAl_3$	Capillary	N	6.67
	Sample S5		Y	1200	30	$NiAl_3$	Capillary	Y	6.67
	Sample S6		Y	1000	30	$NiAl_3$	Capillary	N	6.67
RD 2	Sample 11	~ 30	Y	1430	26	Ni_3Al	Capillary	N	6.67

3.4.2 Microscopy

Infiltrated samples were sectioned using an Allied High Tech Products Inc. Techcut 5™ precision high-speed saw with a 8" IsoMet® diamond wafering blade and then mounted in a conductive epoxy using a Buehler SimpliMet™ 3000 automatic mounting press. The mounted samples were then prepared for general microscopy using the following grinding and polishing procedure:

- Piano grinding disc: 120 grit -> 220 grit -> 600 grit -> 1200 grit
- MD-ALLEGRO polishing disc: 6µm diamond suspension
- MD-LARGO polishing disc: 6µm diamond suspension
- MD-DAC polishing cloth: 3µm diamond suspension
- MD-NAP polishing cloth: 1µm diamond suspension
- MD-NAP polishing cloth: 0.5µm diamond suspension (EBSD only)

The piano grinding discs are specifically used for high wear resistance materials to prevent "rounding" of the sample during grinding/polishing. For EBSD prep, following the described polishing procedure, samples were then placed on a vibratory polishing machine for 5-6 hours in a suspension of 50% colloidal silica and 50% distilled water.

Optical microscopy of the infiltrated samples was done using a Leica DM4000 M LED upright microscope. Images were captured at 5x and stitched together using the multi-step capability within the Leica Application Suite software.

Both a Hitachi 3400 and S4800 scanning electron microscopes were used to image samples at higher magnifications. Imaging was typically done using a 15kV voltage at magnifications ranging from 30 – 5000x. Energy Dispersive X-ray Spectroscopy (EDS) capabilities of each system was used for chemical phase analysis of the composite microstructure.

3.4.3 Electron Backscatter Diffraction (EBSD)

EBSD was used for crystallographic analysis of the infiltrated preforms and was done using a JEOL 6500 operating at 20keV. Crystallographic phase information (CIF) files for each phase were sourced from the Inorganic Crystal Structure Database (ICSD). Sample preparation is described in the previous section.

Analysis of the collected electron diffraction patterns was done using the OIM Analysis™ software. The max peak count was varied between 7-12 during indexing of the various phases in order to better index the more complex structured Ni_2Al_3 against higher symmetry BCC phase. This data will be included in the Appendix.

3.4.4 Transmission Electron Microscopy (TEM)

A single sample was prepared for TEM characterization using the Hitachi NB5000 FIB. A protective layer ~15 x 3 was laid down using a gas nozzle. The bulk sample was cut at 40kV and final thinning was done at 20kV and 10kV.

TEM analysis was conducted on a FEI F2000X TALOS Scanning Transmission Electron Microscope (STEM). The TEM thin foil sample was cleaned of surface impurities prior to analysis using a FISCHIONE Model 1020 Plasma Cleaner.

3.4.5 X-ray Diffraction (XRD)

X-ray diffraction characterization (XRD) was used to identify the present phases within samples of interest. Continuous Θ-2Θ scans were performed on the PANalytical Xpert Diffractometer from nominally 5-60° 2Θ using MoKα radiation (λ=0.709319 Å) and the X'Celerator detector. Total detection times ranged from 45 – 70 minutes using 2 or 4 total scans. It was found that when CuKα radiation (λ=1.541838 Å) was used, incident CuKβ radiation caused fluorescence in the nickel within the samples and

resulted in high background intensity levels. As fluorescence is the result of a absorption re-emission phenomena, the depth of the diffraction signal would be very small and thus not indicative of the bulk sample. Thus, MoKα radiation was used for all XRD characterization thereafter in order to measure a signal representative of the bulk sample. A search match was conducted for each data set using the "Jade" software and the ICDD database [74], [75]. XRD characterization was performed on the infiltrated TiC preforms as well as remaining phase mixture in the crucible and also nickel aluminide melts.

3.5 X-ray Computed Tomography (XCT)

X-ray tomography (XRT) characterization was performed on the printed TiC preforms in order to view the network structure of the TiC particles in the as-printed state. An X-ray Computed Tomography (XCT) scan was performed using a Zeiss Xradia Versa XCT instrument. A 140 kV accelerating voltage at 9W of powder was used for the measurements. The sample was rotated along the vertical axis for 360 degrees; collecting images ~1600 times at equal rotational intervals. A 0.4x wide field of view (FOV) scintillator objective was used, attached to a CCD camera; capturing a 21 mm diameter FOV. A 1x1 camera binning was used, yielding a pixel size of 11.183 microns.

3.6 High Temperature Differential Scanning Calorimetry (DSC)

Differential scanning calorimetry (DSC) was performed on the nickel aluminide powders ($NiAl_3$ and Ni_3Al) in order to characterize the melting and solidification behavior of the alloys. A Netzch Differential Scanning Calorimeter (DSC), Model Pegasus 404, was used for the melting study. Two alumina crucibles were used: one as a reference (empty pan) and the other as a sample pan. Before each test the chamber was evacuated and back filled with ultra-high purity argon three times. The argon gas went through a guttering unit with a oxygen monitoring sensor. The measurement was performed under Ar purge gas with oxygen level < 10^{-7} ppm. The heating and cooling rate was 10°C/min. For the $NiAl_3$ alloy, three cycles were tested as follows:

1. 25°C -> 1250°C -> 400°C
2. 400°C -> 1250°C -> 400°C
3. 400°C -> 1250°C -> 25°C

For the Ni_3Al alloy, three cycles used were:

1. 25°C -> 1500°C -> 1200°C
2. 1200°C -> 1500°C -> 1200°C
3. 1200°C -> 1500°C -> 25°C

Additionally, $NiAl_3$ powder was mixed with TiC powder in a 1:1 molar ratio and tested using the above $NiAl_3$ cycle, but instead the sample was heated to 1400°C and held for 30 minutes. The purpose of the second DSC cycle was to simulate TiC dissolution of liquid $NiAl_3$ at the local interface during infiltration processing and how that might affect solidification behavior of the alloy. Netzch analysis software was used for determination of melting and solidification peaks as well as pattern analysis and plotting.

4 Results & Discussion

The goals of the present work are two-fold. Firstly, the aim was to fabricate a fully dense cermet composed of a $NiAl_3$ or Ni_3Al matrix with a TiC reinforcement in a near-net-shape fashion by a combination process of binder jet AM and melt infiltration. Secondly, experiments were conducted with two intermetallics from the Ni-Al system to better understand the competing kinetics of infiltration and dissolution. The Al-rich $NiAl_3$ alloy in particular is present in the literature only very scarcely, and hence is not well studied or documented. As far is understood, this work will be the first documented instance of using $NiAl_3$ in a carbide-reinforced metal matrix composite. Results from these experiments will be presented in the following chapter alongside discussion on how to interpret these results and their implications.

4.1 XCT of Printed TiC Preform

In order to characterize the arrangement of TiC particles in the preform prior to infiltration, XCT was conducted on a preform from round 1 (~30% dense) and round 2 (~50% dense). The round 1 preform was sintered at 1500°C for 2 hours while the round 2 preform was not sintered. The motivation for this, as mentioned previously in Chapter 3, was that sintering resulted in very little to no densification of the TiC preform and therefore sintering was not conducted on TiC preforms after round 1.

A cross-sectional image of the XCT scan conducted on a round 1 preform is shown in Fig. 4-1, where TiC particles (grey) are visibly arranged in a dimensionally connected network structure. The average particle size of the TiC powder used in round 1 prints was ~2.5µm while the XCT scan resolution was ~10µm so the grey areas are likely representative of clusters of TiC particles. While the TiC preform showed very little to no densification after sintering it is certainly possible that the visible “necking” between TiC clusters is at least partially a product of neck growth during sintering, which does not necessarily result in shrinkage or densification. Ashby describes the solid state sintering process in six steps, where the initial “necking” is a surface transport mechanism and does not result in densification, which occurs as a result of bulk transport mechanisms [49], [76].

A cross-sectional image of the XCT scan conducted on a round 2 preform is shown in Fig. 4-2, where a network structure of TiC particles is considerably less visible. The print density of the preform is ~50% compared to the ~30% print density of round 1 preform and has not undergone a sintering step so a direct comparison may not be viable. While significantly less pronounced than round 1, a dimensionally connected network of TiC particles is still visible and indicates that the network structure of TiC is likely a result of the binder jet process but exaggerated by neck growth during sintering, as seen in Fig. 4-1. Within the XCT scan of the round 2

preform, bright spots can be seen scattered throughout the preform. In XCT, a bright spot is representative of a higher atomic number element due to the higher amount of X-rays that would be scattered by the larger atomic radius. Quantitative EDS point analysis of the bright spots reveals large amounts of W (tungsten) and possibly Fe (iron). While C (carbon) cannot be accurately measured by EDS it is likely the bright spots are WC (tungsten carbide) given the frequency by which WC is printed on the same ExOne printer used to fabricate the TiC preforms in this work and may be contamination.

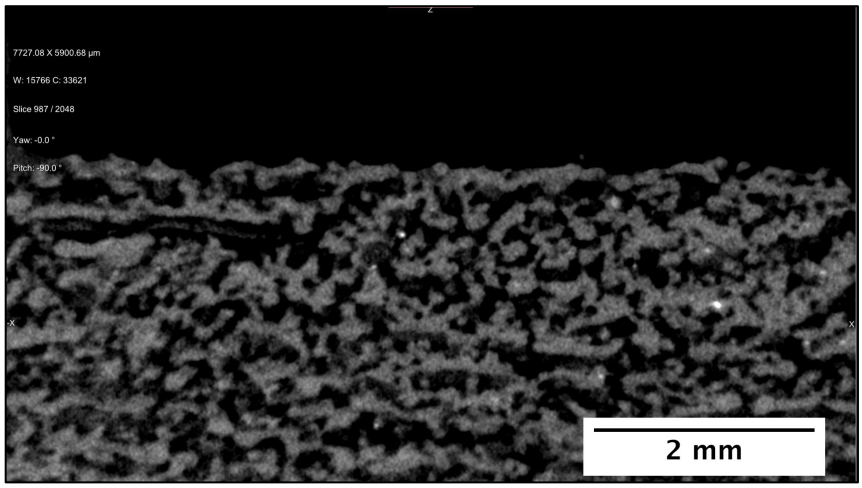


Figure 4-1 XCT of Preform 9 (~30% dense), sintered at 1400°C for 2 hours. Resolution is ~10um. Average particle size of TiC powder is ~2.5um

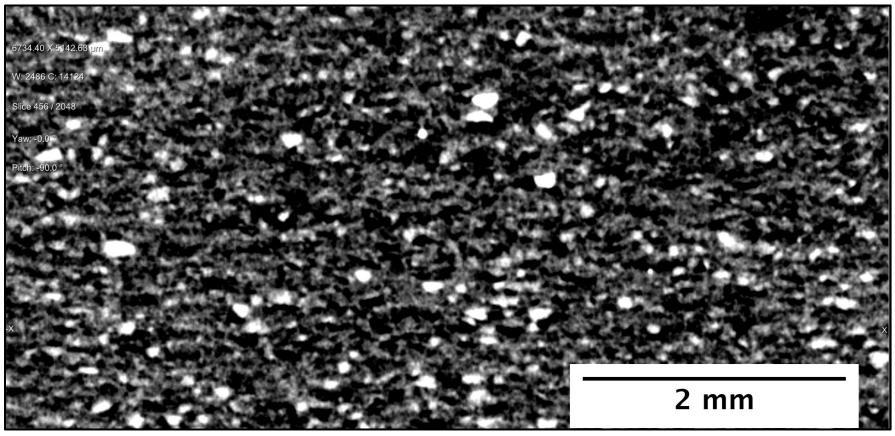


Figure 4-2 XCT of Preform S3 (~50% dense). Resolution is ~10um. Average particle size of TiC powder is ~30um. Bright spots are contamination of a singular or multiple higher Z elements

4.2 Ni_3Al – TiC infiltration

As mentioned previously, a majority of the previous research in literature on nickel aluminide cermets has utilized the Ni-rich Ni_3Al alloy as a matrix material. As such, this alloy provides a well-studied material from which to adapt the binder jet AM process for fabrication of nickel aluminide cermet materials. Initial infiltration experiments utilize base parameters, including temperature and time, described in literature with well-documented results as a "starting point" from which to conduct this work.

4.2.1 30 min Infiltration

Initially, a printed TiC preform (~30% dense) was infiltrated with Ni_3Al at 1430°C for 30 minutes in an alumina tube furnace under a reducing atmosphere of Ar/4% H_2. Nickel aluminides passivate by the formation of aluminum oxide and thus melting cannot be achieved under 100% Ar and requires a small amount of H_2 to reduce the oxide layer. The exact amount of $NiAl_3$ powder required to fill the entire void space of the preform was calculated.

In order to calculate the necessary amount of $NiAl_3$ required to fill the entire void porosity of the preform, volume fraction of the two respective phases (TiC and Ni_3Al) must converted to weight fraction. An arbitrary volume of 1 cc was assumed and also the density of Ni_3Al was assumed to be 7.35g/cc; within the range of reported density values of 7.25 – 7.5 g/cc. As the TiC preform is ~30% dense, the respective volume fractions of TiC and Ni_3Al are 0.3 and 0.7.

$$0.7\ cc * 7.35 g/cc = \ 5.145 g$$

$$0.3\ cc * 4.93 g/cc = 1.479 g$$

Total mass of 1 cc mixture of Ni_3Al (70 vol. %) and TiC (30 vol. %):

$$5.145 g + 1.479 g = 6.624 g$$

Calculate weight fraction of each respective phase:

$$\mathrm{Ni_3Al}: \ \frac{5.145}{6.624} = 0.7767 * 100 = 77.67\ wt.\%$$

$$\mathrm{TiC}: \ \frac{1.479}{6.624} = 0.2233 * 100 = 22.33\ wt.\%$$

Convert to parts per weight:

$$\frac{77.67}{22.33} = \frac{100}{x} \rightarrow x = 28.75$$

Calculate amount of Ni_3Al required to fill void space based upon TiC preform weight of ~2.4g:

$$\frac{100}{28.75} = \frac{x}{2.4} \rightarrow x = 8.34g \text{ of } Ni_3Al \text{ to fill preform}$$

Based upon a preform weight of ~2.4g, preform density of 30%, and Ni_3Al density of 7.35g/cc, ~8.3g of Ni_3Al is required to fully infiltrate the TiC preform. The necessary amount of Ni_3Al will change slightly based upon small variances in preform density (~30-32% dense) or assumed Ni_3Al density (~7.25 - 7.5g/cc). For the infiltration experiment, a TiC preform was set on a bed of ~9g of Ni_3Al powder such that ~8 wt. % excess Ni_3Al was provided for infiltration.

The infiltration results, shown in Fig. 4-3, show full volumetric infiltration of the preform by Ni_3Al but with very poor shape retention. The thin walls of the preform have partially collapsed and the bottom of the preform appears to have dissolved in the liquid metal to some extent, likely a result of TiC dissolution by liquid Ni_3Al, also noted by [30], [34], [36], [39], [40], [77]. Dissolution of the bottom of the preform was possibly amplified from the excess metal that would remain after full saturation of the preform by the liquid infiltrant or if the sample were to initially "sink" into the melt pool. Closer inspection reveals the presence of "ligaments" of metal on the outside of the preform. This same phenomenon is observed by Pan as "upward flowing traces" and indicates the driving force for Ni_3Al infiltration is very strong [33].



Figure 4-3 Sample 10 infiltrated with Ni_3Al at 1430°C for 30 mins. Visibly poor shape retention by wall collapse and excess metal fused to bottom of preform. "Upward flowing traces" of solidified metal clear along outside of preform indicating strong capillary driving force

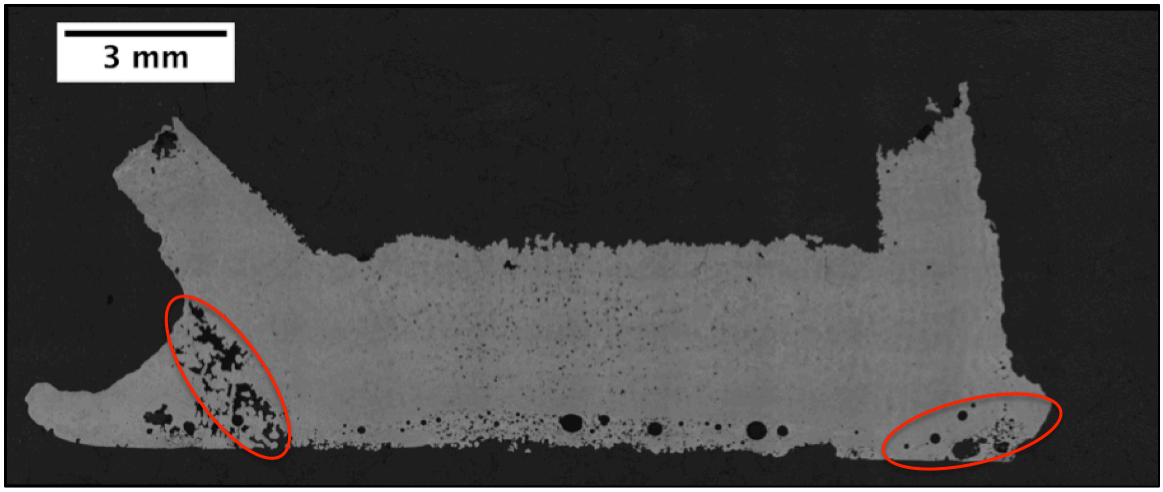


Figure 4-4 Optical stitching of Sample 10. Significant porosity visible in excess metal fused to bottom/side of preform

The density of the infiltrated preform, including metal fused to the outside, was measured to be ~95% theoretical density using the Archimedes displacement method. However, it can be seen in Fig. 4-4 that a significant amount of the porosity present in the part is limited to the pure Ni_3Al fused to the outside of the sample (circled in red) and not within the infiltrated preform itself, which appears to be near full density. Given the amount of excess metal fused to the outside of the preform, the displacement method provides only a rough estimate of the infiltrated density. The small amount of porosity that is present within the infiltrated preform appears to be limited near the center of the preform, indicating the time of infiltration was likely not enough to allow the liquid infiltrant to completely penetrate the preform. The reason for this porosity at the center was not made clear until after infiltration at 15 mins was conducted, which will be described in the next section. Despite the small quantity of porosity still present in the preform, the extent of metal fused to the outside of the preform indicates the use of excess Ni_3Al is likely unnecessary for achieving a fully infiltrated preform.

4.2.2 15 min Infiltration

As discussed in the previous section, full infiltration of the TiC preform was seen to occur after 30 minutes with the exception of micro porosity near the center of the preform, but potential dissolution of the TiC preform by liquid Ni_3Al is significant enough to compromise the structural integrity of the preform and lead to poor shape retention. In order to address this, an attempt was made to improve the shape retention of the infiltrated preform by reducing the hold time at peak temperature from 30 minutes to 15 minutes. It was hypothesized that lowering the time at which

the solid TiC was exposed to liquid Ni_3Al would lessen dissolution of TiC and thus improve shape retention. Ideally, an infiltration set-up such as a drop method would be used to limit exposure of the TiC preform to liquid metal, where the preform would be submerged in the liquid alloy only once peak temperature had been reached. However, such a method would require a more complex infiltration set-up leading to increased costs and reduced scalability and thus not considered in this work.

Based on a preform (~30% dense) weight of ~2.4g and using the methodology shown in section 4.2.1, a TiC preform was set on a bed of ~8.4g of Ni_3Al powder, where ~8.3g of Ni_3Al powder was required to fill the void space such that 1-2 wt. % excess powder was provided. Based upon the previous results, it was thought that excess metal fused to the outside of the preform indicated the amount of excess metal provided could be reduced. As the goal of this experiment was to attempt to improve the shape retention of the infiltrated preform, in addition to lowering the peak hold time the amount of excess metal provided for infiltration was reduced.

The infiltration results, shown in Fig. 4-5, Ni_3Al has infiltrated the full height of the sample but did not fully infiltrate the sample volumetrically indicated by an area at the center of the preform where liquid has not penetrated. If the preform were to "sink" to some degree within the liquid metal then the center of the preform would now become the furthest distance that liquid must penetrate, remember the height of the sample is 10mm while the width and length are 15mm. Lack of available liquid is unlikely to be the cause of incomplete infiltration due to the presence of excess metal still present around the outside of the preform. Initially, the small porosity near the center of the preform after 30 minutes of infiltration (Sample 10) was not attributed to an incomplete infiltration process as a function of time and was only made clear upon the significant lack of infiltration near the center after 15 minutes in Sample 7.



Figure 4-5 Sample 7 infiltrated with Ni_3Al at 1430C for 15 mins (left). Preform set on bed of Ni_3Al powder. Cross-section shows un-infiltrated center area of preform (right). Excess metal fused to outside of preform retains shape of circular crucible

4.2.3 Ni_3Al Infiltrated Microstructure & Phase Analysis

4.2.3.1 Optical Microscopy & SEM Characterization

The microstructure of the Ni_3Al infiltrated preform (Sample 10) is shown in Fig. 4-6, and appears to largely consist of a uniform dispersion of TiC particles within the Ni_3Al matrix; similar to what would be seen in a traditional P/M prepared microstructure. It was shown previously in section 4.1 that the TiC particles in the preform are arranged in a dimensionally connected network structure, yet no network structure is seen after infiltration by $NiAl_3$, which indicates the loss of the network structure may be correlated to the shape retention of the preform after infiltration.

However, it might be expected that if the network structure were to completely disband then the as-printed preform shape would be much less discernable after infiltration, yet the preform shape is still largely intact. Lower magnification optical microscopy of Sample 10 (Fig. 4-7) reveals the presence of subtle clusters of TiC within the overall dispersion of TiC particles, indicating the network structure has at least partially remained intact after infiltration. Shown in Fig. 4-8, near the center of the preform, it can be seen that the small amount of porosity present within the infiltrated part is located within these TiC clusters. Because the liquid infiltrate was unable to fully penetrate the TiC clusters near the center of the preform, this implies that the center of the preform was the last area to be impregnated. This aligns with the results seen for Sample 7 where the center of the preform was not infiltrated after 15 minutes.

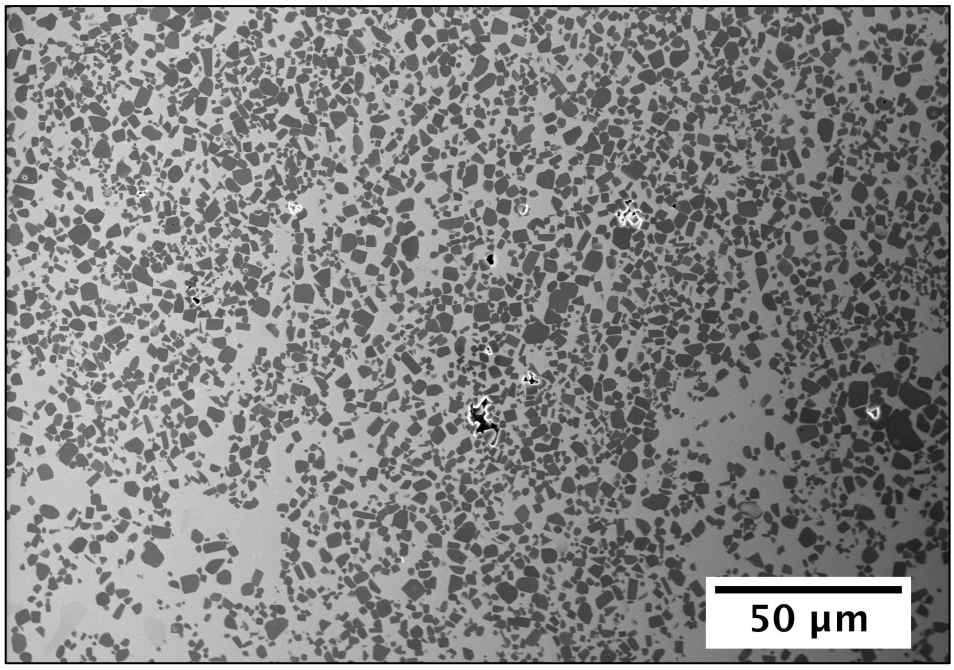


Figure 4-6 SEM image of Sample 10 infiltrated by Ni_3Al at 1430°C for 30 mins. 500x

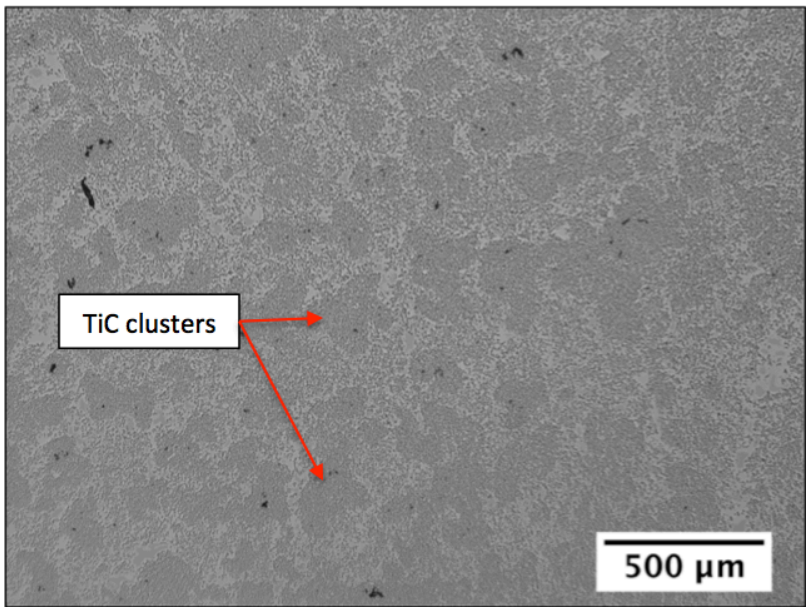


Figure 4-7 Optical micrograph of Sample 10 infiltrated by Ni_3Al at 1430°C for 30 mins. 5x. TiC clusters visible at lower magnifications noted by red arrows

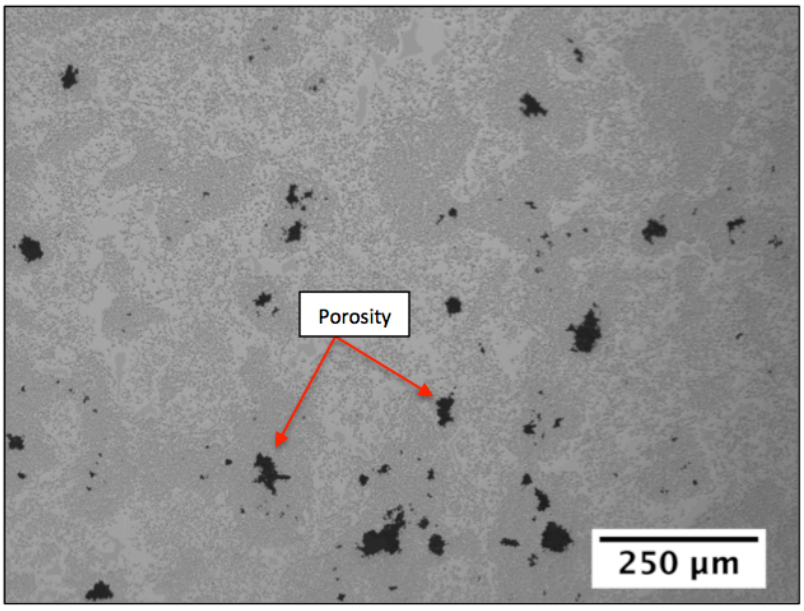


Figure 4-8 Optical micrograph of Sample 10, infiltrated by Ni_3Al at 1430°C for 30 mins. Porosity visible within TiC clusters near center of preform. 10x

This poses a unique challenge. Extending the infiltration time would likely allow the liquid infiltrant to fully penetrate the TiC clusters and remove porosity. However, while the small amount of porosity is reduced near the center of the preform, the thin walls of this geometry have already been fully infiltrated and would undergo further dissolution and shape loss. The near-net-shape capability of this geometry is much more reliant on the shape retention of the thin wall features compared to the cubic center. A potential solution to this problem would be to set metal powder within the cavity of the preform before infiltration to facilitate multiple infiltration fronts and ensure a fully impregnated preform in a lesser amount of time. While this might be an applicable solution for the specific geometry used within this work, it might not be useful for a more complex geometry such as a drill bit where there is no feature in which to set powder. Additionally, as discussed in Chapter 3, Pan demonstrated improved mechanical properties using a capillary only, single front infiltration method compared to a multi-front infiltration where infiltration is driven by both capillary action and gravity [33]. It is for these reasons that a multi-front infiltration method was not utilized in this work

4.2.3.2 Ni_3Al Infiltrated Phase Analysis

Initial inspection of the Ni_3Al infiltrated microstructure shows TiC particles dispersed in a single matrix of Ni_3Al. Upon closer inspection, there appears to be a second phase scattered within the Ni_3Al matrix, highlighted in Fig. 4-9. EDS mapping reveals the dark phase to be Al-rich compared to the base Ni_3Al matrix, shown in Fig. 4-10. The dark phase does not appear to be related to the presence of TiC as the same dark phase can be seen in the solidified Ni_3Al metal fused to the outside of the preform, shown in Fig. 4-11. EDS quantitative point analysis shows the dark phase to be ~63-65 at. % Al, which indicates possibly Ni_5Al_3 and/or NiAl B2 in small amounts.

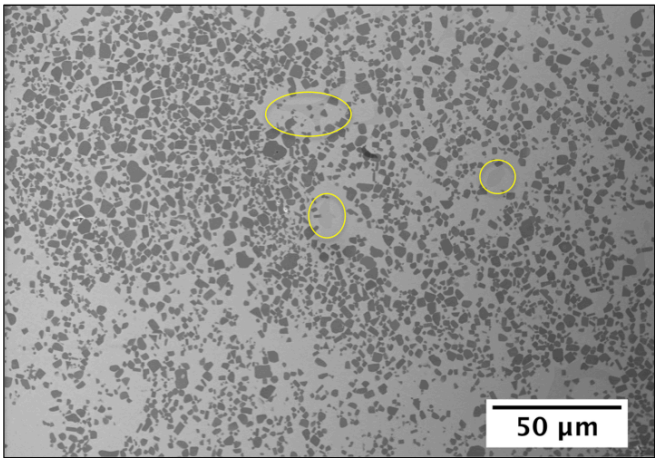


Figure 4-9 Sample 10 SEM image showing TiC particles dispersed in matrix with sporadic dark spots highlighted by yellow circles

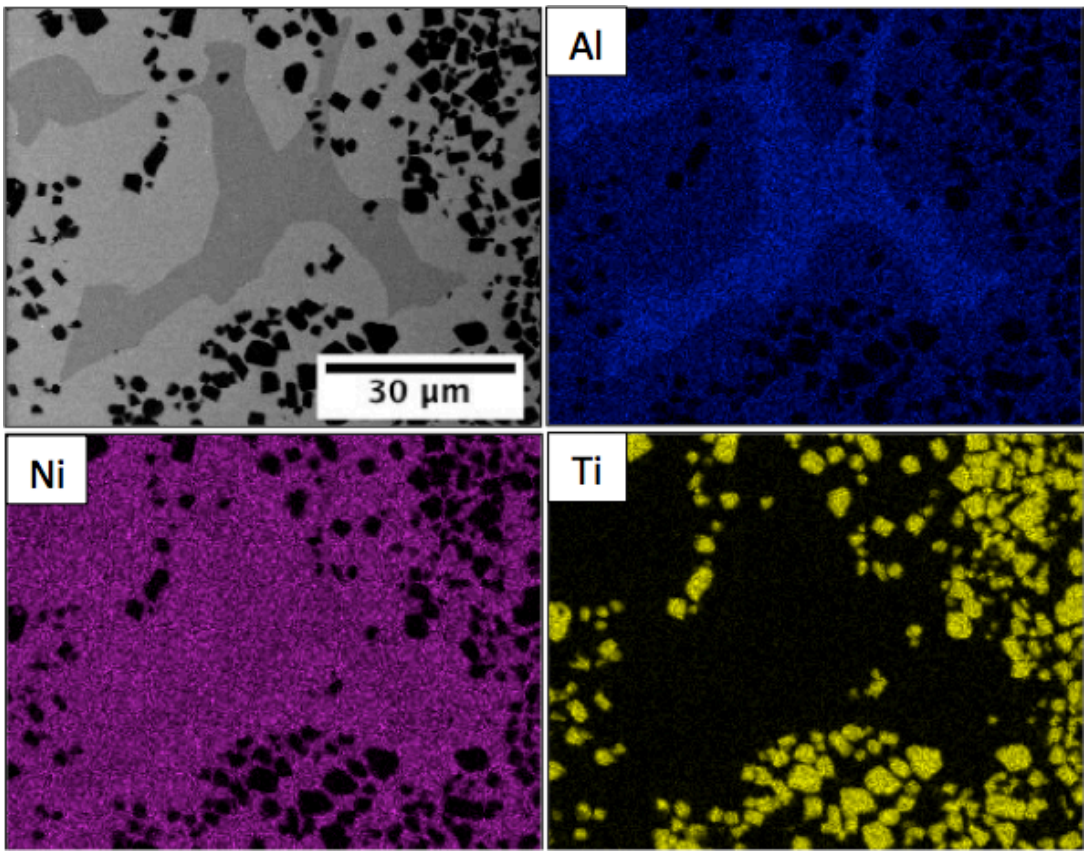


Figure 4-10 Sample 10 SEM image showing EDS map of dark spot indicating Al-rich compared to rest of matrix

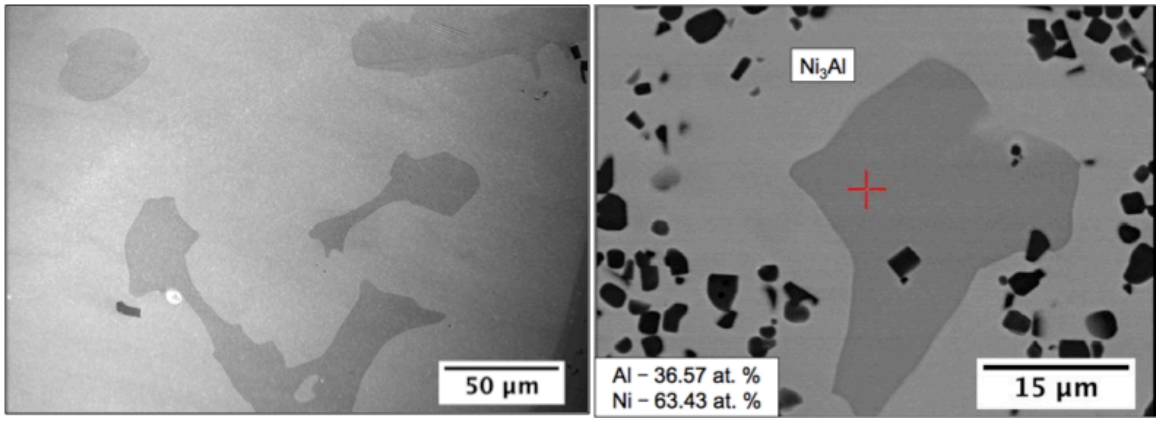


Figure 4-11 Sample 10, infiltrated at 1450C for 30 mins. a) Dark phase in base Ni_3Al metal fused to outside of infiltrated preform b) EDS point analysis of infiltrated preform shows composition of dark phase to be Al-rich compared to surrounding Ni_3Al matrix (light grey); black features are TiC particles

XRD data of the infiltrated preform (Fig. 4-12) confirms the presence of both TiC and Ni_3Al with no additional phases providing strong matches. The diffraction pattern was also checked against Ni_2Al_3 and NiAl as the next most Ni-rich phases within the Ni-Al binary system. Formation of NiAl within Ni_3Al-TiC cermet materials is documented in literature [78]. The presence of NiAl in small quantities may be possible, but is based only upon a single peak at 20.1° 2Θ. The pattern was not checked against Ni_5Al_3 as XRD data was taken before EDS quantitative point analysis but may be included in future work. Generally, the interaction volume with XRD lends itself towards a "bulk" specimen analysis method and as such if the dark phase were present only in small quantitates then it may be hard to confirm with XRD.

Clearly, there is a secondary phase solidifying in the metal matrix that appears to be Al-rich compared to the base Ni_3Al matrix. This indicates the Ni_3Al powder is non-stoichiometric, but may not be a complete surprise as the powder was shown to be pre-alloyed in Chapter 3. The melting and solidification behavior of the Ni_3Al infiltrate powder was characterized using high temperature DSC where the powder was heated 1500°C at 10°C/min and then cooled to 1200°C at 10°C/min before being cycled through twice more. A cooling curve is shown in Fig. 4-13, which shows two exothermic solidification peaks. The first exothermic peak appears at ~1380°C during the first cycle and is fairly small, but by the third cycle has shifted to ~1360°C and is much larger. The second exothermic peak at ~1345°C remains mostly constant through all three cycles and likely represents solidification of Ni_3Al, but does appear to be reducing in size with progressive cycles. According to the phase diagram in Fig. 2-1, Ni_3Al can exist within a range of compositions (~72.5-77.5 at. % Ni) and upon heating or cooling may pass through either a small phase field of NiAl B2 + Liquid or FCC Ni + Liquid. The presence of a second exothermic peak during solidification of the base Ni_3Al metal in conjunction with EDS and XRD phase analysis suggests that NiAl is likely forming during cooling of the Ni_3Al infiltrated preform. Then, according to the phase diagram, NiAl B2 may undergo solid-state decomposition to Ni_5Al_3, which would align with the composition of the dark phase indicated by EDS quantitative point analysis.

4.2.4 Infiltration Kinetics – Time of Infiltration

As discussed in Chapter 3, the Lucas-Washburn equation (Eq. 5 in Chapter 2) can be used to roughly describe the melt infiltration of a liquid into a porous preform. The infiltration distance, h, as a function of time, t, can be described where the pore radius is represented by r, liquid viscosity by η, contact angle by $cos\theta$, and liquid surface tension by γ_{LV}. Despite the limitations outlined in Chapter 3, Plucknett and Becher utilized the Washburn equation to estimate the time and height of Ni_3Al liquid infiltration into a porous TiC preform with the following assumed values. Based upon the surface tension values for Al and Ni (~1050 and 1780 mJ/m_2 respectively), γ_{LV} was estimated to be ~1600 mJ/m_2. Egry et. al reported a surface tension value of ~1450

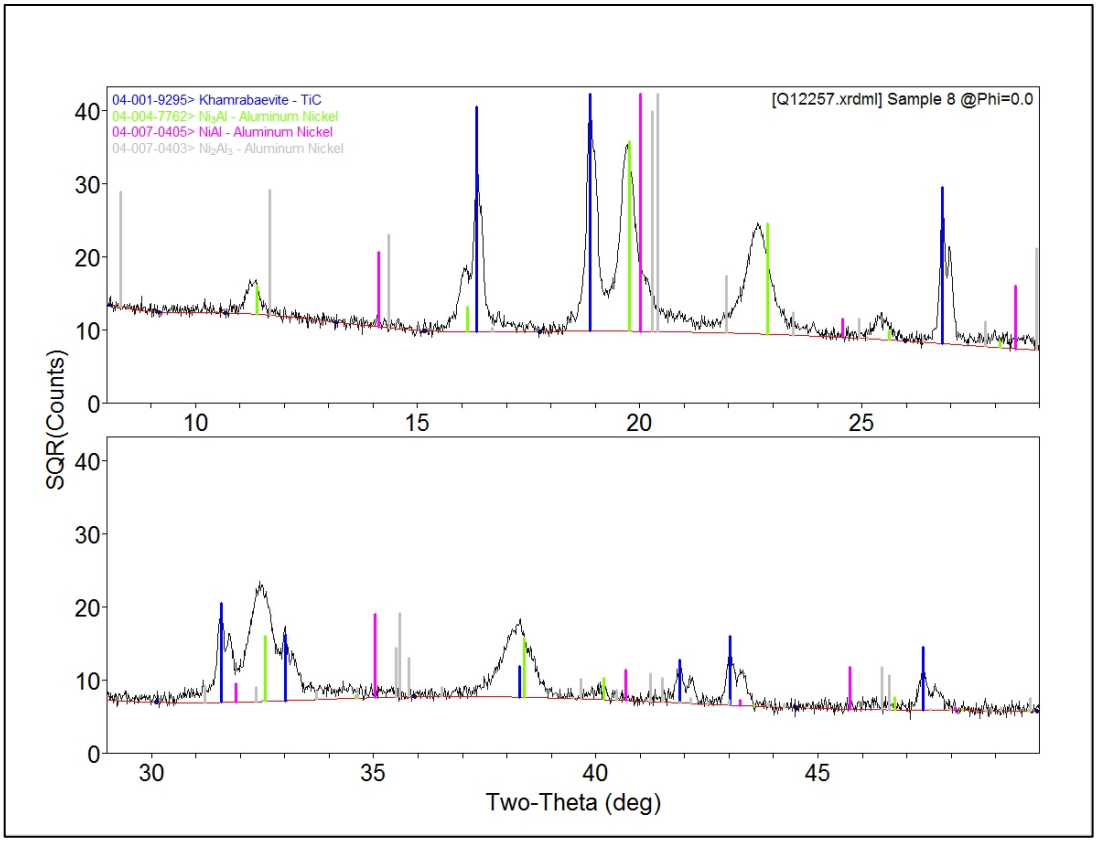


Figure 4-12 XRD pattern for Sample 10, infiltrated at 1430°C for 30 mins confirming presence of TiC and Ni_3Al phases and possibly NiAl. Pattern is miss labeled as Sample 8 but is in fact Sample 10. Mo radiation source was used to prevent fluorescence by nickel

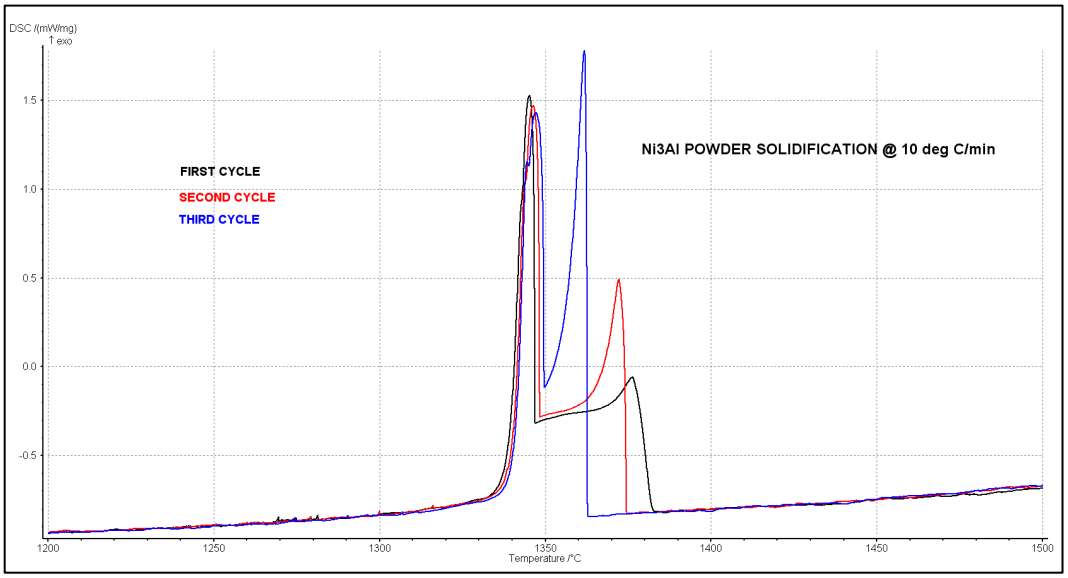


Figure 4-13 DSC Cooling curves of three separate Ni_3Al cycles. Two exothermic solidification peaks are observed. The first solidification peak is enlarged and moves towards lower temperatures with each progressive cycle

mJ/m^2 at 1400°C [79]. Melt viscosity was estimated to be 0.003-0.005 N-s/m^2 based upon the rule of mixtures for Ni_3Al. A mean pore radius was determined by Plucknett and Becher with porosimetry measurements to be ~0.23µm. Plucknett and Becher measured the contact angle at 1400°C to be θ = 25 - 35°. Using the assumed values put forth, a preform with a thickness of 15mm should be fully infiltrated in less than a minute according to the Lucas-Washburn equation. The average pore radius of the preform used in this work is unknown, but the pore size dependence on time of infiltration is shown in Fig. 4-14 and indicates that infiltration should occur in under a minute despite a larger pore radius.

However, Plucknett and Becher's extrapolated experimental data (Fig. 4-15) shows that it would take upwards of 30 minutes to fully infiltrate a 15mm thick preform. They explain that a slower infiltration rate than predicted would occur by chemical alteration of the Ni_3Al liquid metal by dissolution of TiC where liquid surface tension γ_{LV}, melt viscosity η, and contact angle θ would all likely be affected [34]. W

Within this work, it was shown that liquid Ni_3Al failed to fully infiltrate a TiC preform after 15 minutes, but full infiltration was observed after 30 minutes. Additionally, a slower infiltration rate was observed by Plucknett and Becher and described as the result of TiC dissolution by liquid Ni_3Al. Based upon the slowed infiltration rate observed in this work and also described by Plucknett and Becher, it is likely significant dissolution of TiC particles by liquid Ni_3Al is occurring, which is possibly leading to shape loss of the infiltrated preform.

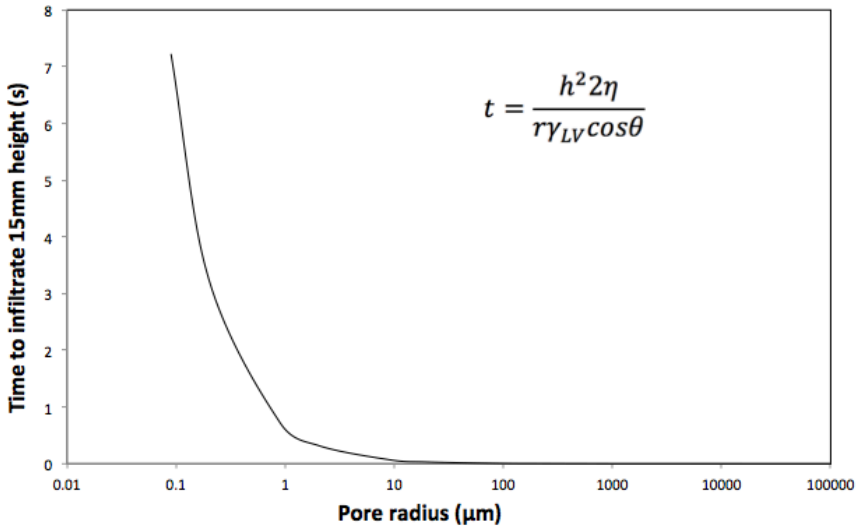


Figure 4-14 Time of infiltration as a function of pore radius using Lucas-Washburn equation. Assumed values include contact angle of 30°, melt viscosity (η) of 4 MPa-s, surface tension (γ_{LV}) of 1.6 J/m^2

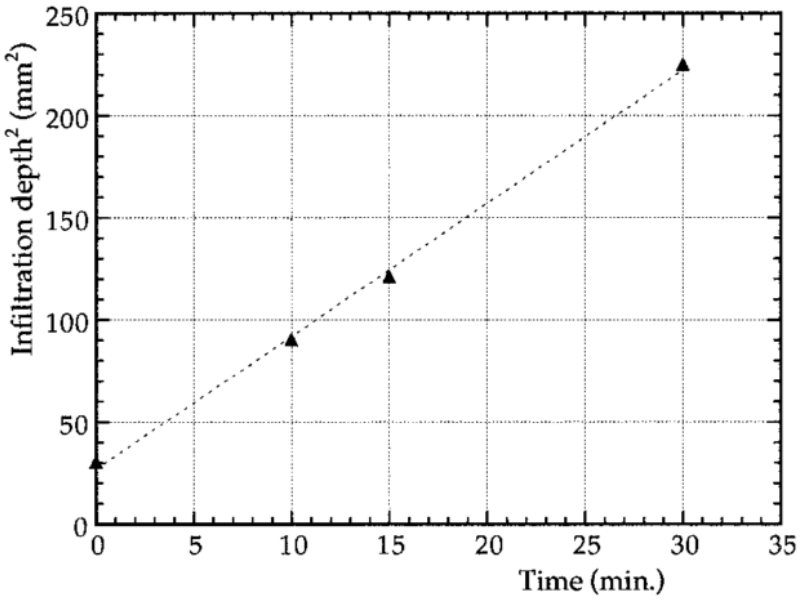


Figure 4-15 "Effect of time on infiltration depth for porous TiC preforms CIPed at 285 MPa (~63% of theoretical density)" [34]

4.3 $NiAl_3$ – TiC infiltration

In order to gain a better understanding on wetting behavior and the role it plays in shape retention, the more Al-rich $NiAl_3$ phase from the same Ni-Al binary system was also infiltrated into a printed TiC preform. As mentioned in Chapter 3, it is well known that transition metals (such as Ni) wet transition metal carbides (such as TiC) very well compared to metals such as Al. As such, it might be expected that a nickel aluminide with lesser nickel content would exhibit different wetting behavior. For this reason, the Ni-rich Ni_3Al and Al-rich $NiAl_3$ alloys were compared in this work.

$NiAl_3$ was infiltrated into a printed TiC preform (~30% dense) at 1415°C for 30 minutes in an alumina tube furnace under Ar/4% H_2 atmosphere. Compared to Ni_3Al infiltrated samples 7 and 10, which used a heating rate of 10°C/min, Sample 6 was infiltrated using a heating rate of 6.7°C/min due to the use of a different tube furnace as mentioned in Chapter 3. The necessary amount of $NiAl_3$ required to fill the void space of the preform is calculated using the methodology in section 4.2.1 and shown below.

$$0.7\ cc * 3.96 g/cc = 2.772 g$$

$$0.3\ cc * 4.93 g/cc = 1.479 g$$

Total mass of 1 cc mixture of $NiAl_3$ (70 vol. %) and TiC (30 vol. %):

$$2.772g + 1.479g = 4.251g$$

Calculate weight fraction of each respective phase:

$$\mathrm{NiAl_3} = \frac{2.772}{4.251} = 0.652 * 100 = 65.2\ wt.\%$$

$$\mathrm{TiC} = \frac{1.479}{4.251} = 0.348 * 100 = 34.8\ wt.\%$$

Convert to parts per weight:

$$\frac{65.2}{34.8} = \frac{100}{x} \rightarrow x = 53.37$$

Calculate amount of $NiAl_3$ required to fill void space based upon TiC preform weight of ~2.35g

$$\frac{100}{53.37} = \frac{x}{2.35} \rightarrow x = 4.4g \text{ of } \mathrm{NiAl_3} \text{ to fill preform}$$

Based on a preform weight of ~2.35g and $NiAl_3$ density of 3.96g/cc and using the methodology shown in section 4.2.1, ~4.4g of $NiAl_3$ powder is required to fully infiltrate the TiC preform. However, ~7.6g of $NiAl_3$ powder was provided for the infiltration process. The primary goal of this experiment was to ensure a fully infiltrated, fully dense cermet and to guarantee this an arbitrary amount of excess metal was used: ~70 wt. % excess $NiAl_3$ powder.

The infiltration results are shown in Fig. 4-16 & 4-17. It can be seen that the liquid metal fully infiltrates the volume of the preform while also exhibiting excellent shape retention. The printed outer dimensions of the cup were 15 x 15 x 10mm while the outer dimensions post-infiltration were measured to be 14.93 x 15.38 x 10.23-10.51mm, where the range in height results from a very slight warping to be apparent at the corners of the infiltrated preform. Each dimension is an average of 3 measurements. It can be noted that the total dimensional volume of the preform shows signs of swelling after infiltration by $NiAl_3$, with a linear shrinkage of <2% in a singular direction. However, significant porosity remains after infiltration and the cermet is measured to be ~88-90% theoretical density by the displacement method. Additionally, cracking behavior can be clearly observed within the material, particularly within the thin walls of the geometry.



Figure 4-16 Sample 6 infiltrated with $NiAl_3$ at 1415°C for 30mins. Preform shows excellent shape retention

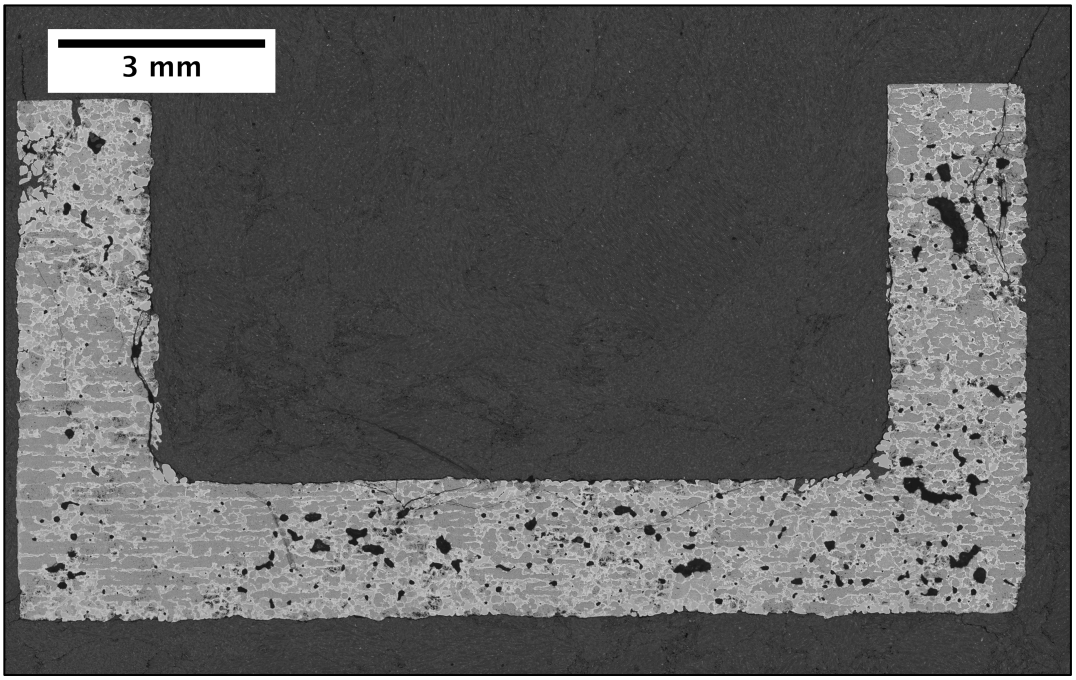


Figure 4-17 Optical stitching of Sample 6. Significant porosity visible throughout specimen. Visible cracking indicates brittle nature of alloy. Cross-section taken from center of preform where small warpage at corners is not discernable

4.4 Ni_3Al Infiltrated Microstructural & Phase Analysis

4.4.1 SEM

It was shown in previous sections that TiC particles are arranged in a dimensionally connected network structure in the preform prior to infiltration. Infiltration by Ni_3Al, which exhibited poor shape retention, resulted in dissolution of this network structure and showed a microstructure where TiC particles were largely uniformly dispersed in the matrix metal. Conversely, a TiC preform infiltrated by $NiAl_3$ resulted in excellent shape retention. The microstructure of a $NiAl_3$ infiltrated specimen is shown in Fig. 4-18. It can be seen that TiC particles are set in clusters that are dimensionally connected throughout the matrix, indicating the network structure in the green preform has largely remained intact after infiltration. A second feature that stands out are the small, light grey areas in the base metal matrix, which was more easily seen using a backscatter detector where higher atomic # elements will provide a brighter contrast. Therefore, a lighter color in the matrix indicates a likely more Ni-rich phase and will be discussed in the following sections. Large, bright spots with very high contrast can also be seen and is likely porosity within the microstructure as a result from carbide pullout during the polishing process. Closer inspection reveals small porosity present within the clusters of TiC as well, indicated by the black areas with a high contrast perimeter surrounding the TiC particles. The microstructure of the infiltrated preform will be discussed in-depth in later sections.

The excellent shape retention after $NiAl_3$ infiltration indicates that either dissolution of TiC by $NiAl_3$ is lesser compared to Ni_3Al, and thus does not dissolve TiC enough to remove the structural network, or $NiAl_3$ reacts with TiC at the local interface to form a reaction product that would then protect TiC particles from further dissolution. Such a reaction might also provide a displacement reaction that might explain the apparent swelling (or lack of shrinkage) in the $NiAl_3$ infiltrated preform. Unfortunately, there is no reported wetting angle of TiC by $NiAl_3$ in literature, but the reported wetting angles of Ni and Al on TiC can provide insight. As mentioned previously in Chapter 3, transition metals (such as Ni) wet the carbides of transition metals (such as TiC) very well, with a reported wetting angle as low as 25° for Ni on TiC [69]. The wetting of TiC by aluminum is more complex, as it is a reactive system and exhibits dynamic wetting behavior. It is well documented that aluminum experiences a non-wetting to wetting transition at elevated temperatures and will have a steadily decreasing contact angle over time by the formation of Al_4C_3 at the interface with a reported equilibrium contact angle as low as 25-40° [50], [57], [69]. Thus, it may be expected that a Ni-rich alloy (Ni_3Al) would exhibit better wetting behavior on TiC (and by extension stronger chemical interaction) compared to an Al-rich alloy ($NiAl_3$). Conversely, this also indicates the potential for a dynamic wetting behavior of TiC by $NiAl_3$

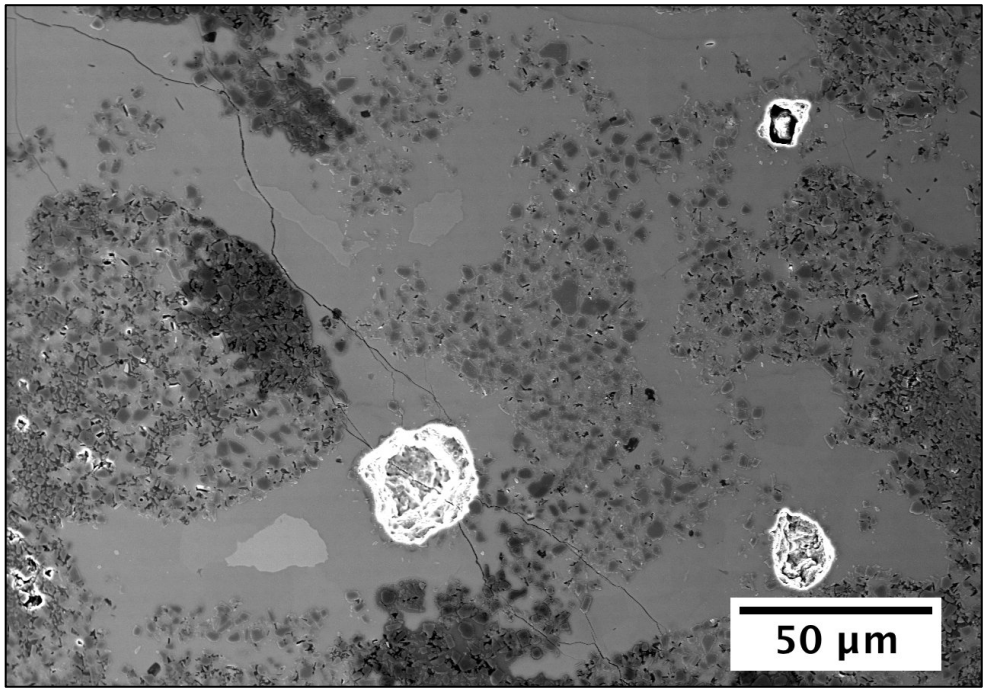


Figure 4-18 SEM (BSE) image of Sample 6 infiltrated by $NiAl_3$ at 1415°C for 30 mins. 500x. Light grey matrix phase is a higher atomic # phase, which is Ni_2Al_3, and will appear brighter. Cracking visible

4.4.2 Initial XRD Phase Analysis

XRD of sample 6, shown in Fig. 4-19, confirms the presence of $NiAl_3$ and TiC by strong peak match. Additionally, the Ni-rich Ni_2Al_3 phase was also detected and is possibly to be expected based upon the melting and solidification behavior of $NiAl_3$ as predicted by the Ni-Al phase diagram. This will be discussed in later sections. The crystal structures of Ni_2Al_3 and NiAl are very similar, such that the peak positions of the cross-referenced NiAl pattern are offset from Ni_2Al_3 peaks by ~1° 2Θ. Hence, the pattern was checked against NiAl but was found to be less likely than Ni_2Al_3. The close peak match requires that a more in-depth analysis of the pattern be conducted in the future, such as looking at d-spacing to verify the presence or absence of NiAl B2. It should be noted that a Mo x-ray source was used to prevent the fluorescence of Ni, but the smaller wavelength of a Mo x-ray source compared to a Cu source can result in a lower resolution at lower 2θ.

4.5 $NiAl_3$ Melting/Solidification Behavior

In the case of Ni_3Al infiltration, calculating the amount of material required to fill the entire void space of the preform is straightforward due to the single-phase nature of Ni_3Al during melting and solidification. The entirety of the metal material set in the

crucible either infiltrates the preform or is fused to the outside of the preform. However, in the case of $NiAl_3$, remnant material is left in the crucible after infiltration, shown in Fig. 4-20 as a dark, porous compact. The presence of remnant material in addition to a low infiltrated density (~88-90% theoretical density) indicates that only partial infiltration of $NiAl_3$ is occurring despite using a significant amount of excess material provided; ~68 wt. % excess. Certainly, the use of excess material before infiltration would likely result in remnant material being left in the crucible. However, as can be seen from previous results, the infiltrated preform does not achieve full density despite the excess material provided. Additionally, the excess material provided for Ni_3Al infiltration simply fused to the outside of the preform and was not left in the crucible. In the case of $NiAl_3$ infiltration, the preform was sitting directly on top of the remnant material and did not appear to have any direct interaction with the solidified material.

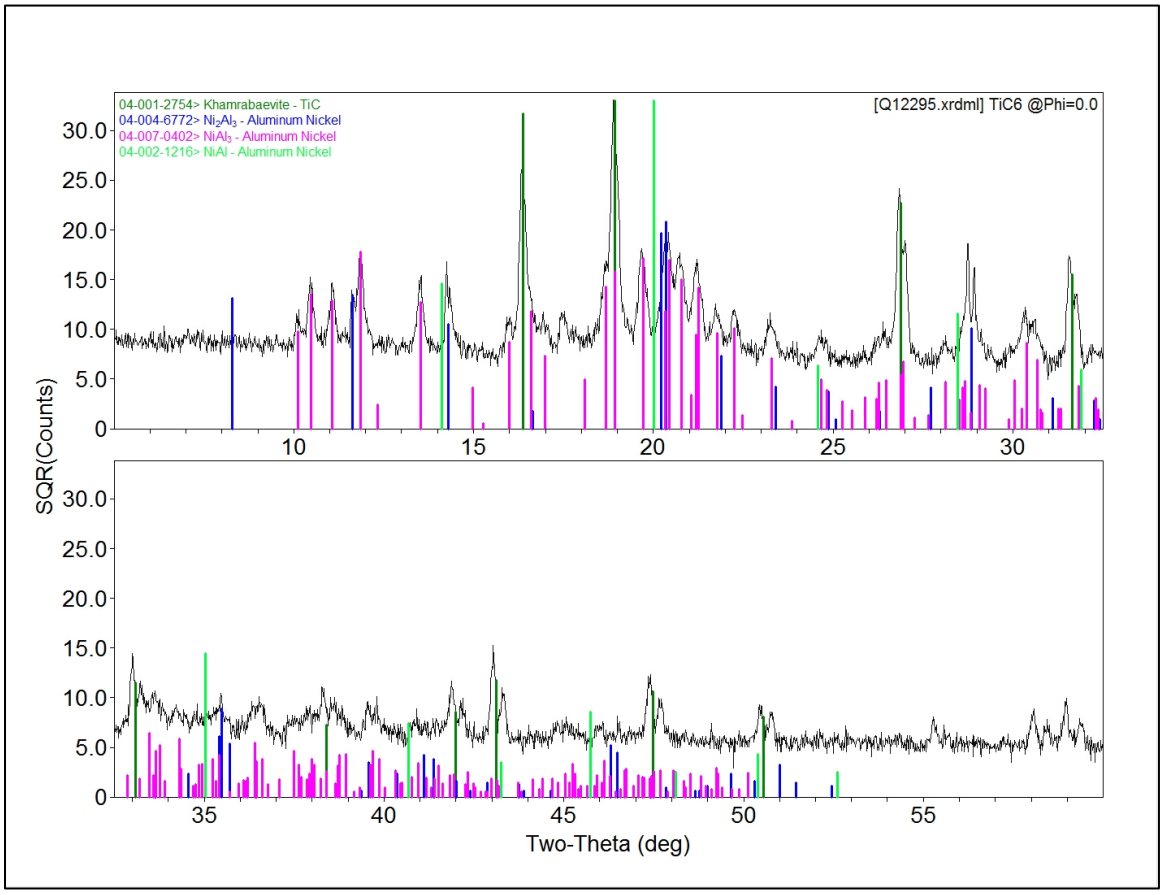


Figure 4-19 XRD pattern for Sample 6, infiltrated with $NiAl_3$ at 1415°C for 30 mins. Presence of TiC, $NiAl_3$, Ni_2Al_3 confirmed. Pattern also checked against NiAl but no peak match



Figure 4-20 Remnant material left in crucible after $NiAl_3$ infiltration into TiC preform. Precipitate of some metal phase on crucible wall

4.5.1 $NiAl_3$ Infiltration of TiC preform – No Excess Infiltrant

In order to de-couple the remnant crucible material after infiltration from the excess $NiAl_3$ powder provided prior to infiltration, a printed TiC preform (Sample 9, ~30% dense) was infiltrated with the exact amount of $NiAl_3$ required to fill the void space of the preform provided. Based upon a preform weight and density of ~2.4g, ~4.1g of $NiAl_3$ powder was provided with no excess material. Infiltration was conducted with same parameters as previous $NiAl_3$ infiltrations - 1415°C for 30 minutes in an alumina tube furnace under an Ar/4% H_2 atmosphere with a heating rate of 6.67°C/min.

The infiltration results are shown in Figs 4-21 & 4-22. $NiAl_3$ appears to have fully infiltrated the full volume of the preform, but with significant porosity present throughout the preform and particularly concentrated near the center of the preform. The infiltrated density of Sample 9 was measured by the displacement method to be ~86-88% theoretical density. Despite the use of the exact amount of $NiAl_3$ powder required to fill the entire void space of the preform, there is still leftover material remaining in the crucible despite the preform having a low % theoretical density. The top surface of the remnant material has a very rough surface and appears to be a single, dark grey phase. However, the bottom of the leftover material has partially conformed to the shape of the alumina crucible indicating melting of the material. The flat bottom surface appears to have a silver, metallic looking phase possibly dispersed throughout the material. The remnant material is very fragile and will easily lose material with light physical contact. These results indicate that the leftover material is not simply a result of having excess infiltrant powder and is likely a result of a more complex melting behavior of $NiAl_3$.



Figure 4-21 Sample 9 infiltrated with NiAl3 at 1415°C for 30 mins. The infiltrated preform is shown on the left. The top surface of the remnant material is shown in the middle while the bottom surface of the remnant material is shown on the right.

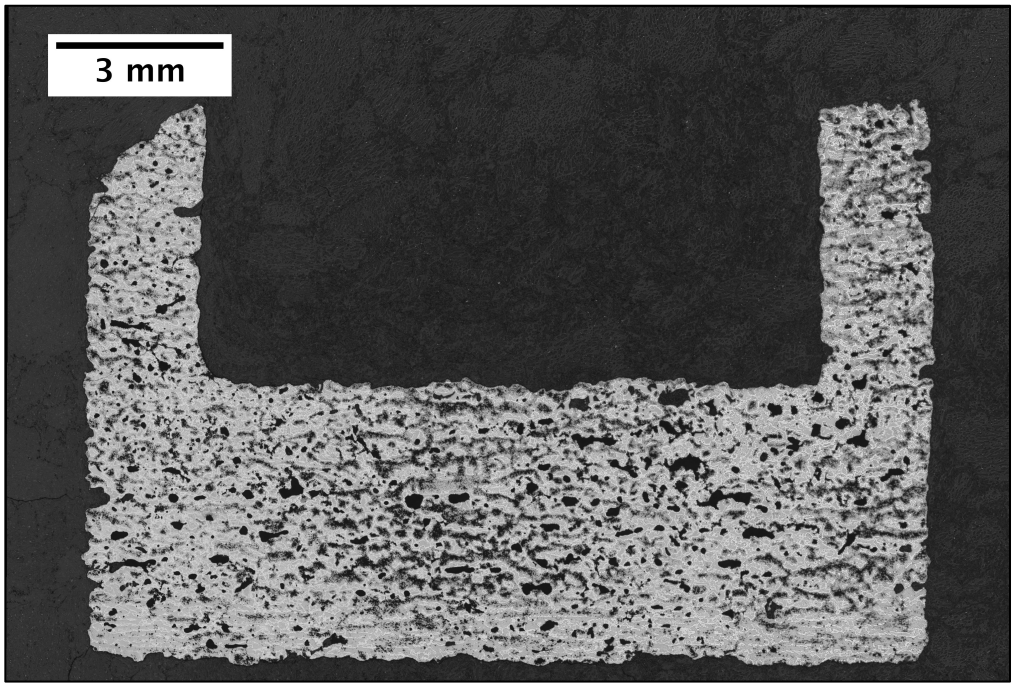


Figure 4-22 Sample 9 infiltrated with $NiAl_3$ at 1415°C for 30 mins. Considerable porosity visible throughout infiltrated preform.

4.5.1.1 XRD Phase Analysis of Remnant Material

XRD was performed on the Sample 9 remnant material left after infiltration and the results are shown in Fig. 4-23 & 4-24. Due to the rough, uneven geometry of the top surface of the remnant, two scans were performed on the bottom, flat surface of the material. First, the pattern was checked against $NiAl_3$ and Ni_2Al_3 and found to have

good peak match. The dotted lines at ~17.5° and ~25° 2Θ indicate the possibility of a unidentified phase. The pattern was then checked against Al and was found to have select peak matches, specifically at the previously unidentified phase at ~17° 2Θ, but remains highly speculative due to the lack of an overall fit. TiC was also checked due to the interaction of the $NiAl_3$ infiltrant with the TiC preform but was found to have very low peak match and unlikely to be present.

4.5.2 Melting & Solidification of base $NiAl_3$ Alloy

In order to investigate the melting behavior of $NiAl_3$ further, $NiAl_3$ powder was melted separately without a TiC preform. The result is shown in Fig. 4-25 and shows a highly segregated; two phase mixture where the same dark, porous phase is present and also a new silver, metallic phase that was not originally present after infiltration. Qualitatively, the color of the metallic phase very closely matches the color of the infiltrated TiC preform and is possibly the liquid infiltrant.

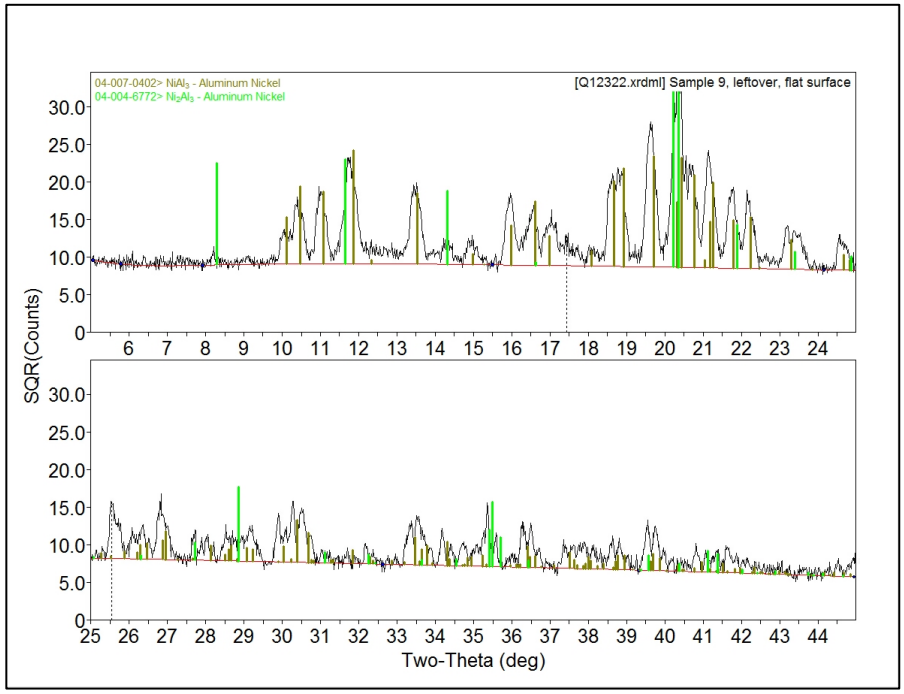


Figure 4-23 Diffraction pattern for flat, bottom surface of Sample 9 remnant, shown left in Fig. 4-19. $NiAl_3$ and Ni_2Al_3 phases identified. Dotted lines at ~17.5° and ~25° 2Θ indicate an unidentified phase.

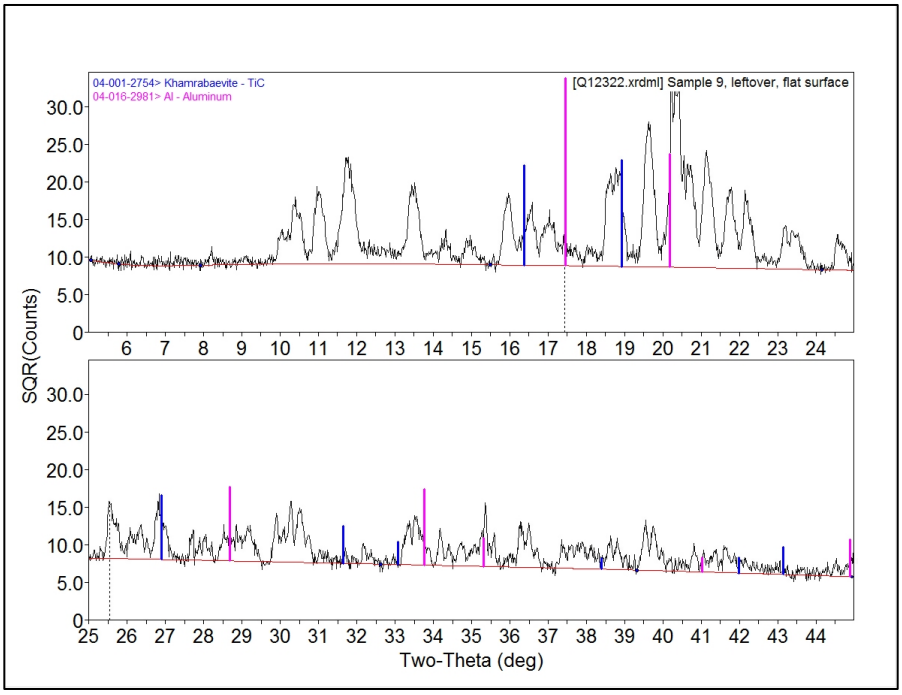


Figure 4-24 Same diffraction pattern of flat, bottom surface of Sample 9 remnant, shown left in Fig. 18. Al-rich phase matches one of the unidentified peaks at ~25°C 2Θ, but the presence of Al-rich phase and TiC are both highly speculative. Unidentified peaks shown here are $NiAl_3$ and Ni_2Al_3 peaks shown in Fig 4-23

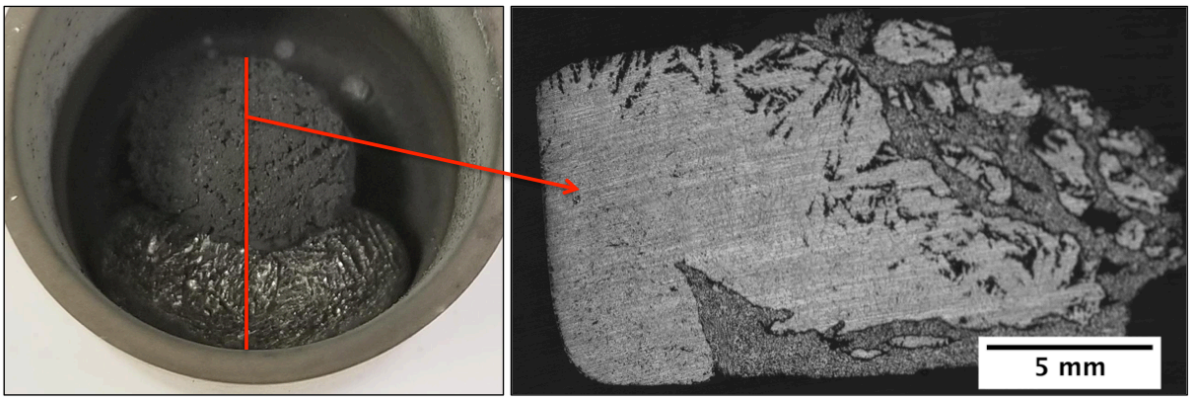


Figure 4-25 Remnant material left in crucible after melting pure NiAl3 powder (left). Cross-section of segregated remnant material (right)

4.5.2.1 Microstructure & Phase Analysis – SEM & EDS

Closer examination of the silver, metallic phase by SEM reveals a microstructure consisting of three distinct phases. Quantitative EDS was performed on each phase (Fig. 4-27) and shows the light grey area to very closely match Ni_2Al_3 and the grey region to be the bulk composition of $NiAl_3$. The black regions are measured to be ~99 at. % Al and have an aerial density of ~23-27%. Conversely, the dark macro phase appears to have the same phases present but is porous and was very difficult to measure microstructural composition.

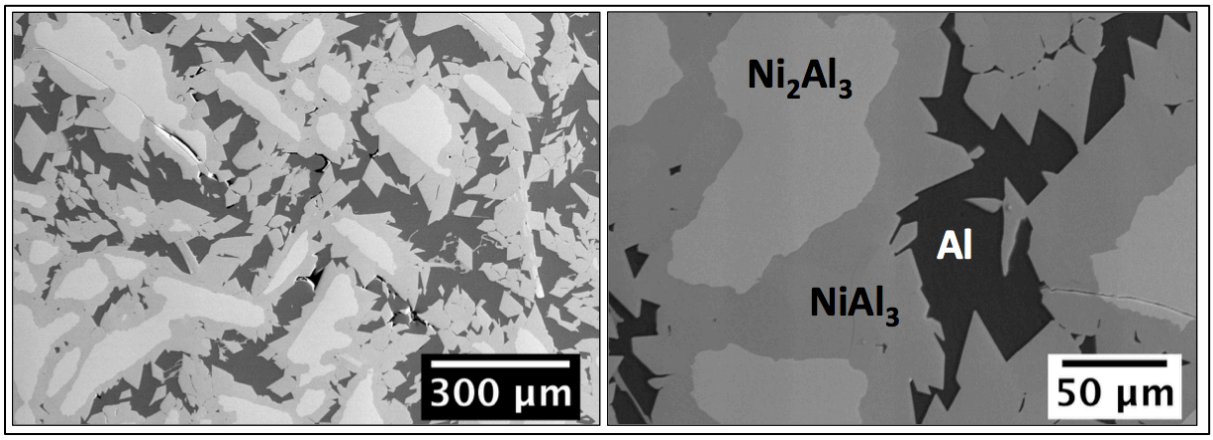


Figure 4-26 Microstructure of metallic, silver liquid phase showing three distinct phases: Ni_2Al_3 (light grey), $NiAl_3$ (grey), and Al (dark grey). Left and right images taken at 100x and 450x respectively

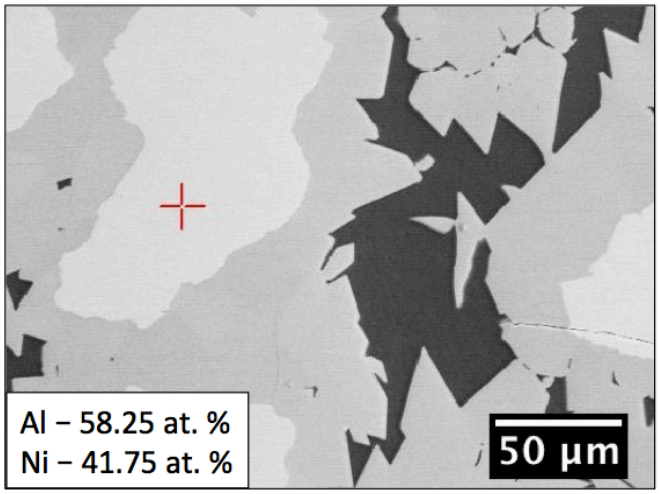


Figure 4-27 EDS Quantitative Point Scan Image a) Ni_2Al_3 b) $NiAl_3$ c) FCC Al. Image taken at 450x

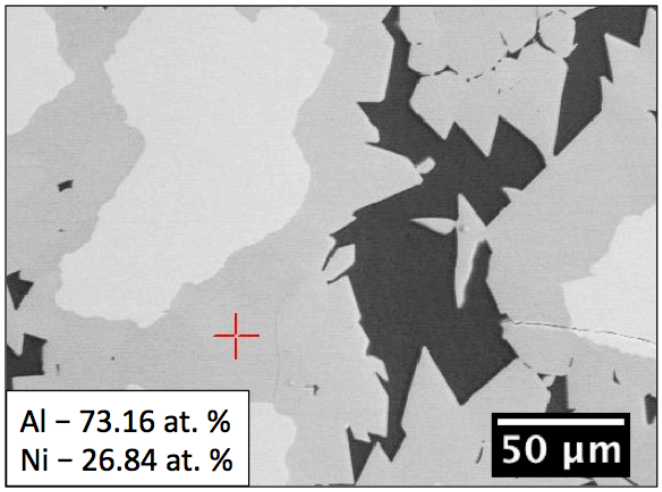


Figure 4-27. Continued 1. b) $NiAl_3$

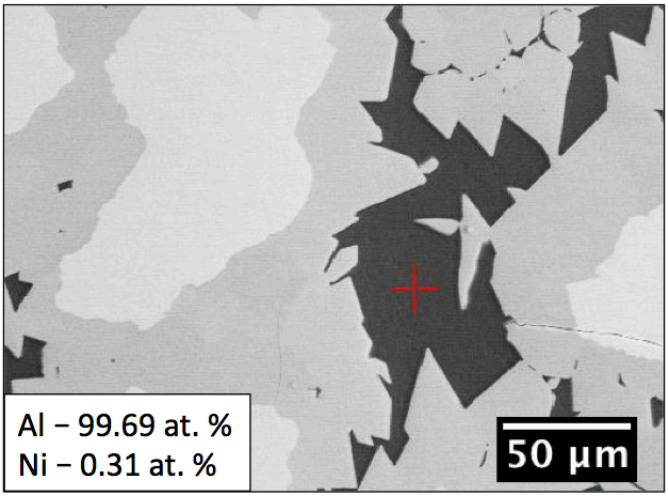


Figure 4-27. Continued 2. c) FCC Al

4.5.2.2 XRD Phase Analysis of Segregated $NiAl_3$ Solidification

XRD was conducted on each phase of the segregated remnant material to confirm the EDS phase analysis results. The entire nodule of material was used where two separate scans were utilized to attempt to isolate the diffraction signal (XRD) from each phase as much as possible. A scan of the gray, porous phase is shown in Fig. 4-28 and confirms the presence of $NiAl_3$, Ni_2Al_3, and a possible Al-rich phase. The pattern was also checked against TiC, whose peaks are speculative and unlikely, which is expected, as there was no TiC preform present during the melting experiment. It is thought that a small portion of the diffraction signal originated from the silver, metallic phase. During the scan of the metallic phase, the dark grey phase was covered by a zero background half plate, which precluded a diffraction signal originating from it. However, this was not used to cover the metallic phase during the scan of the dark grey phase. A scan of the silver, metallic phase is shown in Fig. 4-29 and confirms the presence of $NiAl_3$, Ni_2Al_3, and an Al-rich alloy. Two peaks of the pattern indicate aluminum nitride (AIN), but this is unlikely as the melting atmosphere was Ar/4% H_2.

4.5.2.3 Melting & Solidification Behavior – DSC

The solidification behavior of $NiAl_3$ can be explained by looking at the Ni-Al phase diagram (Fig. 4-30). The bulk composition of $NiAl_3$ is set at 25 at. % Ni and is represented by the red line. As $NiAl_3$ is heated it will decompose to a mixture of solid Ni_2Al_3 + Al-rich liquid at ~820°C. With further heating, the amount of Al-rich liquid increases while being saturated in Ni. This will continue until ~1150°C, at which point the alloy becomes completely liquid with the bulk $NiAl_3$ composition. Upon cooling, Ni_2Al_3 will begin to nucleate and solidify, and then $NiAl_3$, and finally the Al-rich liquid will reach the eutectic point at ~620°C (~0.03 at. % Ni) and FCC Al will nucleate alongside $NiAl_3$ in a possible eutectic structure. At the eutectic point the structure is almost all Al with very little NiAl3 within that phase field

The melting and solidification behavior of $NiAl_3$ is confirmed by high temperature DSC, shown in Fig 4-31 & 4-32. A small endothermic peak is observed at ~620°C where the Al-rich liquid begins to form and thus indicative of a non-stoichiometric alloy and possible presence of small amounts of Al. At ~850°C a large endothermic peak is observed and represents the primary decomposition of $NiAl_3$ into a mixture of Ni_2Al and Al-rich liquid. Finally, the alloy reaches the fully liquid point at ~1130°C represented by a third, small endothermic peak. As the alloy cools, solidification of Ni_2Al_3 begins indicated by the first, small exothermic peak at ~1100°C. With further cooling, a large amount of the Al-rich liquid begins to solidify as $NiAl_3$ at ~815°C and will then become completely solidified with the formation of FCC Al at ~630°C.

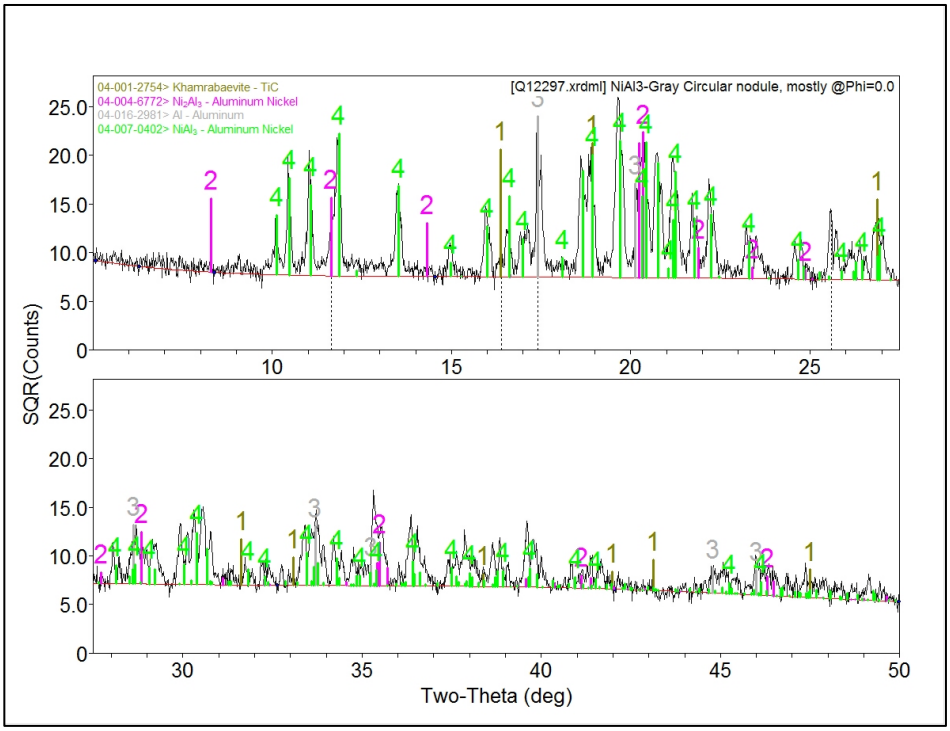


Figure 4-28 XRD scan of gray, porous phase of segregated remnant material. NiAl3, Ni2Al3, and possible Al-rich phase detected. It's thought that a small part of the diffraction signal originated from the silver, metallic phase

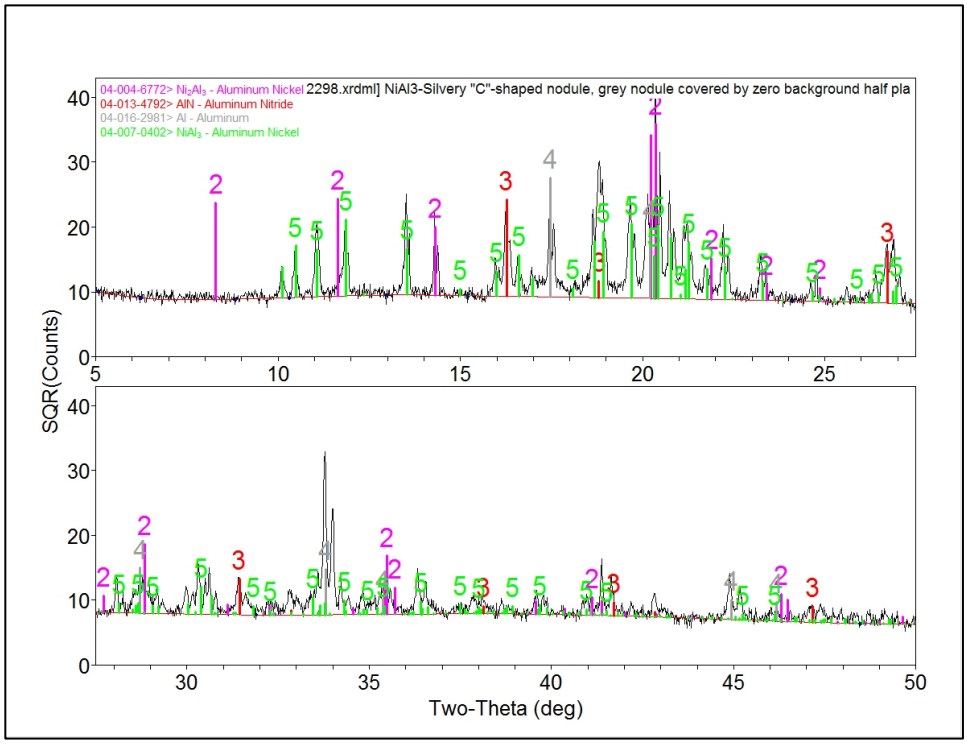


Figure 4-29 XRD scan of silver, metallic phase of segregated remnant material. NiAl3, Ni2Al3, and Al-rich alloy confirmed

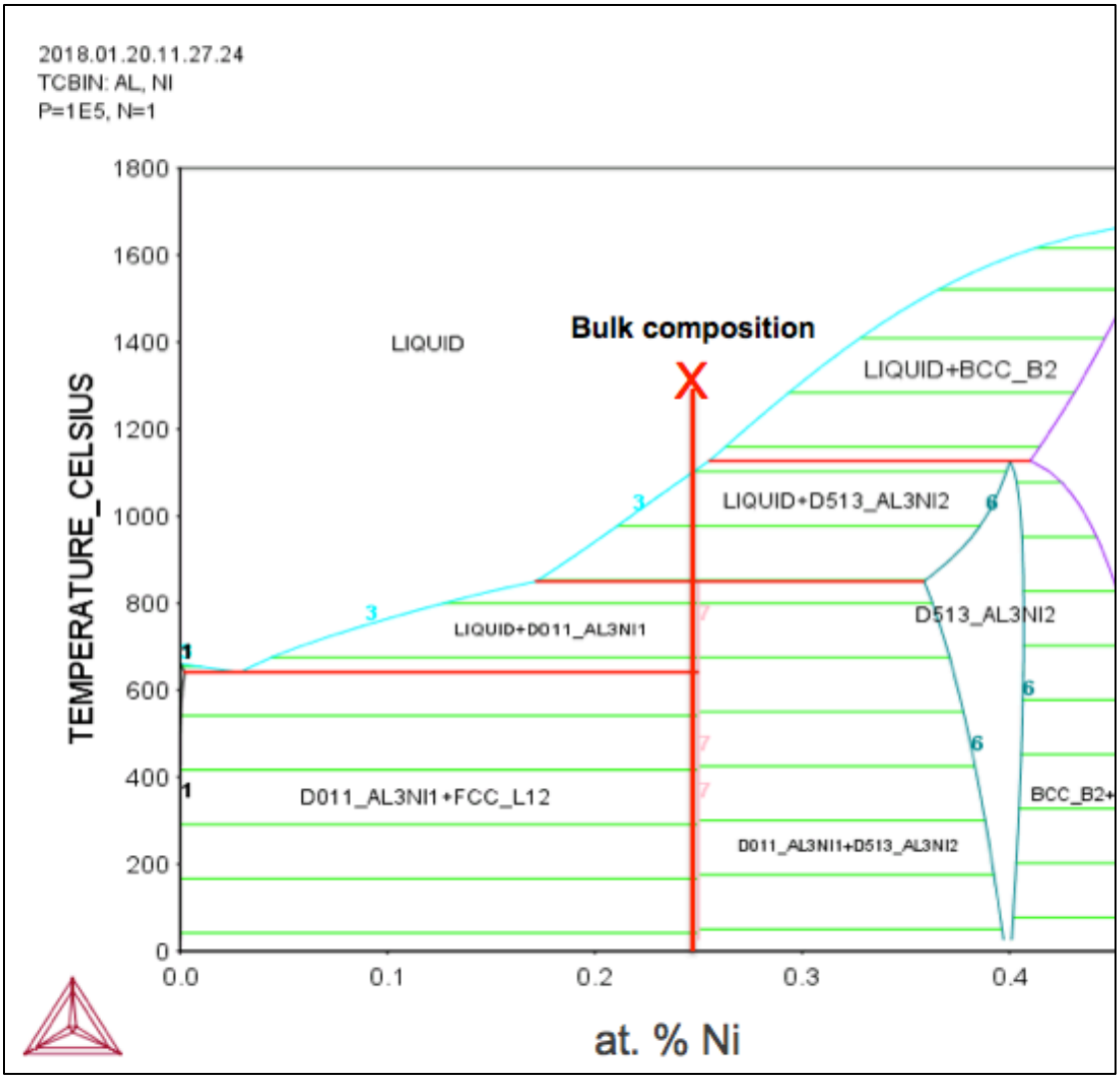


Figure 4-30 Ni-Al phase diagram created using ThermoCalc showing bulk composition of $NiAl_3$

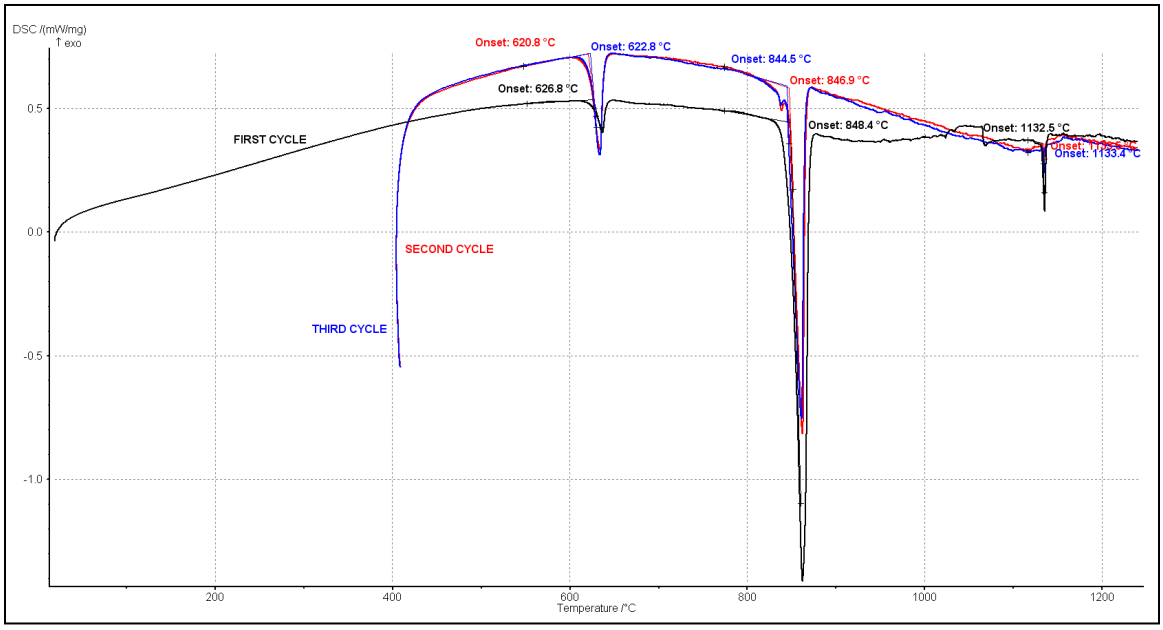


Figure 4-31 DSC Melting curves of $NiAl_3$. Black curve is first run from powder, blue and red curves are subsequent re-melting. Primary melting peak observed at ~850°C with smaller melting peaks observed at ~620°C and ~1130°C. Pattern made in Netzch analysis software

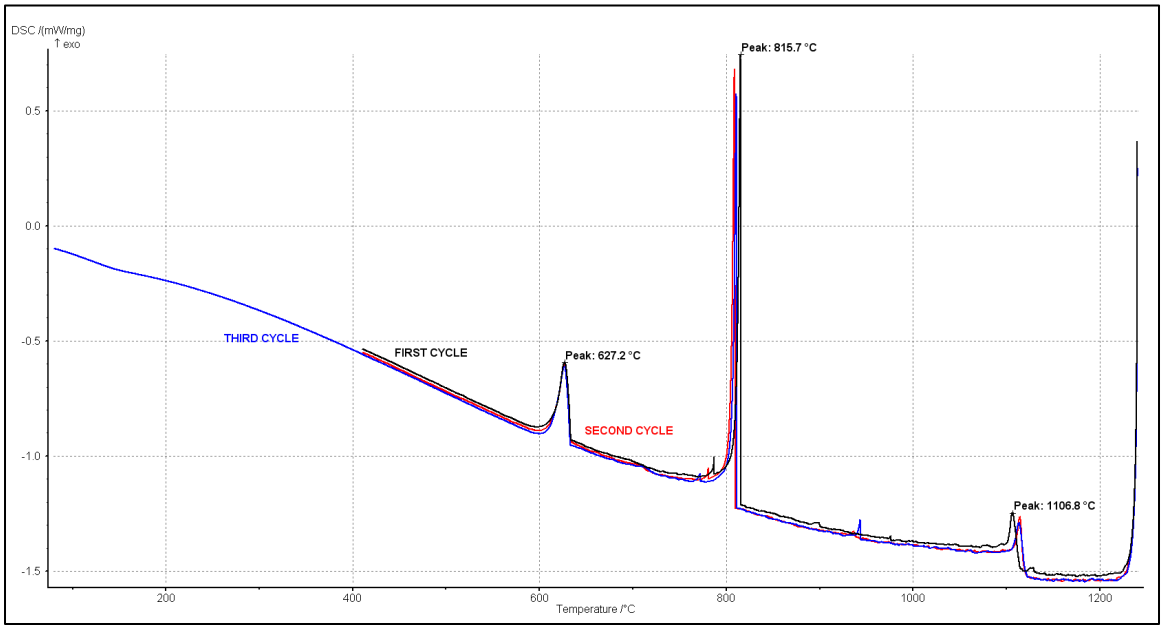


Figure 4-32 DSC Cooling curves of three separate $NiAl_3$ cycles. Primary solidification peak observed at ~820°C with smaller solidification peaks observed at ~1110°C and ~630°C

4.5.3 $NiAl_3$ Infiltration at Intermediate temperature

For a wetting system, infiltration can be considered a “spontaneous” process, in that if there is liquid present then it will wick into a capillary at a very fast rate via capillary action. According to the Ni-Al phase diagram an Al-rich liquid is forming well before the fully liquid point of $NiAl_3$. Experimental melting of $NiAl_3$ shown in the previous section demonstrates an Al-rich phase significantly segregates from the overall alloy at some point during melting and solidification. If there is indeed the separation of an Al-rich liquid well before the fully liquid point of $NiAl_3$, and this liquid wets TiC, then perhaps this Al-rich liquid is wicking into and saturating the TiC preform before the alloy has become fully liquid. It would then be expected that infiltration would occur at a considerably lower temperature than the peak temperature of the infiltration cycle.

To investigate this further, $NiAl_3$ was infiltrated into a TiC preform (~50% dense) at 1000°C for 30 minutes (Sample S2) in an alumina tube furnace under Ar/4% H_2 atmosphere with a heating rate of 6.67°C/min. Previous infiltration experiments of $NiAl_3$ into a TiC preform were done at 1415°C. This temperature falls in the mixed liquid + solid phase field where the Al-rich liquid is ~88 at.% Al and is present alongside solid Ni_2Al_3. At this temperature, the lever rule can be applied to determine the approximate amount of liquid that should be present, calculated to be ~75 wt. % liquid. The density of the liquid phase is assumed to be that of $NiAl_3$ (3.96g/cc) for calculation of the required amount of metal powder to fill the void space. In reality, the density will be lower if the liquid has a higher Al content and thus will require less material than calculated. Based upon a preform weight of ~4.1g, ~3.5g of $NiAl_3$ is required to fill the entire void space of the preform. Assuming ~75 wt.% of the alloy is liquid at 1000°C, the preform was set on a bed of ~4.8g of $NiAl_3$ where 3.5g is equal to 75 wt.% of the total powder.

No infiltration of the TiC preform by liquid occurred; confirmed by weighing the preform before and after the infiltration cycle and also by visual inspection. Despite the lack of infiltration there is a clear indication of melting behavior of the $NiAl_3$ powder indicated by the presence of solidified Al-rich phase that has segregated from the alloy, shown in Fig. 4-33. A complete lack of infiltration at intermediate temperatures where the Al-rich liquid is present suggests the Al-rich liquid does not wet TiC and instead successful infiltration of the TiC preform occurs above the fully liquid point where the liquid is of bulk composition $NiAl_3$.



Figure 4-33 Sample S2 (left) shows complete lack of infiltration. Material remnant (right) left in crucible shows clear melting behavior and segregation of Al-rich phase

4.6 $NiAl_3$ Microstructure Analysis & Solidification Behavior

4.6.1 Al-rich phase within TiC inter-particle area

The solidification behavior and resulting microstructure of the base $NiAl_3$ alloy have been studied in the previous sections by SEM, EDS, XRD, and DSC and follow closely that predicted by the Ni-Al phase diagram: a three phase microstructure composed of Ni_2Al_3, $NiAl_3$, and Al. Initial inspection of the $NiAl_3$ infiltrated microstructure reveals the same expected phases of $NiAl_3$ and Ni_2Al_3, but no clear indication of the darker Al phase. TiC particles and clusters exist within the $NiAl_3$ phase where the dark, Al phase would have been expected. XRD results of Sample 6, infiltrated by $NiAl_3$, were shown previously and confirmed only the presence of $NiAl_3$ and Ni_2Al_3 without any indication of an Al-rich phase. However, a closer look at the microstructure of the infiltrated preform reveals the inter-particle spacing within TiC clusters appears to contain a very dark phase, shown in Fig. 4-34. Many of these black areas are large porosity scattered throughout the part, but with the help of a high contrast setting in SEM, the porosity can be differentiated from a dark phase that exists only within clusters of TiC. EDS mapping of these areas, shown in Fig. 4-35, reveals the dark inter-particle area to be rich in Al compared to the surrounding $NiAl_3$ matrix but may also contain residual amounts Ti, which might be a result of Ti leaching from the surrounding TiC particles. Accurate quantitative EDS analysis within SEM of this dark phase was not possible given the high density of surrounding TiC particles.

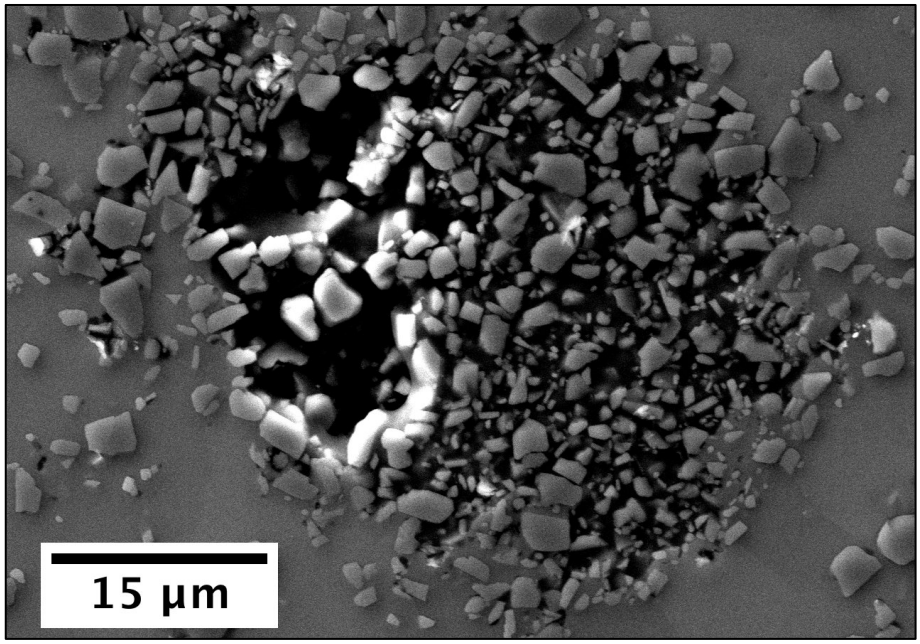


Figure 4-34 SEM image of Sample 5, infiltrated at 1415°C for 30 mins by $NiAl_3$. Cluster of TiC particles shown where high contrast reveals the porosity against dark inter-particle matrix phase

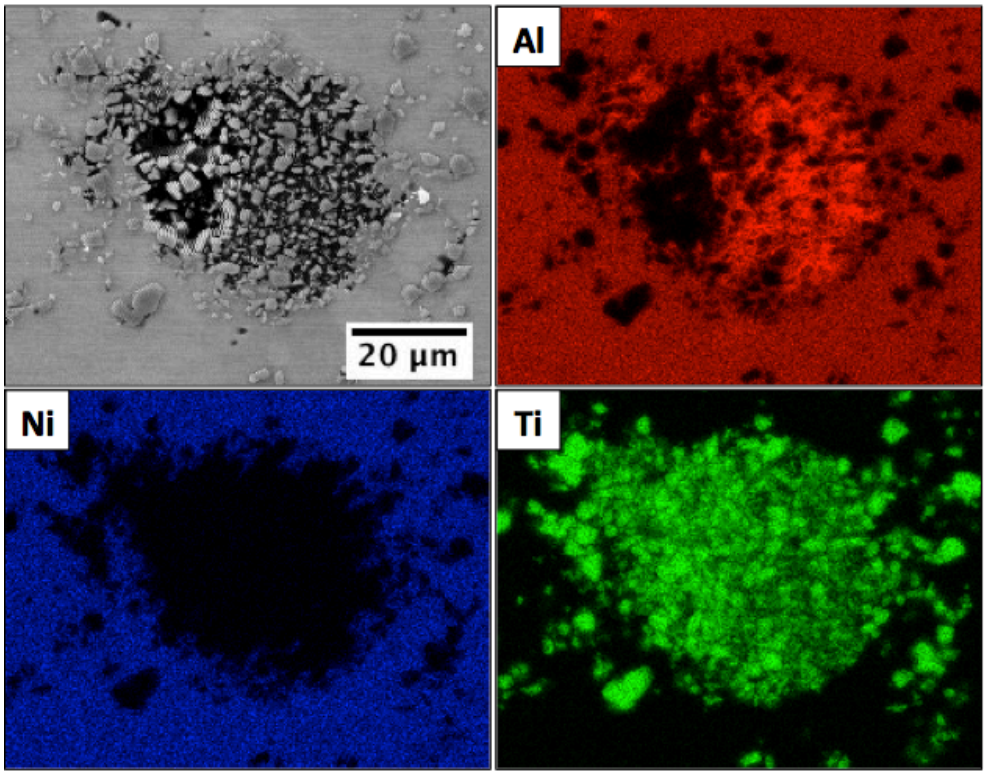


Figure 4-35 EDS map of TiC cluster in Sample 5. Inter-particle area has Al-rich matrix phase with no detected Ni alongside porosity. 1,500x magnification

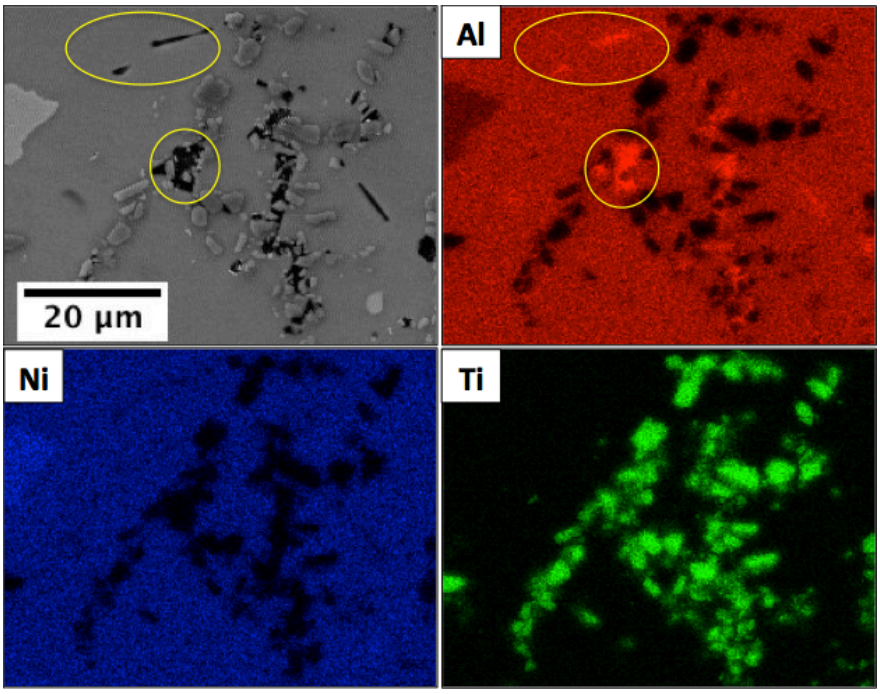


Figure 4-36 EDS map of Sample 5 shows black phase adjoined and near to TiC particles that appear to be Al-rich with little to no Ni and Ti. 2,000x magnification

In addition to select areas within TiC clusters being Al-rich, there appears to be small black, faceted features scattered throughout the microstructure that are much more visible around dispersed TiC particles that exist outside or near the larger clusters. These features appear to be Al-rich and, based upon the black rod shaped features shown in Fig. 4-36, do not contain any Ti, although the same features that interface with TiC particles may have small amounts of Ti through leaching from TiC. Based upon Figs. 4-35 & 4-36, the Al-rich black phase appears to have largely nucleated around TiC particles, which gives an indication that this phase might possibly be a reaction product. With the lack of measured Ti, it could possibly be the formation of Al_4C_3, but EDS cannot confirm this due to the inability to accurately measure carbon. Qualitative measurements of carbon by mapping proved to be difficult as well. An exception to the above observation is the presence of the black, rod-shape features (circled at top of Fig. 4-36) that appear within the $NiAl_3$ matrix away from a TiC interface.

Certainly, the “capillaries” present within the infiltrated preform are intuitively considered as the open porosity within the overall TiC particle network structure, which measure to be ~20-40µm using ImageJ. However, individual clusters of TiC particles may be considered to be a bundle of “micro” capillaries represented by the individual TiC particle spacing. Measurements using ImageJ reveal the inter-particle TiC spacing to be 0.1-1µm and the larger “macro” capillaries between clusters of TiC to be 20-40µm. Remember, the pore radius assumed by Plucknett & Becher in their assumptions for the Lucas-Washburn equation was ~0.23µm - within the same range

as the “micro” capillary shown in this work. Also remember the capillary pressure (the driving force for infiltration shown by Eq. 4) is inversely proportional to pore radius, which means the driving force for infiltration into the “micro” capillaries between individual TiC particles will be higher than that for the “macro” capillaries between clusters of TiC. This will be expanded upon in the next section.

4.6.2 $NiAl_3$ Infiltrated Matrix Microstructure

Upon closer inspection of the $NiAl_3$ infiltrated microstructure, it becomes apparent that TiC particles reside only within the $NiAl_3$ matrix while regions of Ni_2Al_3 are completely devoid of TiC particles. An example of this is shown in Fig. 4-37. Based upon the phase diagram shown previously, Ni_2Al_3 is the first phase to nucleate upon cooling from liquid and will continue to solidify over a large temperature range until the remaining Al-rich liquid eventually solidifies as $NiAl_3$ and then finally Al. During the solidification process, solid TiC particles remain in the liquid and essentially act as an inoculant providing an existing solid-liquid interface upon which heterogeneous nucleation should occur.

According to traditional nucleation theory, heterogeneous nucleation is more energetically favorable than homogeneous nucleation where solid would begin to nucleate within the liquid. It would then be expected that Ni_2Al_3, as the first phase to solidify, would nucleate at the TiC interface and as the infiltrated preform is cooled further the Al-rich liquid away from the TiC particles at the Ni_2Al_3 interface would solidify as $NiAl_3$, and then Al. The expected microstructure would then be TiC particles surrounded by areas of Ni_2Al_3, then $NiAl_3$, then Al and/or Al/$NiAl_3$ eutectic, shown in Fig. 4-38. Another possibility for the microstructure could be the formation of small amounts of NiAl B2 surrounding TiC. As the liquid with bulk composition $NiAl_3$ is cooled, the NiAl B2 phase field falls within a single at. % near the liquidus point. If the liquid were slightly Ni-rich, then solidification would begin with NiAl and the remaining liquid would solidify as described above. A microstructure following these solidification conditions would then show small amounts of NiAl B2 around TiC and then a progressive microstructure of Ni_2Al_3, $NiAl_3$, and Al or Al+$NiAl_3$ eutectic, shown in Fig. 4-39.

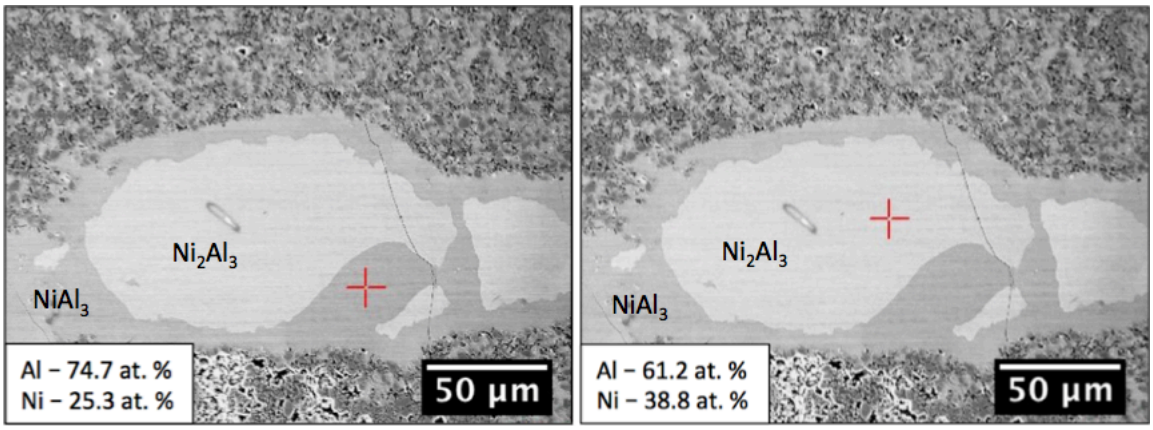


Figure 4-37 EDS Point Scan of Sample 6 confirms dark matrix phase to be NiAl3 and light matrix phase to be Ni2Al3. TiC particles reside only within NiAl3 matrix.

For the two solidification theories described, the microstructure is compositionally graded such that the most Ni-rich phases exist at the TiC particle interface and Al content rises with increasing distance away from TiC. However, the experimentally shown microstructure (Fig. 4-37) reveals the more Ni-rich phase Ni_2Al_3 exists furthest away from the TiC particles, which cannot be explained by traditional solidification, described using the phase diagram during cooling. The assumption with the above theories is that a single liquid of bulk composition $NiAl_3$ has infiltrated the preform and then undergone solidification with heterogeneous nucleation at the TiC interface. However, it was shown in the previous section the possibility that the Al-rich liquid that forms at ~620°C may be infiltrating the "micro" capillaries of the TiC clusters before infiltration of the "macro" capillaries of the preform. This "metered" infiltration process may occur due to the complex melting behavior of the $NiAl_3$ alloy where liquid forms at multiple stages of varying composition. Could then a "metered" infiltration process also occur within the "macro" capillaries of the preform upon further heating?

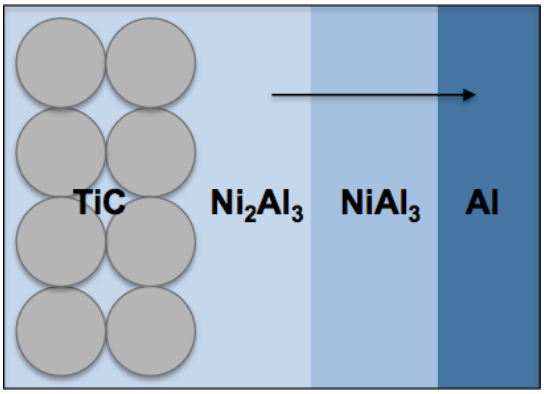


Figure 4-38 Solidification Theory 1

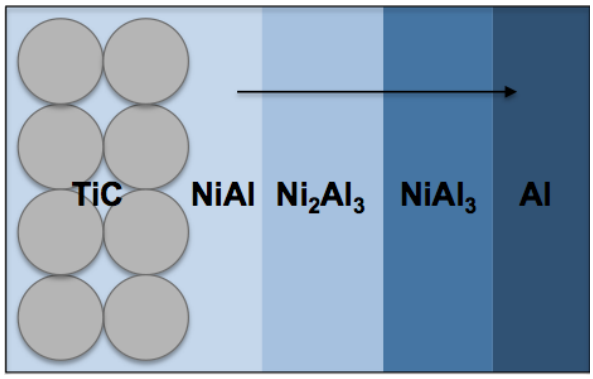


Figure 4-39 Solidification Theory 2

At ~850°C $NiAl_3$ decomposes to a mixture of Ni_2Al_3 and Al-rich liquid. If this Al-rich liquid were to separate and infiltrate the TiC preform first, then what would be left in the crucible is solid Ni_2Al_3. It was shown previously in section 4.5.3 that no infiltration likely occurred by this Al-rich liquid at 1000°C, but as the liquid enriches in Ni with increasing temperature infiltration may still occur above this point by the same liquid. With the composition of the solid phase now that of Ni_2Al_3, further heating to ~1170°C will result in the decomposition of Ni_2Al_3 to a mixture of NiAl B2 solid and a liquid phase that is more Ni-rich than the bulk composition $NiAl_3$. If the "macro" capillaries of the preform have yet to be fully saturated by the earlier Al-rich liquid, then this Ni-rich liquid could potentially wick into the preform. The Al-rich liquid would then surround TiC clusters and the Ni-rich liquid would fill the remaining void space away from TiC. Upon cooling, solidification of the compositionally graded liquid results in the more Al-rich $NiAl_3$ phase surrounding the TiC particles and the Ni-rich Ni_2Al_3 existing at the $NiAl_3$ interface. Then, the remnant material in the crucible would be solid NiAl B2 that does not undergo melting during the infiltration process and experiences solid state decomposition to include $NiAl_3$ + Ni_2Al_3 and/or NiAl B2 and would explain why the remnant material after infiltration does not show a clear melting behavior. The possible presence of NiAl within the remnant material requires that further analysis of XRD data be done to confirm the phases present since Ni_2Al_3 and NiAl diffraction patterns are extremely similar.

Overall, it appears that the experimentally observed microstructure cannot be explained by traditional solidification assuming infiltration of a single liquid front of bulk composition $NiAl_3$. Further, the presence of an Al-rich phase within the TiC clusters indicates the possibility of a "metered" infiltration process where liquids of varying compositions may infiltrate the "micro" and "macro" capillaries of the TiC preform in a staggered fashion. A "metered" infiltration process provides a potential explanation for the experimentally observed microstructure where an Al-rich liquid first infiltrates the "macro" capillaries followed by a more Ni-rich liquid. If there is a highly Al-rich (< ~95 at. % Al) liquid first infiltrating the "micro" capillaries of the TiC clusters, will the presence of TiC alter the local solidification behavior of the liquid?

4.6.3 Local TiC Interface Simulation by CALPHAD

ThermoCalc CALPHAD software used to simulate the local solidification behavior of the system using the Scheil module. A simulation of the local TiC interface may be considered by assuming a 1:1 molar ratio of TiC and $NiAl_3$. The solidification behavior as a function of temperature can then be modeled by a Scheil simulation, which determines solidification according to the Gulliver-Scheil equation. The Gulliver-Scheil equation is a solute re-distribution law that assumes no diffusion within the solid phase, infinitely fast mixing of solute in the liquid, and equilibrium only at the local solid-liquid interface. Assuming local equilibrium allows phases within the equilibrium phase diagrams to be used. One can think of equilibrium and Scheil as being two "limits" of solidification where reality falls somewhere in between these two conditions. It is important to remember that a Scheil simulation begins at complete liquid, yet within this system solid TiC is already present.

A Scheil simulation showing the solidification behavior of a 1:1 molar ratio of TiC and $NiAl_3$ is shown below in Fig. 4-40. The dotted line represents the equilibrium solidification and predicts full solidification much earlier than the Scheil condition. The solidification behavior predicted by the Scheil simulation can be described as follows. Initially, a liquid saturated by Ti and C and will begin to form TiC (FCC_L12) upon cooling at ~3050°C and the liquid will move toward the bulk $NiAl_3$ composition. At ~1850°C, aluminum carbide Al_4C_3 will begin to solidify and the driving force for this solidification will remain until reaching the $NiAl_3$ phase field at ~830°C. With further cooling to ~1200°C, there is a small window of NiAl (BCC_B2) solidification, which quickly gives way to Ni_2Al_3. Finally, $NiAl_3$ will begin to solidify at ~830°C and will continue until full solidification has occurred. Notably, there is no driving force for the nucleation of FCC Al predicted by the Scheil simulation. As Al_4C_3 nucleates, the composition of the liquid becomes slightly Al-depleted and shifts into the NiAl (B2 phase field).

Thus, the microstructure predicted by the Scheil simulation is very close to the one described above that begins with NiAl solidification, only now the nucleation of Al_4C_3 is predicted. ThermoCalc does not tell you the location at which each phase solidifies, but Al_4C_3 will nucleate at or near the TiC interface due to the presence of C.

4.6.4 High Temperature DSC Dissolution at Local Interface Simulation

Scheil simulation by ThermoCalc indicates several key results that differ from the equilibrium solidification, mainly the solidification of Al_4C_3, small amounts of NiAl B2, and no solidification of FCC Al. An attempt was made to experimentally validate this predicted solidification behavior by the use of high temperature DSC. Similar to ThermoCalc, a 1:1 molar ratio of TiC and $NiAl_3$ powders were mixed together as a representation of the local interface. In order to simulate the dissolution of TiC that

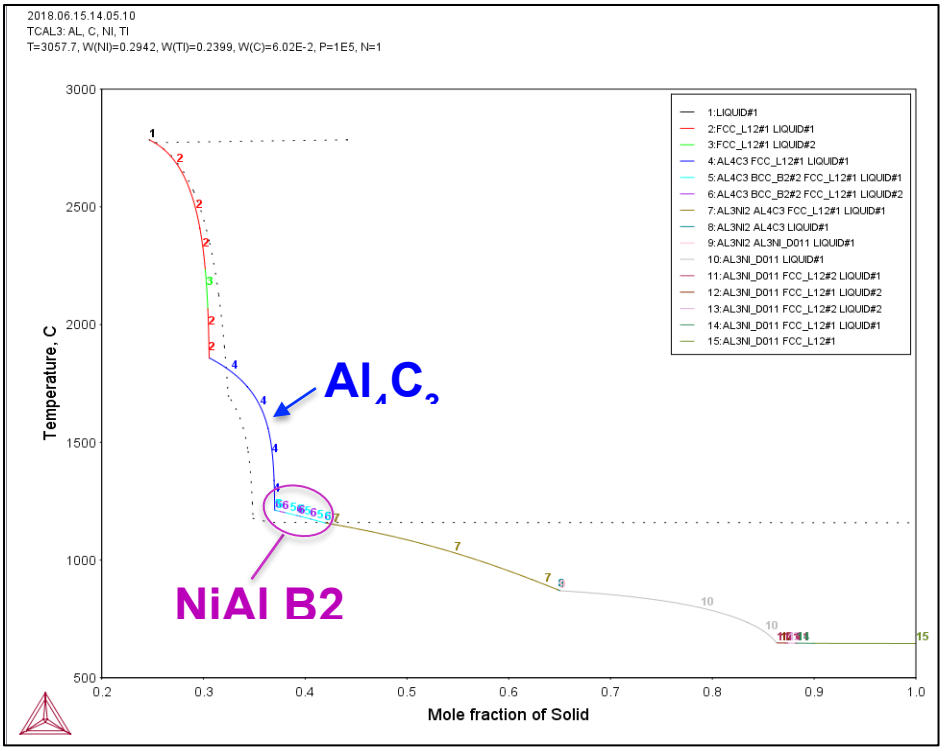


Figure 4-40 Scheil simulation depicting solidification behavior of 1:1 molar ratio of TiC and $NiAl_3$. Simulation conducted in ThermoCalc software with TCAL3 database. Dotted line represents the equilibrium calculation

might be occurring during infiltration, the powder mixture was heated to 1400°C and held for 30 minutes to simulate infiltration conditions. In Fig. 4-41, the initial heating cycle is shown by the red curve where the sample was heated at 10°C/min up to 1400°C and held for 30 minutes. The sample was then cooled down to 400°C (green curve) and cycled back up to 1200°C (blue curve) before finally cooling back to room temperature (purple curve).

In comparison to the melting and solidification behavior of the base $NiAl_3$ alloy shown in Figs. 4-31 and 4-32, the same melting peaks are observed at ~830°C and 1130°C, likely corresponding to the first decomposition of $NiAl_3$ into Ni_2Al_3 (s) + Al-rich liquid and the liquidus point respectively. The same solidification peaks are observed at ~750°C and 1130°C. The first difference to note is the primary solidification peak has shifted from ~830°C to ~750°C. Secondly, and most notably, the melting and solidification peaks at ~620°C, which correspond to the formation of FCC Al, are absent.

Thermodynamic calculations indicate the formation of Al_4C_3 at the TiC interface along with potential formation of small amounts of NiAl B2. There is no prediction for the solidification of Al, which is also correlated by experimental high temperature DSC results. Additionally, XRD of the $NiAl_3$ infiltrated preform does not give any indication of Al or an Al-rich phase and SEM analysis shows Al-enrichment within the TiC inter-particle area but no strong evidence for an obvious FCC Al microstructural phase. The

formation of Al_4C_3 at the local interface is interesting, as it is a lower density phase (2.93g/cc) compared to $NiAl_3$ (3.96g/cc) and could provide an explanation for the lack of shrinkage (at least partially) by result of a displacement reaction. However, there is currently no visual or compositional evidence for Al_4C_3 or NiAl B2 by SEM and EDS.

4.7 Characterization of TiC Interface by TEM

While Thermodynamic simulation predicts the formation of Al_4C_3, this is not confirmed using SEM or EDS. It is possible the black, faceted features shown earlier are Al_4C_3, but that remains unknown. The TiC interface can be inspected in greater detail by using TEM. Shown below in Fig. 4-42 is a bright field TEM image of the TiC/matrix interface. The light region to the left is the TiC particle while the grey region in the bottom right is the metallic matrix. The dark feature in the upper right is a yet unknown feature. The dark layer along the boundary of the TiC particle may be slightly Ti-enriched, but requires further analysis to confirm. Electron diffraction patterns for each phase were taken and indexing of these patterns will provide insight into the crystal structure of each phase. Specifically, the crystal structure of the matrix phase and its coherency with the TiC particle is of particular interest to study if solidification occurred at the TiC interface and if the matrix is the base $NiAl_3$ phase. Indexing of the electron diffraction patterns will be included in future work.

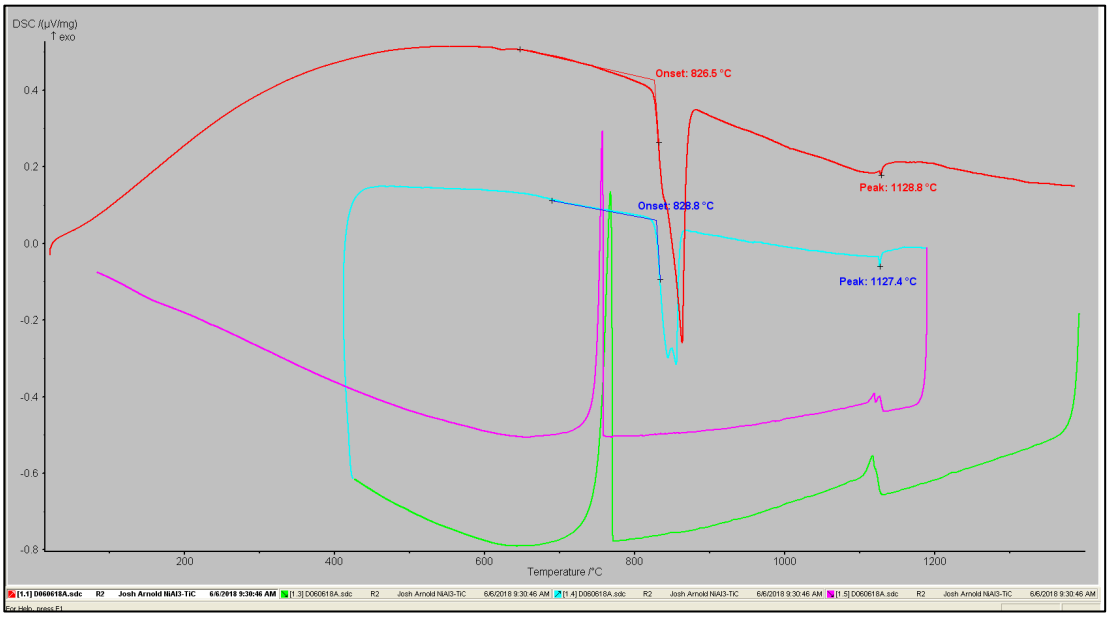


Figure 4-41 DSC Analysis of 1:1 molar ratio TiC:NiAl3. The sample was ramped up to 1400°C and held for 30 mins to simulate TiC dissolution during infiltration processing

In particular, the clear presence of ledges can be seen along the interface of the metallic matrix and TiC particle. This phenomenon possibly represents a lateral growth mechanism of solidification and generally indicates nucleation has occurred at the interface, however this cannot be confirmed without determining coherency between the TiC particle and matrix phase. A ledge effect is well documented for TiC in composite systems, particularly within a Ni_3Al matrix [78], [80]–[84]. Generally, the presence of a ledge effect is documented by TiC particles that have precipitated *in-situ* and then coarsen by further absorbing Ti and C from the liquid. Within this work, TiC particles exist as a solid throughout the infiltration process and have no method of traditional coarsening. Conversely, the dark contrast of the ledges could represent stacking faults at the interface.

A black layer can be seen along the TiC/matrix interface, which EDS mapping shows to be potentially Ti-enriched compared to the base TiC particle (Fig. 4-43). This is a possible indicator that carbon has left TiC and entered the matrix, either by solution within the liquid or an interfacial reaction product such as Al_4C_3. Visually, there is no indication of Al_4C_3 but this may be confirmed later by analysis of the electron diffraction patterns of the TiC particle, interfacial layer, and matrix phase. A secondary explanation for the Ti-enrichment could be due to a thinning of the sample locally compared to either the TiC particle or interface and requires further analysis.

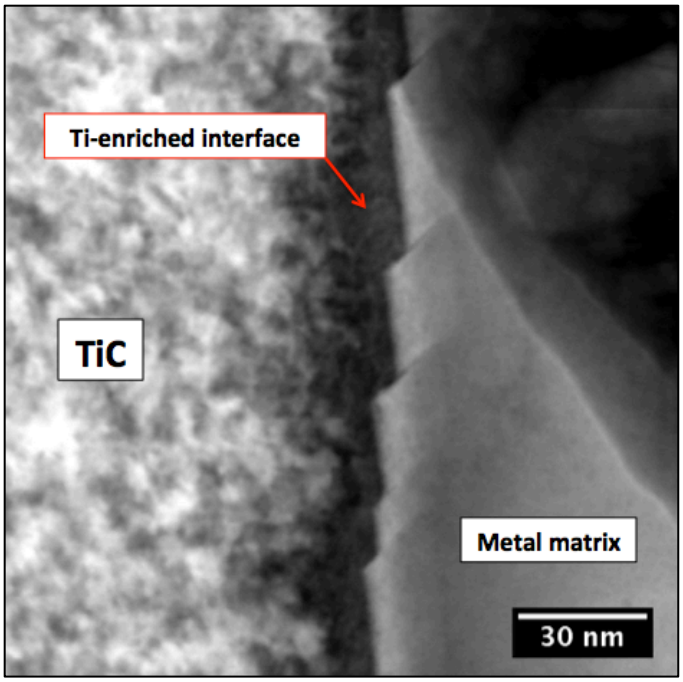


Figure 4-42 Bright field TEM image of TiC interface. Ledges are seen along the TiC/matrix interface

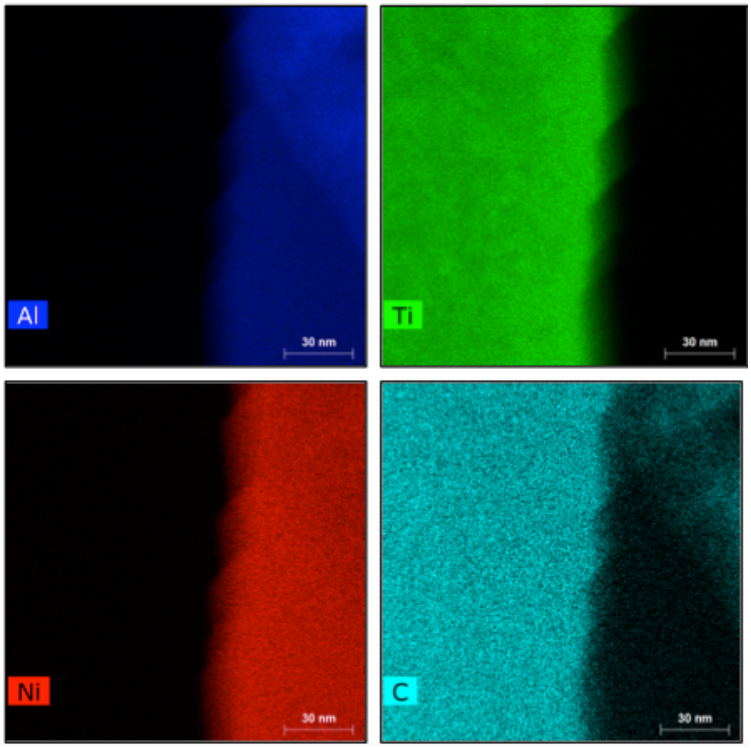


Figure 4-43 EDS Map of TiC interface for Bright Field TEM Image shown in Fig. 4-42

4.8 Infiltration of TiC by $NiAl_3$ + Al Mixture

For a TiC preform infiltrated by $NiAl_3$, it is clear that porosity is present in the preform after infiltration with a % theoretical density of ~88-90%. Additionally, attempted tensile testing of a $NiAl_3$ infiltrated TiC dog bone resulted in the sample fracturing by simply being clamped in the jaws of the tensile machine signifying brittle behavior. It is thought that perhaps the complex solidification behavior of the alloy is contributing to the porosity within the infiltrated preform and also the brittle behavior, specifically as a result of the formation of Ni_2Al_3. This Ni-rich phase has a density higher than $NiAl_3$ (4.7g/cc vs. 3.96g/cc) and also a considerably higher hardness, upwards of 11-12 GPa [24]. The current microstructure of the $NiAl_3$ infiltrated preform is a dual-phase microstructure of two complex crystal structures in $NiAl_3$ (orthorhombic) and Ni_2Al_3 (trigonal) and the solidification of the higher density Ni_2Al_3 could be contributing to the porosity of the preform.

It was hypothesized that a preform with better ductility and less porosity could be obtained by removing the Ni_2Al_3 phase by using a more Al-rich infiltrate material such that the end microstructure would instead be $NiAl_3$ dispersed within an Al-matrix, similar to the eutectic structure. Additionally, the removal of Ni_2Al_3 and the introduction of an Al-matrix would further reduce the density of the preform. To address this, a TiC preform was infiltrated with $NiAl_3$ powder mixed with Al ingots. The

target composition was 90 at. % Al and 10 at. % Ni, which was a safe estimate given that the exact composition and amount of liquid infiltrating the TiC preform remains unknown. Based upon a preform (~50% dense) weight of ~3.95g, ~3.167g of $NiAl_3$ is required to fill the void space calculated using the methodology shown in section 4.2.1. The methodology for determining the amount of infiltrate material is shown below.

The weight fractions of Al and Ni within $NiAl_3$ are 0.5797 and .4203 respectively. Assuming 3.167g of $NiAl_3$, the respective amounts of Al and Ni are:

$$0.5797 * 3.167 = 1.835g\ of\ Al$$

$$.4203 * 3.167 = 1.331g\ of\ Ni$$

The target composition of the infiltrate material is 90 at. %, 10 at. Ni. The weight fractions of Al and Ni are 0.8053 and 0.1947 respectively. The amount of additional Al to be added to the $NiAl_3$ powder in order to reach the target composition is:

$$\frac{80.53g}{19.47g} = \frac{x}{1.331g\ of\ Ni} \rightarrow x = 5.505g\ of\ Al\ total$$

$$5.505 - 1.835 = 3.67g\ of\ additional\ Al$$

For the infiltration experiment, ~3.6g of Al ingots were set in the bottom of an alumina crucible then ~3.16g of NiAl powder was poured over the Al ingots for a total amount ~6.76g of infiltrate material provided for infiltration with ~5.5g of Al total. A TiC preform was then placed upon the ingot and powder mixture. By adding Al ingots to the already assumed required amount of $NiAl_3$ in order to reach the target composition, there is a significant amount of excess material provided for the infiltration process. Based upon a preform weight of ~3.944g, ~2.16 of pure Al or ~3.167g of $NiAl_3$ would be required to fully infiltrate the preform and as such the required amount of infiltrate material for a 90 at. % Al, 10 at. % Ni mixture would be within this range. However, as shown previously in section 4.2.3, $NiAl_3$ exhibits a partial melting and infiltration behavior and thus it is unclear exactly how much liquid will be available to infiltrate the preform and what the composition and density of the liquid phase are. Infiltration was conducted at 1415°C for 30 minutes using Furnace 1 (10°C/min heating rate) under Ar/4% H_2.

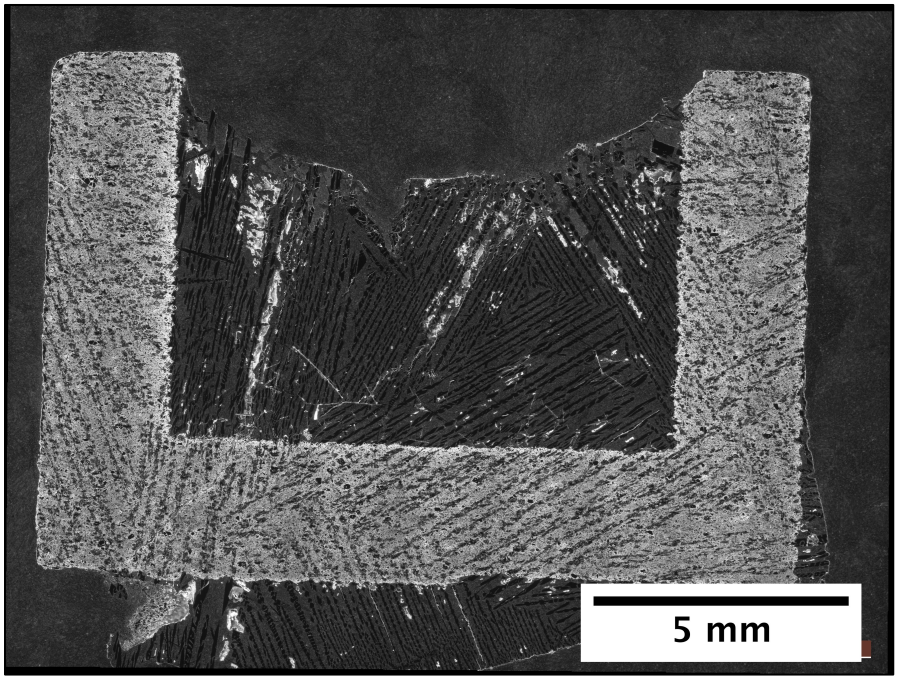


Figure 4-44 Optical cross-section of TiC preform infiltrated with NiAl3 + Al at 1415°C for 30 mins. Significant crystal growth is visible inside cavity of preform and also fused to bottom of preform**.**

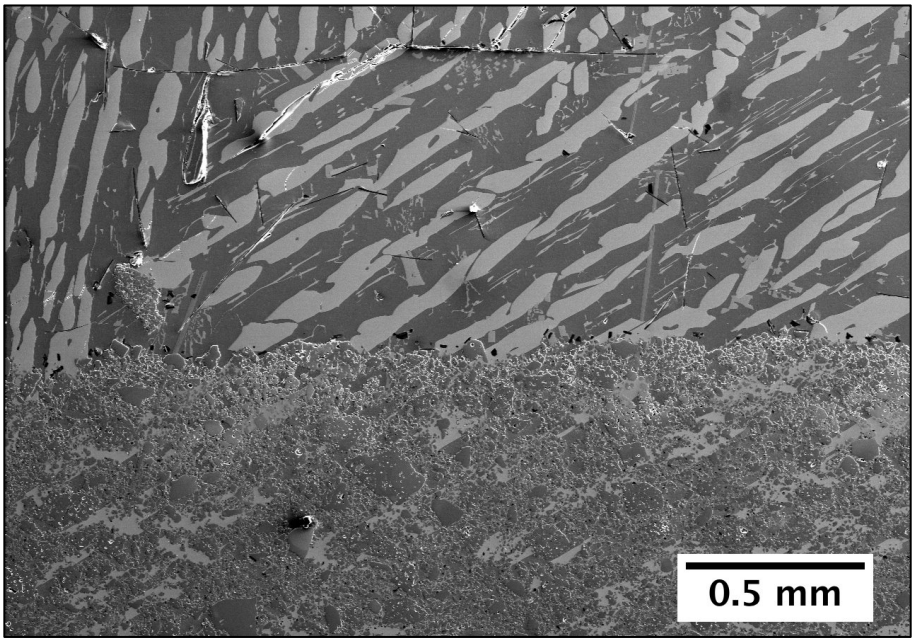


Figure 4-45 Top of infiltrated preform showing region of crystal growth in cup cavity. Crystal growth regions show light colored dendrites (NiAl3) within a dark (Al) matrix

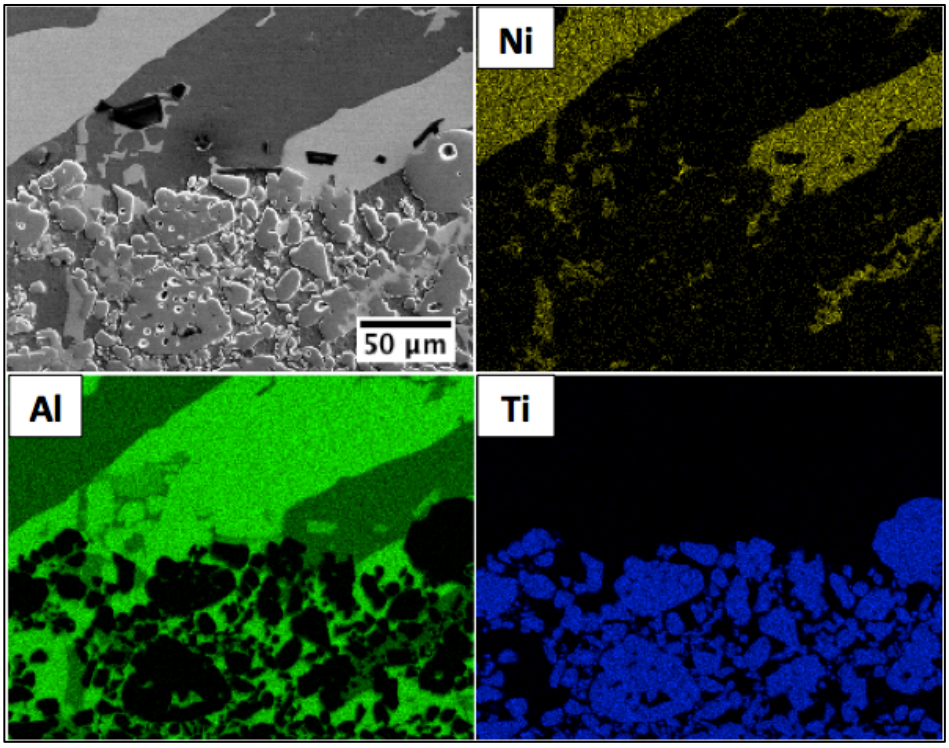


Figure 4-46 EDS Mapping of sample at bottom of crystal growth showing TiC particles dispersed in a matrix of NiAl3 + Al

The infiltration results are shown in Fig. 4-44-4.46. Firstly, it is observed that full infiltration of the TiC preform occurred with excellent shape retention. The infiltrated density has yet to be measured but optical cross-section visually shows much less porosity than the $NiAl_3$ infiltrated preform. Most notably, there appears to be a significant amount of crystal growth in the cavity of the preform, despite infiltrate material being placed beneath the preform only. There is also solidified metal beneath the preform. Analysis of the crystal growth region within the cavity shows $NiAl_3$ dendrites dispersed in an Al-matrix, confirmed by EDS quantitative point analysis. More in-depth analysis is required to determine if the composition of the matrix within the infiltrated preform matches that observed within the crystal growth region in the cavity. It was discussed previously in section 4.6 that an Al-rich liquid, or even that of composition $NiAl_3$, can react with TiC to form Al_4C_3 at the local interface. If such a reaction were to occur then it might be expected that the composition of the matrix metal would be different in the crystal growth below the preform, within the infiltrated preform, and the cavity crystal growth. If a reaction with TiC were to occur then the TiC preform could act as sort of a “filter” of the liquid infiltrate. Investigation of this will be the subject of future work and could provide valuable insight into the results of the base $NiAl_3$ infiltration including microstructure and interfacial reaction products.

The crystal growth within the preform cavity represents a significant volume and is likely a result of the significant amount of excess material provided for the

infiltration process. However, where excess material after previous $NiAl_3$ infiltration remained in the bottom of the crucible, excess material in this instance flows through and grows into the cavity of the preform. Moving forward, the amount of infiltrate material should be reduced to view the effects on the volume of the observed crystal growth.

While the results shown in this section are only preliminary, they prove to be promising where the infiltrated preform has excellent shape retention and appears to have a higher infiltrated density compared to infiltration by base $NiAl_3$. Additionally, the desired microstructure of an Al matrix with dispersed $NiAl_3$ phase was achieved that will potentially lead to better ductility. Crystal growth was observed in the preform cavity and raises interesting questions that should be the focus of future works that may provide valuable insight into the infiltration process.

5 Summary, Conclusions, & Future Work

5.1 Conclusions

Within the scope of the research contained in this study, it was shown that obtaining a fully infiltrated cermet with good shape retention is feasible. However, it was also shown that the wetting behavior of the liquid infiltrant on the printed carbide feedstock has a large effect on the shape retention of the infiltrated alloy. Additionally, the formation of a reaction product during $NiAl_3$ infiltration may play a role in the shape retention. Specifically, this work was able to demonstrate the following:

1. Through the use of binder jet additive manufacturing, a preform with a cubic cup geometry with features of varying thickness was infiltrated with good shape retention. While porosity remains a present challenge, the ability to infiltrate a printed TiC preform by a nickel aluminide alloy was shown.
2. It was shown that the TiC particles are arranged in an interconnected network structure as a result of the binder jetting print process and that it is this network that is responsible for the shape retention of the preform during and after infiltration. Ni_3Al wets TiC with a very low contact angle and thus dissolves TiC to such an extent that this network shape is lost and the structural integrity of the preform is compromised.
3. The melting and solidification behavior of Ni_3Al is very straightforward as predicted by the single-phase regime in the binary phase diagram. $NiAl_3$, on the other hand, has a much more complex melting and solidification behavior as indicated also by the phase diagram. However, it was learned that $NiAl_3$ exhibits a significant segregation of an Al-rich liquid phase that forms before the fully liquid point is achieved. This complex melting behavior of $NiAl_3$ leads to only partial infiltration of the TiC preform. Additionally, the source of the present porosity in the $NiAl_3$ infiltrated preform is still to be determined but appears to be related to solidification as evidenced by a higher density being achieved through using a more Al-rich alloy that avoids the Ni_2Al_3 phase regime entirely.

5.2 Suggestions for Future Work

The complex, and still unknown, melting and solidification behavior of $NiAl_3$ could be better understood through in-situ measurements and phase evaluation during the infiltration process. High-speed video of the infiltration process would shed light on the melting and segregation phenomenon of $NiAl_3$ and also the infiltration kinetics of the liquid metal wicking into the TiC preform. In-situ phase analysis would

allow the solidification behavior of the $NiAl_3$ infiltrated preform to be better understood.

The cause for the present porosity in the $NiAl_3$ preforms is still unknown, but likely linked to the complex solidification behavior of $NiAl_3$, particularly with the Ni_2Al_3 phase. Elimination of the Ni_2Al_3 phase by additions of excess Al resulted in a higher % theoretical density and removal of large porosity, which indicates porosity within the $NiAl_3$ infiltrated preform is possibly linked to the formation of Ni_2Al_3. However, the significant amount of crystal growth within the Al-excess infiltrated preform should be a priority moving forward. Firstly, lesser amounts of $NiAl_3$+Al should be used to infiltrate a TiC preform and confirm how much of the crystal growth is a result of simply using excess infiltrate material. Secondly, the composition of the crystal growth regions beneath the preform and also within the cavity of the preform should be analyzed and compared.

During preliminary TEM analysis, electron diffraction patterns were taken of the TiC particles and matrix phase in addition to a second, unknown feature. Indexing of these patterns will be included in future work to identify the possible crystal structure of each phase. Comparing the diffraction patterns of the TiC particle and matrix phase under a same zone axis will provide insight into a possible coherent interface that might suggest solidification upon the TiC particle.

Infiltration of Sample B1, a TiC preform (~50%) with a bimodal powder distribution of TiC, showed a noticeably different microstructure than the original infiltrated preforms that contained a single distribution of -325 mesh TiC. The microstructure shows a significantly higher amount of a black phase similar to the melted, pure $NiAl_3$. The infiltration kinetics of the bimodal preform may be different than the single distribution -325 mesh preforms that could influence the solidification behavior of the alloy, specifically how the “macro” and “micro” capillaries compare between the two preforms. A more detailed analysis, including SEM and XRD, will be conducted on this sample.

References

[1] ASTM International, “F2792-12a - Standard Terminology for Additive Manufacturing Technologies,” *Rapid Manuf. Assoc.*, pp. 10–12, 2013.
[2] A. M. Elliott and L. J. Love, “Overview of Additive Manufacturing Technologies for the Rapid Equipping Force: Final Report,” 2014.
[3] A. Levy, A. Miriyev, A. Elliott, S. S. Babu, and N. Frage, “Additive manufacturing of complex-shaped graded TiC/steel composites,” *Mater. Des.*, vol. 118, pp. 198–203, 2017.
[4] I. A. Ibrahim, F. A. Mohamed, and E. J. Lavernia, “Particulate reinforced metal matrix composites - a review,” *J. Mater. Sci.*, vol. 26, no. 5, pp. 1137–1156, 1991.
[5] N. Chawla and K. K. Chawla, *Metal Matrix Composites*. New York, NY: Springer New York, 2013.
[6] A. Mortensen and J. Llorca, “Metal Matrix Composites,” *Annu. Rev. Mater. Res.*, vol. 40, no. 1, pp. 243–270, Jun. 2010.
[7] J. . Torralba, C. . da Costa, and F. Velasco, “P/M aluminum matrix composites: an overview,” *J. Mater. Process. Technol.*, vol. 133, no. 1–2, pp. 203–206, Feb. 2003.
[8] J. Davis, “No Title,” in *ASM Specialty Handbook: nickel, cobalt, and their alloys*, ASM International, 2000, pp. 104–105.
[9] C. T. Liu, R. W. Cahn, and G. Sauthoff, Eds., *Ordered Intermetallics — Physical Metallurgy and Mechanical Behaviour*. Dordrecht: Springer Netherlands, 1992.
[10] J. M. Yang, W. H. Kao, and C. T. Liu, “Development of Nickel aluminide matrix composites,” *Mater. Sci. Eng. A*, vol. 107, no. C, pp. 81–91, 1989.
[11] S. C. Deevi and V. K. Sikka, “Nickel and iron aluminides: An overview on properties, processing, and applications,” *Intermetallics*, vol. 4, no. 5, pp. 357–375, 1996.
[12] S. H. Whang, D. P. Pope, and C. T. Liu, Eds., “High Temperature Aluminides and Intermetallics,” in *Proceedings of the Second International ASM Conference on High Temperature Aluminides and Intermetallics*, 1991.
[13] R. Mitra, *Intermetallic Matrix Composites*. Elsevier Science & Technology, 2017.
[14] Y. Gotoh *et al.*, “Synthesis of titanium carbide from a composite of TiO2 nanoparticles/methyl cellulose by carbothermal reduction,” *Mater. Res. Bull.*, vol. 36, no. 13–14, pp. 2263–2275, 2001.
[15] A. Rajabi, M. J. Ghazali, and A. R. Daud, “Chemical composition, microstructure and sintering temperature modifications on mechanical properties of TiC-based cermet - A review,” *Mater. Des.*, vol. 67, pp. 95–106, 2015.
[16] H. Abderrazak, F. Schoenstein, M. Abdellaoui, and N. Jouini, “Spark plasma sintering consolidation of nanostructured TiC prepared by mechanical alloying,” *Int. J. Refract. Met. Hard Mater.*, vol. 29, no. 2, pp. 170–176, 2011.
[17] M. Ashby, “Hybrid materials to expand the boundaries of material-property space,” *J. Am. Ceram. Soc.*, vol. 94, no. SUPPL. 1, 2011.
[18] R. W. Cahn, “Binary Alloy Phase Diagrams-Second edition. T. B. Massalski, Editor-in-Chief; H. Okamoto, P. R. Subramanian, L. Kacprzak, Editors. ASM

International, Materials Park, Ohio, USA. December 1990. xxii, 3589 pp., 3 vol., hard- back. $995.00 the set," *Adv. Mater.*, vol. 3, no. 12, pp. 628–629, Dec. 1991.
[19] M. P. Brady *et al.*, "The development of alumina-forming austenitic stainless steels for high-temperature structural use," *Jom*, vol. 60, no. 7, pp. 12–18, 2008.
[20] H. K. D. H. Bhadeshia, "Nickel Based Superalloys," *University of Cambridge*. [Online]. Available: http://www.phase-trans.msm.cam.ac.uk/2003/Superalloys/superalloys.html. [Accessed: 02-Oct-2018].
[21] G. K. Dey, "Physical metallurgy of nickel aluminides," *Sadhana*, vol. 28, no. 1–2, pp. 247–262, 2003.
[22] K. Yamashita, I. Fujimoto, T. Murakumo, S. Kumai, and A. Sato, "Observation of glide dislocations in D020 ordered Al3Ni," *Philos. Mag. A*, vol. 80, no. 1, pp. 219–235, 2000.
[23] T. P. Weihs, V. Zinoviev, D. V. Viens, and E. M. Schulson, "The strength, hardness and ductility of Ni3Al with and without boron," *Acta Metall.*, vol. 35, no. 5, pp. 1109–1118, May 1987.
[24] L. F. Mondolfo, *Aluminum Alloys: Structure and Properties*. 2013.
[25] G. Peng, Z. Tietao, X. Xiaoqing, G. Zhi, and C. Li, "Refinement Mechanism Research of Al3Ni Phase in Ni-7050 Alloy," *Rare Met. Mater. Eng.*, vol. 42, no. 1, pp. 6–13, 2013.
[26] T. N. Tiegs, K. B. Alexander, K. P. Plucknett, P. A. Menchhofer, P. F. Becher, and S. B. Waters, "Ceramic composites with a ductile Ni3Al binder phase," *Mater. Sci. Eng. A*, vol. 209, no. 1–2, pp. 243–247, 1996.
[27] B. Huang, W. Xiong, Q. Yang, Z. Yao, G. Zhang, and M. Zhang, "Preparation, microstructure and mechanical properties of multicomponent Ni3Al-bonded cermets," *Ceram. Int.*, vol. 40, no. 9 PART A, pp. 14073–14081, 2014.
[28] B. Huang, X. Tang, Y. Chen, H. Cheng, J. Yang, and W. Xiong, "High temperature oxidation behaviors of Ni3Al-bonded cermets," *J. Alloys Compd.*, vol. 704, pp. 443–452, 2017.
[29] Q. Shen, L. Zhang, and R. Tu, "Effect of Mo addition on the wettability between Ni3Al and TiC," *Key Eng. Mater.*, vol. 226, pp. 501–504, 2002.
[30] W. A. Sparling and K. P. Plucknett, "The effects of Mo2C additions on the sintering response of TiC0.3N0.7–Ni3Al cermets," *Int. J. Refract. Met. Hard Mater.*, vol. 61, pp. 98–106, 2016.
[31] K. P. Plucknett, P. F. Becher, and S. B. Waters, "Flexure Strength of Melt-Infiltrated-Processed Titanium Carbide/Nickel Aluminide Composites," *Ceram. Soc.*, vol. 44, pp. 1839–1844, 1998.
[32] P. F. Becher and K. P. Plucknett, "Properties of Ni3Al-bonded Titanium Carbide Ceramics," *J. Eur. Ceram. Soc.*, vol. 18, no. 4, pp. 395–400, 1998.
[33] Y. Pan and K. Sun, "Yi Pan 2000 upward melt infiltration.pdf," *J. Mater. Sci. Technol.*, vol. 16, no. 4, pp. 387–392, 2000.
[34] K. P. Plucknett and P. F. Becher, "Processing and Microstructure Development

of Titanium Carbide – Nickel Aluminide Composites Prepared by Melt Infiltration / Sintering (MIS),” vol. 61, pp. 55–61, 2001.
[35] R. B. Collier and K. P. Plucknett, “Aqueous Processing of TiC Preforms for Advanced Cermet Preparation,” in *Innovative Processing and Manufacturing of Advanced Ceramics and Composites*, Hoboken, NJ, USA: John Wiley & Sons, Inc., 2010, pp. 179–188.
[36] B. L. He and Y. F. Zhu, “Microstructure and properties of TiC/Ni3Al composites prepared by pressureless melt infiltration with porous TiC/Ni3Al preforms,” *Mater. Manuf. Process.*, vol. 26, no. 4, pp. 586–591, 2011.
[37] M. B. Holmes, A. Ibrahim, G. J. Kipouros, Z. N. Farhat, and K. P. Plucknett, “The effects of Ni3Al binder content on the electrochemical response of melt-infiltration processed TiC–Ni3Al cermets,” *Can. Metall. Q.*, vol. 55, no. 2, pp. 138–146, 2016.
[38] H. Liu, A. Wang, L. Wang, B. Ding, and Z. Hu, “In Situ Synthesis of TiC p / Ni 3 Al Composites under High Pressure,” vol. 23, no. 191815, pp. 521–523, 1997.
[39] T. L. Stewart and K. P. Plucknett, “The sliding wear of TiC and Ti(C,N) cermets prepared with a stoichiometric Ni3Al binder,” *Wear*, vol. 318, no. 1–2, pp. 153–167, 2014.
[40] X. Chen, J. Xu, Q. Sun, W. Yang, and W. Xiong, “Characterization of intermetallic bonded TiC composites prepared by mechanically induced self-sustained reaction,” *Mater. Des.*, vol. 89, pp. 102–108, 2016.
[41] Z. Memarrashidi and K. P. Plucknett, “The influence of Ni3Al binder content on the aqueous corrosion response of TiC and Ti(C,N) cermets,” *Int. J. Refract. Met. Hard Mater.*, vol. 64, pp. 113–121, 2017.
[42] L. M. Zhang, J. Liu, R. Z. Yuan, and T. Hirai, “Properties of TiC-Ni3Al composites and structural optimization of TiC-Ni3Al functionally gradient materials,” *Mater. Sci. Eng. A*, vol. 203, pp. 272–277, 1995.
[43] S. Skirl, R. Krause, S. M. Wiederhorn, and J. Rödel, “Processing and Mechanical Properties of Al2O3/Ni3Al Composites with Interpenetrating Network Microstructure,” *J. Am. Ceram. Soc.*, vol. 40, no. 9, pp. 2034–2040, 2001.
[44] R. B. Collier and K. P. Plucknett, “Spherical indentation damage in TiC-Ni3Al composites,” *Int. J. Refract. Met. Hard Mater.*, vol. 30, no. 1, pp. 188–195, 2012.
[45] J. Zhang and Y.-G. Jung, “Additive Manufacturing: Materials, Processes, Quantifications, and Applications,” p. 362, 2018.
[46] P. Nandwana, A. M. Elliott, D. Siddel, A. Merriman, W. H. Peter, and S. S. Babu, “Powder bed binder jet 3D printing of Inconel 718: Densification, microstructural evolution and challenges☆,” *Curr. Opin. Solid State Mater. Sci.*, vol. 21, no. 4, pp. 207–218, 2017.
[47] Y. Bai, G. Wagner, and C. B. Williams, “Effect of Bimodal Powder Mixture on Powder Packing Density and Sintered Density in Binder Jetting of Metals,” *2015 Annu. Int. Solid Free. Fabr. Symp.*, p. 62, 2015.
[48] W. Reitz, “Ceramic Processing and Sintering by M. N. Rahaman,” *Mater. Manuf.*

Process., vol. 12, no. 3, pp. 555–556, May 1997.
[49] Ashby, “a First Report on sintering diagrams,” *Acta Metall.*, vol. 22, no. March, 1974.
[50] N. Frumin, N. Frage, M. Polak, and M. P. Dariel, “Wettability and phase formation in the TiC<inf>x</inf>/Al system,” *Scr. Mater.*, vol. 37, no. 8, pp. 1263–1267, 1997.
[51] R. C. Pack, “Protective Coating of Titanium Diboride Reinforcement Particulates for Improvement of Titanium Metal Matrix Composite Armor Systems,” 2014.
[52] R. M. German, P. Suri, and S. J. Park, “Review: liquid phase sintering,” *J. Mater. Sci.*, vol. 44, no. 1, pp. 1–39, Jan. 2009.
[53] M. K. Aghajanian, M. A. Rocazella, J. T. Burke, and S. D. Keck, “The fabrication of metal matrix composites by a pressureless infiltration technique,” *J. Mater. Sci.*, vol. 26, no. 2, pp. 447–454, 1991.
[54] M. Rosso, “Ceramic and metal matrix composites: Routes and properties,” *J. Mater. Process. Technol.*, vol. 175, no. 1–3, pp. 364–375, Jun. 2006.
[55] N. Eustathopoulos, “Wetting by Liquid Metals—Application in Materials Processing: The Contribution of the Grenoble Group,” *Metals (Basel).*, vol. 5, no. 1, pp. 350–370, 2015.
[56] P. E. De Jongh and T. M. Eggenhuisen, “Melt infiltration: An emerging technique for the preparation of novel functional nanostructured materials,” *Adv. Mater.*, vol. 25, no. 46, pp. 6672–6690, 2013.
[57] D. Muscat and R. A. L. Drew, “Modeling the infiltration kinetics of molten aluminum into porous titanium carbide,” *Metall. Mater. Trans. A*, vol. 25, no. 11, pp. 2357–2370, 1994.
[58] D. Muscat, R. L. Harris, and R. A. L. Drew, “The effect of pore size on the infiltration kinetics of aluminum in titanium carbide preforms,” *Acta Metall. Mater.*, vol. 42, no. 12, pp. 4155–4163, 1994.
[59] N. Fries and M. Dreyer, “An analytic solution of capillary rise restrained by gravity,” *J. Colloid Interface Sci.*, vol. 320, no. 1, pp. 259–263, Apr. 2008.
[60] G. P. Martins, D. L. Olson, and G. R. Edwards, “Modeling of infiltration kinetics for liquid metal processing of composites,” *Metall. Trans. B*, vol. 19, no. 1, pp. 95–101, 1988.
[61] R. Anish, G. Robert Singh, and M. Sivapragash, “Techniques for processing metal matrix composite; A survey,” *Procedia Eng.*, vol. 38, pp. 3846–3854, 2012.
[62] D. Kopeliovich, “Liquid state fabrication of Metal Matrix Composites.” [Online]. Available: http://www.substech.com/dokuwiki/doku.php?id=liquid_state_fabrication_of_metal_matrix_composites.
[63] J. T. Blucher, “Discussion of a liquid metal pressure infiltration process to produce metal matrix composites,” *J. Mater. Process. Tech.*, vol. 30, no. 3, pp. 381–390, 1992.
[64] M. Dhanashekar and V. S. S. Kumar, “Squeeze Casting of Aluminium Metal Matrix Composites-An Overview,” *Procedia Eng.*, vol. 97, pp. 412–420, 2014.

[65] “Capillary Pressure,” *Missouri S&T University*. [Online]. Available: http://web.mst.edu/~numbere/cp/chapter 3.htm.
[66] F. Delannay, L. Froyen, and A. Deruyttere, “The wetting of solids by molten metals and its relation to the preparation of metal-matrix composites composites,” *J. Mater. Sci.*, vol. 22, no. 1, pp. 1–16, Jan. 1987.
[67] M. E. Schrader, “Young-Dupre Revisited,” *Langmuir*, vol. 11, no. 9, pp. 3585–3589, Sep. 1995.
[68] “Work of adhesion and Young-Laplace equation--Theory of surface tension, contact angle, wetting and work of adhesion (4).” [Online]. Available: http://www.surface-tension.org/article/62.html.
[69] G. V. Samsonov, A. D. Panasyuk, and G. K. Kozina, “Wetting of Refractory Carbides,” vol. 11, no. 11, pp. 874–878, 1968.
[70] W. S. Williams, “Physics of transition metal carbides,” *Mater. Sci. Eng. A*, vol. 105–106, pp. 1–10, Nov. 1988.
[71] S. Ahmad, “Metal Carbides,” *NED University of Engineering & Technology, Peoples Steel Mills Ltd.*, 2015. [Online]. Available: https://www.slideshare.net/ShamailAhmad/metal-carbides.
[72] T. Y. Kosolapova, *Carbides: Propeties, Production, and Applications*. Boston, MA: Springer US, 1995.
[73] W. Sen *et al.*, “Preparation of TiC powders by carbothermal reduction method in vacuum,” *Trans. Nonferrous Met. Soc. China (English Ed.*, vol. 21, no. 1, pp. 185–190, 2011.
[74] “Jade (2012).” Materials Data Inc., Livermore, CA 94550, USA.
[75] “ICDD, PDF-4+.” International Centre for Diffraction Data, Newtown Square, PA, 2016.
[76] F. B. Swinkels and M. F. Ashby, “A second report on sintering diagrams,” *Acta Metall.*, vol. 29, no. 2, pp. 259–281, 1981.
[77] M. X. Gao, Y. Pan, F. J. Oliveira, J. L. Baptista, and J. M. Vieira, “Microstructural characteristics of NiAl/TiC composites with high TiC content prepared by pressureless melt infiltration,” *J. Mater. Sci.*, vol. 39, pp. 6385–6387, 2004.
[78] A. E. Karantzalis, A. Lekatou, and K. Tsirka, “Solidification observations and sliding wear behavior of vacuum arc melting processed Ni-Al-TiC composites,” *Mater. Charact.*, vol. 69, pp. 97–107, 2012.
[79] I. Egry, J. Brillo, D. Holland-Moritz, and Y. Plevachuk, “The surface tension of liquid aluminium-based alloys,” *Mater. Sci. Eng. A*, vol. 495, no. 1–2, pp. 14–18, 2008.
[80] G. J. Shiflet and J. H. Merwe, “The role of structural ledges as misfit-compensating defects: fcc-bcc interphase boundaries,” *Metall. Mater. Trans. A*, vol. 25, no. 9, pp. 1895–1903, 1994.
[81] A. E. Karantzalis, A. Lekatou, E. Georgatis, Z. Arni, and V. Dracopoulos, “Solidification observations of vacuum arc melting processed Fe-Al-TiC composites: TiC precipitation mechanisms,” *Mater. Charact.*, vol. 62, no. 12, pp.

1196–1204, 2011.
[82] A. E. Karantzalis, Z. Arni, K. Tsirka, A. Evangelou, A. Lekatou, and V. Dracopoulos, “Fabrication of TiC-Reinforced Composites by Vacuum Arc Melting: TiC Mode of Reprecipitation in Different Molten Metals and Alloys,” *J. Mater. Eng. Perform.*, vol. 25, no. 8, pp. 3161–3172, 2016.
[83] R. Mitra, W. A. Chiou, M. E. Fine, and J. R. Weertman, “Interfaces in as-extruded XD Al / TiC and Al / TiB2 metal matrix composites,” *Most*, no. May, 1993.
[84] G. Dehm, J. Thomas, J. Mayer, T. Weißgärber, W. Püsche, and C. Sauer, “Formation and interface structure of TiC particles in dispersion-strengthened Cu alloys,” *Philos. Mag. A Phys. Condens. Matter, Struct. Defects Mech. Prop.*, vol. 77, no. 6, pp. 1531–1554, 1998.

Appendices

Appendix A: Infiltration of TiC Preform Prepared with Bi-modal Powder Distribution by $NiAl_3$

It is clear from previous infiltration experiments that only partial amounts of $NiAl_3$ are wicking into the TiC preform, evidenced by remnant material in the crucible. Yet despite this, calculations for the amount of powder required to fill the void space of the preform have assumed full infiltration of $NiAl_3$, similar to Ni_3Al. If only a partial amount of $NiAl_3$ is wicking into the preform, then it is possible that the porosity is a result of available liquid for complete infiltration. To address this, an infiltration experiment was conducted using a significant amount of excess $NiAl_3$ powder, approximately ~350 wt.% excess powder. Infiltration was conducted at 1415°C for 30 minutes. The results are shown in Fig. A-1 & A-2. The preform used for this particular experiment was printed using TiC with a bimodal powder distribution; sample B1. The density of the infiltrated composite was measured via the displacement method to be ~88% theoretical density, similar to previously infiltrated preforms by $NiAl_3$, which were ~88-90% theoretical density. Additionally, there were considerable amounts of solidified Al-rich liquid left in the crucible. Thus it can be determined that lack of available liquid is not the cause of porosity within the cermet. It was shown previously that the small amount of porosity in the Ni_3Al infiltrated preforms resulted from liquid infiltrant not penetrating clusters of TiC near the center of the preform, which would presumably be solved by a longer infiltration time due to their location. Within the $NiAl_3$ infiltrated preform there exists multiple phases of varying densities including the higher density Ni_2Al_3 (4.76g/cc) compared to $NiAl_3$ (3.96g/cc) and also possibly the formation of FCC Al (2.7g/cc). The complex solidification behavior involving these phases of varying densities possibly plays a role in the porosity formation within the infiltrated preform. The driving force of the infiltrant liquid to penetrate the TiC clusters could also be such that liquid does fully penetrate partial areas of tightly clustered TiC particles. Ultimately, the cause of the present porosity within the infiltrated preform is still unknown and requires further analysis.

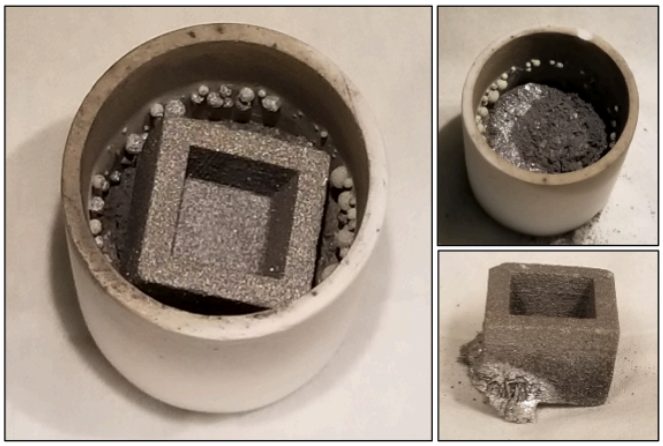


Figure A-1 Sample B1 infiltrated with $NiAl_3$ at 1415°C for 30 mins. Significant amount of excess material left in crucible. Silver, metallic chunk fused to bottom of infiltrated preform.

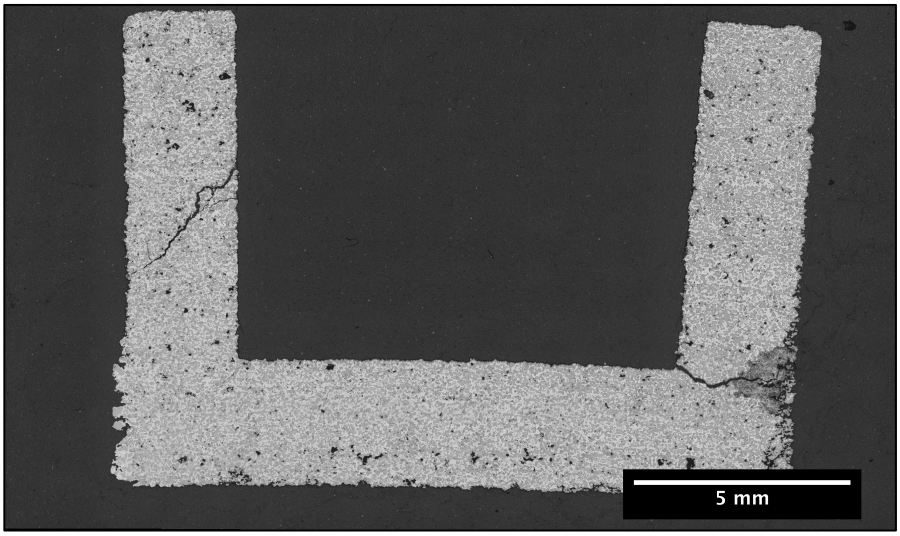


Figure A-2 Optical stitching cross-section of sample B1, infiltrated with $NiAl_3$ at 1415°C for 30 mins. Large cracking seen at base of right wall and mid-height of left wall occurred as a result of the hot mount process

Appendix B: EBSD Data for Sample 6

Crystallographic analysis of a $NiAl_3$ infiltrated preform was conducted in order to potentially characterize the presence of NiAl in the microstructure of the specimen, as predicted by thermodynamic simulation and possibly indicated by XRD.

Shown in Fig. B-1 is an image quality (IQ) map of the scanned area. An IQ map represents the individual IQ parameter obtained for each point during a scan, or, the quality of the electron backscatter diffraction pattern obtained at that point. The IQ map can be useful for visualizing the overall grain structure of the microstructure but caution must be taken in interpretation of such data. The dark grey area can be seen to be polycrystalline and was indexed as $NiAl_3$, shown in Fig. B-2. Indexing of the TiC particles proved difficult during this particular scan, with NiAl B2 showing in large amounts, but this is likely due to the high aerial density of particles plus the interaction volume of the x-rays with the underlying metal matrix.

The light grey regions, shown in Fig. B-1, are likely to be Ni_2Al_3 from previous compositional EDS analysis, however, indexing of this phase proved very difficult. Two of the grains of the light grey region indexed as Ni_2Al_3, while the rest of the light grey area showed great difficulty in indexing where NiAl and Ni_2Al_3 both are present. Ni_2Al_3 and NiAl were both analyzed due to the similarity in their crystal structure; NiAl is a BCC B2 structure while Ni_2Al_3 is simply a deformed NiAl trigonal structure. Generally, a better fit of the electron diffraction bands for the light grey region was found to be Ni_2Al_3, however, NiAl also showed a good fit and the calculated confidence index (CI) was zero. Confidence index is a calculated parameter that weighs the difference between the “first” best fit and “second” best fit to the electron diffraction bands in that if two phases are competing then the CI will be very low. An overlay of the CI parameter on the IQ map for each point is shown in Fig. B-3 and can be seen that the area where NiAl and Ni_2Al_3 are both present with poor indexing also shows a very low overall CI. Conversely, the light grey regions that index as Ni_2Al_3 have a higher CI. Raising the max peak count.

Overall, it was found that indexing the light grey, Ni-rich regions of the $NiAl_3$ infiltrated microstructure was very difficult where Ni_2Al_3 and NiAl both were found have a good fit. As mentioned previously, the crystal structures of Ni_2Al_3 and NiAl are very similar and may require more in-depth EBSD analysis in order to more accurately differentiate the two phases.

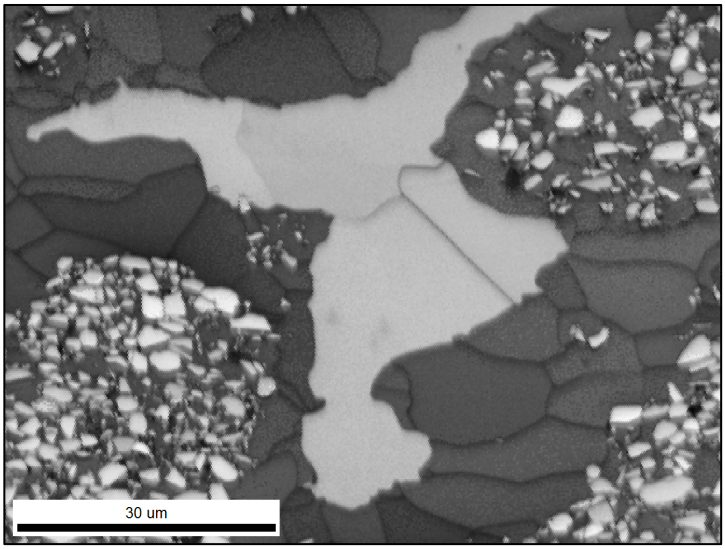


Figure B-1 Image Quality (IQ) Map of Sample 6, Infiltrated at 1415°C for 30 mins. Light grey region is Ni_2Al_3. Dark grey is $NiAl_3$.

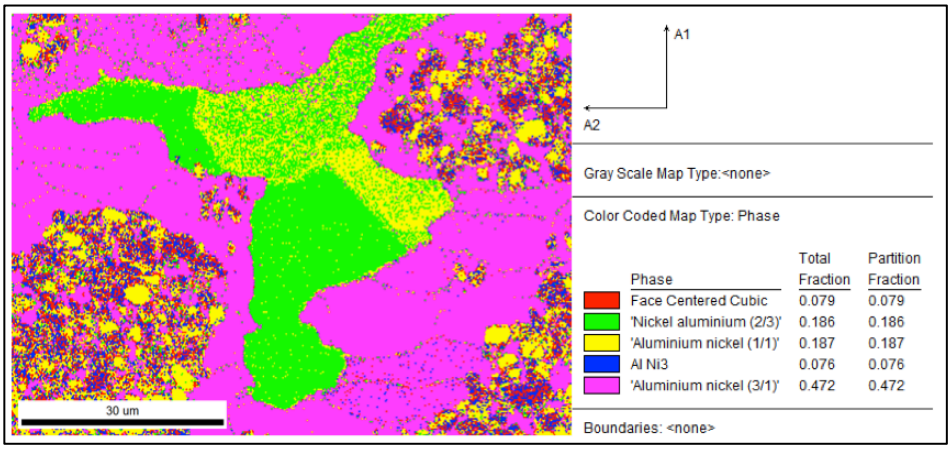


Figure B-2 Auto Phase Map of Sample 6.

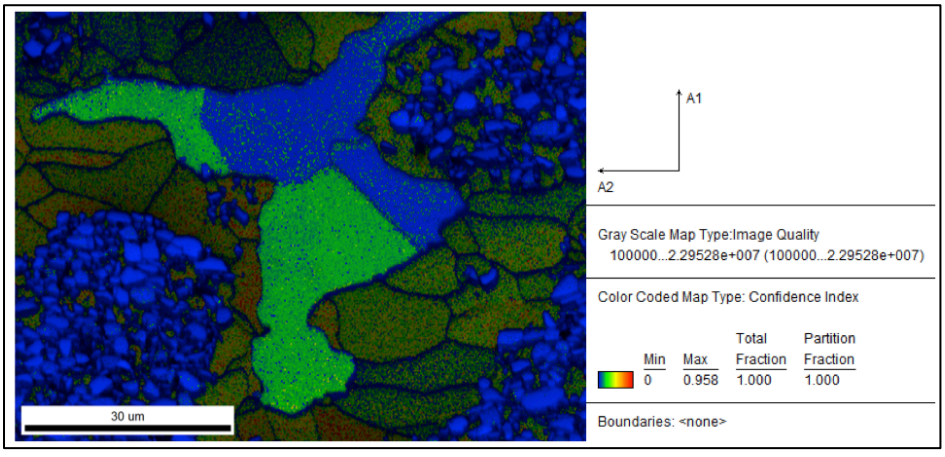


Figure B-3 IQ + CI map of Sample

Vita

Josh Arnold was born in Takoma Park, Maryland to the parents of Michael and Katherine Arnold and grew up in Seymour, Tennessee where he graduated from Heritage High School in 2011. Upon graduation, he began his studies at the University of Tennessee, Knoxville where he majored in Materials Science & Engineering. During his undergraduate career, Josh was selected twice to NASA's LARSS student research program at NASA Langley Research Center in Hampton, Virginia where he first fostered his interest in technical research. Josh received his Bachelor's of Science in Materials Science & Engineering in December of 2015 and then joined Oak Ridge National Laboratory's HERE research program until August 2015, where he then began his studies as a Master's student in the Materials Science & Engineering graduate program at the University of Tennessee, Knoxville under Dr. Suresh Babu. While a graduate student, Josh conducted his research at ORNL's Manufacturing Demonstration Facility. Josh was awarded his Master's of Science in Materials Science & Engineering in August 2018 and will continue his career as a Product Development Engineer at Arconic Engines in Savannah, Georgia.